# Spin-dependent phenomena and device concepts explored in (Ga,Mn)As

T. Jungwirth

*Institute of Physics, Academy of Sciences of the Czech Republic, Cukrovarnická 10, 162 53 Praha 6, Czech Republic*
*and School of Physics and Astronomy, University of Nottingham, Nottingham NG7 2RD, United Kingdom*

J. Wunderlich

*Institute of Physics, Academy of Sciences of the Czech Republic, Cukrovarnická 10, 162 53 Praha 6, Czech Republic*
*and Hitachi Cambridge Laboratory, Cambridge CB3 0HE, United Kingdom*

V. Novák and K. Olejník

*Institute of Physics, Academy of Sciences of the Czech Republic, Cukrovarnická 10, 162 53 Praha 6, Czech Republic*

B. L. Gallagher, R. P. Campion, K. W. Edmonds, and A. W. Rushforth

*School of Physics and Astronomy, University of Nottingham, Nottingham NG7 2RD, United Kingdom*

A. J. Ferguson

*Microelectronics Group, Cavendish Laboratory, University of Cambridge, CB3 0HE, United Kingdom*

P. Němec

*Faculty of Mathematics and Physics, Charles University in Prague, Ke Karlovu 3, 121 16 Prague 2, Czech Republic*
(published 11 July 2014)

Over the past two decades, the research of (Ga,Mn)As has led to a deeper understanding of relativistic spin-dependent phenomena in magnetic systems. It has also led to discoveries of new effects and demonstrations of unprecedented functionalities of experimental spintronic devices with general applicability to a wide range of materials. This is a review of the basic material properties that make (Ga,Mn)As a favorable test-bed system for spintronics research and a discussion of contributions of (Ga,Mn)As studies in the general context of the spin-dependent phenomena and device concepts. Special focus is on the spin-orbit coupling induced effects and the reviewed topics include the interaction of spin with electrical current, light, and heat.

## CONTENTS

## I. INTRODUCTION

Under equilibrium growth conditions the incorporation of magnetic Mn ions into III-As semiconductor crystals is limited to approximately 0.1%. To circumvent the solubility problem a nonequilibrium, low-temperature molecular-beam-epitaxy (LT-MBE) technique was employed which led to the first successful growths of (In,Mn)As and (Ga,Mn)As ternary alloys with more than 1% Mn and to the discovery of ferromagnetism in these materials (Ohno *et al.*, 1992, 1996; Munekata *et al.*, 1993; Hayashi *et al.*, 1997, 2001; Shen *et al.*, 1997; Van Esch *et al.*, 1997; Ohno, 1998; Shimizu *et al.*, 1999).

The compounds qualify as ferromagnetic semiconductors to the extent that their magnetic properties can be altered by the usual semiconductor electronics engineering variables, such as doping, electric fields, or light. The achievement of ferromagnetism in an ordinary III-V semiconductor with Mn concentrations exceeding 1% demonstrates on its own the sensitivity of magnetic properties to doping. Several experiments have verified that changes in the carrier density and distribution in thin (III,Mn)As films due to an applied gate voltage can induce reversible changes of the Curie temperature $T_c$ and other magnetic and magnetotransport properties (Ohno *et al.*, 2000; Chiba *et al.*, 2003, 2008, 2013; Chiba, Matsukura, and Ohno, 2006; Wunderlich, Jungwirth, Irvine *et al.*, 2007; Olejník *et al.*, 2008; Stolichnov *et al.*, 2008; Owen *et al.*, 2009; Riester *et al.*, 2009; Sawicki *et al.*, 2010; Mikheev *et al.*, 2012; Niazi *et al.*, 2013). Experiments in which ferromagnetism in a (III,Mn)As system is turned on and off optically or in which recombination of spin-polarized carriers injected from the ferromagnetic semiconductor yields emission of circularly polarized light clearly demonstrated the interaction of spin and light in these materials (Koshihara *et al.*, 1997; Munekata *et al.*, 1997; Ohno *et al.*, 1999).

(Ga,Mn)As has become a test-bed material for the research of phenomena in which charge carriers respond to spin and vice versa. By exploiting the large spin polarization of carriers in (Ga,Mn)As and building on the well-established hetero-structure growth and microfabrication techniques in semi-conductors, high-quality magnetic tunnel junctions have been demonstrated showing large tunneling magnetoresistances (TMRs) (Tanaka and Higo, 2001; Chiba, Matsukura, and Ohno, 2004; Mattana *et al.*, 2005; Saito, Yuasa, and Ando, 2005). In the studies of the inverse magnetotransport effects, namely, spin-transfer torques (STTs) in tunnel junctions (Chiba *et al.*, 2004) and domain walls (DWs) (Yamanouchi *et al.*, 2004, 2006; Wunderlich *et al.*, 2007; Adam *et al.*, 2009; Wang *et al.*, 2010; Curiale *et al.*, 2012; De Ranieri *et al.*, 2013), the dilute-moment *p*-type (Ga,Mn)As is unique for its low saturation magnetization and strongly spin-orbit coupled valence band (Sinova, Jungwirth *et al.*, 2004; Garate, Gilmore *et al.*, 2009; Hals, Nguyen, and Brataas, 2009). Compared to common transition-metal ferromagnets this implies a more significant role of the fieldlike (nonadiabatic) STT complementing the anti-damping-like (adiabatic) STT

and lower currents required to excite magnetization dynamics. Moreover, the leading role of magnetocrystalline anisotropies over the dipolar shape anisotropy fields allows for the control of the direct and inverse magnetotransport phenomena by tuning the lattice strains *ex situ* by microfabrication (Wenisch *et al.*, 2007; Wunderlich *et al.*, 2007) or *in situ* by piezoelectric transducers (Goennenwein *et al.*, 2008; Overby *et al.*, 2008; Rushforth *et al.*, 2008; De Ranieri *et al.*, 2013).

In general, TMR (Julliere, 1975; Miyazaki and Tezuka, 1995; Moodera *et al.*, 1995) and STT (Berger, 1996; Slonczewski, 1996; Zhang and Li, 2004) are examples of spin-dependent phenomena which can be understood within the basically nonrelativistic two-channel model of conduction in ferromagnets (Mott, 1964), and in which spins are transported between at least two noncollinear parts of a nonuniform magnetic structure with the magnetization in one part serving as a reference to the other one. Besides these more commonly considered spintronic effects, (Ga,Mn)As studies have extensively focused on relativistic phenomena which in principle can be observed in uniform magnetic structures and where the spin dependence of the transport stems from the internal spin-orbit coupling in carrier bands. An archetypical example among these effects is the anisotropic magnetoresistance (AMR) discovered by Kelvin more than 150 years ago in wires of Ni and Fe (Thomson, 1857). Research in (Ga,Mn)As led to the observation of a tunneling anisotropic magneto-resistance (TAMR) (Brey, Tejedor, and Fernández-Rossier, 2004; Gould *et al.*, 2004). Unlike the TMR which corresponds to the different resistances of the parallel and antiparallel magnetizations in two magnetic electrodes separated by the tunnel barrier, the TAMR relies on the rotation of the magnetization in a single magnetic electrode while the other electrode can be nonmagnetic. Large and electrically tunable relativistic anisotropic magnetotransport phenomena were observed in the Coulomb blockade (CB) devices in which (Ga,Mn)As formed the island or the gate electrode of a single-electron transistor (SET) (Wunderlich *et al.*, 2006; Schlapps *et al.*, 2009; Ciccarelli *et al.*, 2012). The TAMR and CB-AMR were subsequently reported in other systems including common transition-metal ferromagnets and antiferromagnets (Gao *et al.*, 2007; Moser *et al.*, 2007; Park *et al.*, 2008, 2011; Bernand-Mantel *et al.*, 2009).

For the inverse magnetotransport effects, the relativistic counterpart of the STT is the current-induced spin-orbit torque (SOT) (Bernevig and Vafek, 2005; Manchon and Zhang, 2008). Similar to the TAMR and CB-AMR, the SOT can be observed in uniform magnets, the seminal experiment was performed in (Ga,Mn)As (Chernyshov *et al.*, 2009), and subsequently the phenomenon was reported in other systems including transition-metal ferromagnets (Miron *et al.*, 2010). For the SOT, the above-mentioned favorable characteristics of (Ga,Mn)As, namely, the strong spin-orbit coupling in the carrier bands and exchange coupling of carrier spins with the dilute local moments, combine with the broken space-inversion symmetry in the host zinc-blende lattice. The broken space-inversion symmetry is a necessary condition for observing the relativistic SOT (Bernevig and Vafek, 2005; Manchon and Zhang, 2008).

Theoretical studies of the intrinsic nature of the anomalous Hall effect (AHE) (Luttinger, 1958; Jungwirth, Niu, and

MacDonald, 2002; Onoda and Nagaosa, 2002) and experiments in (Ga,Mn)As interpreted by this theory (Jungwirth, Niu, and MacDonald, 2002; Nagaosa *et al.*, 2010) have inspired a renewed interest in the AHE in a broad class of ferromagnets (Nagaosa *et al.*, 2010). Simultaneously they led to predictions of a directly related intrinsic spin Hall effect (SHE) (Murakami, Nagaosa, and Zhang, 2003; Sinova, Culcer *et al.*, 2004) in which the spin-dependent transverse deflection of electrons originating from the relativistic band structure occurs in a nonmagnetic conductor. The intrinsic SHE proposal triggered an intense theoretical debate and prompted the experimental discovery of the phenomenon (Kato *et al.*, 2004; Wunderlich *et al.*, 2005). The SHE has become a common tool to electrically detect or generate spin currents (Jungwirth, Wunderlich, and Olejník, 2012) and the intrinsic SHE combined with the STT can allow for an in-plane current-induced switching of the free magnetic electrode in a TMR magnetic tunnel junction (Liu *et al.*, 2012). An intense discussion ensued on the alternative, SHE-STT based or SOT based interpretations of these in-plane current-induced spin reorientation effects (Miron *et al.*, 2011; Liu *et al.*, 2012; Garello *et al.*, 2013). Research in (Ga,Mn)As continues to contribute to this area in a distinct way; experimental and theoretical studies in (Ga,Mn)As have uncovered the fact that the intrinsic SHE and SOT can be linked by a common microscopic origin (Kurebayashi *et al.*, 2014), the same one that was originally proposed for interpreting the AHE data in (Ga,Mn)As (Jungwirth, Niu, and MacDonald, 2002).

The SHE, STT, and SOT phenomena are at the forefront of the research field of electrically controlled spin manipulation and play an important role in the development of a new generation of magnetic random access memories (MRAMs), tunable oscillators, and other spintronic devices (Chappert, Fert, and Dau, 2007; Ralph and Stiles, 2008). Optical excitations of magnetic systems by laser pulses have traditionally represented a complementary research field whose aim is to explore magnetization dynamics at short time scales and enable ultrafast spintronic devices (Kirilyuk, Kimel, and Rasing, 2010). The optical counterparts of the STT and SOT, in which current carriers are replaced by photocarriers and which have been identified in laser induced spin-dynamics studies in (Ga,Mn)As (Fernández-Rossier *et al.*, 2003; Núñez *et al.*, 2004; Nemec *et al.*, 2012; Tesarova *et al.*, 2013), build a bridge between these two important fields of spintronics research. The direct-gap GaAs host allowing for the generation of a high density of photocarriers, optical selection rules linking light and carrier-spin polarizations, and the carrier spins interacting with magnetic moments on Mn via exchange coupling make (Ga,Mn)As a unique ferromagnetic system for exploring the interplay of photonics and spintronics.

Thermopower, also known as the Seebeck effect, is the ability of conductors to generate electric voltages from thermal gradients. A subfield of spintronics, termed spin caloritronics, explores the possibility of controlling charge and spin by heat and vice versa (Bauer, Saitoh, and van Wees, 2012). In (Ga,Mn)As, experiments on the anomalous Nernst effect (ANE) (Pu *et al.*, 2008), which is the spin-caloritronics counterpart to the AHE, confirmed the validity of the Mott relation between the off-diagonal electrical and thermal transport coefficients in a ferromagnet (Wang *et al.*, 2001). The

experiments also firmly established the intrinsic nature of both the AHE and ANE in metallic (Ga,Mn)As. The anisotropic magnetothermopower (AMT) (Ky, 1966) is a phenomenon in which the Seebeck coefficient of a uniform magnetic conductor depends on the angle between the applied temperature gradient and magnetization. Measurements of this counterpart to the AMR electrical-transport effect in (Ga,Mn)As (Pu *et al.*, 2006) initiated renewed interest in the phenomenon in a broad class of magnetic materials (Wisniewski, 2007; Tang *et al.*, 2011; Anwar, Lacoste, and Aarts, 2012; Mitdank *et al.*, 2012). The spin-caloritronic counterpart of the TMR effect in magnetic tunnel junctions is observed when the voltage gradient across the junction is replaced with a temperature gradient. The resulting tunneling magnetothermopower (TMT) represents the difference between the Seebeck coefficients for the parallel and antiparallel magnetizations of the tunnel junction electrodes (Liebing *et al.*, 2011; Walter *et al.*, 2011). The relativistic analog in a tunnel junction with only one magnetic electrode is the tunneling anisotropic magnetothermopower (TAMT) whose observation was reported in (Ga,Mn)As (Naydenova *et al.*, 2011), reminiscent of the discovery of the TAMR (Gould *et al.*, 2004). Another spin-caloritronics effect which is distinct from the magnetothermopower (magneto-Seebeck) phenomena is the spin-Seebeck effect (Uchida *et al.*, 2008, 2010; Jaworski *et al.*, 2010; Sinova, 2010). Here the thermal gradient in a ferromagnet induces a spin current which is then converted into electrical voltage via, e.g., the SHE in an attached nonmagnetic electrode (Uchida *et al.*, 2008, 2010; Jaworski *et al.*, 2010; Sinova, 2010). Experiments in (Ga,Mn)As (Jaworski *et al.*, 2010) provided a direct evidence that, unlike the Seebeck effect in normal conductors, the spin-Seebeck effect does not originate from charge flow. The intriguing origin of the spin-Seebeck effect has been extensively debated (Bauer, Saitoh, and van Wees, 2012; Tikhonov, Sinova, and Finkeľstein, 2013) since these seminal experiments.

In Sec. II we provide an overview of the material properties of (Ga,Mn)As with the emphasis on characteristics that make (Ga,Mn)As a favorable model system for spintronics research. For more detailed discussions of the materials aspects of the research of (Ga,Mn)As in the context of the family of (III,Mn) V and other magnetic materials we refer to other comprehensive review articles (Matsukura, Ohno, and Dietl, 2002; Dietl, 2003; Jungwirth, Sinova *et al.*, 2006; Sato *et al.*, 2010; Dietl and Ohno, 2014). The focus of this review is the spin-dependent phenomena and devices concepts explored in (Ga,Mn)As, and their relevance within the broad spintronics research field. These are discussed in Sec. III. Our aim is to find conceptual links between the seemingly diverse areas of spintronic studies in (Ga,Mn)As. Simultaneously, we attempt to provide intuitive physical pictures of the spin-dependent phenomena and functionalities for not only describing the specific observations in the ferromagnetic semiconductor (Ga,Mn)As but also for highlighting their applicability to other materials including the common transition-metal ferromagnets, and other types of magnetic order such as antiferromagnets. While (Ga,Mn)As and the related ferromagnetic semiconductors have so far failed to allow for practical spintronic functionalities at room temperature, transition-metal ferromagnets are commonly used in commercial

spintronic devices (Chappert, Fert, and Dau, 2007) and antiferromagnets can readily combine room-temperature operation with not only metal but also semiconductor electronic structure (Jungwirth *et al.*, 2011). In Sec. IV we provide a brief summary of the spintronics research directions inspired by (Ga,Mn)As.

## II. TEST-BED MATERIAL FOR SPINTRONICS RESEARCH

### A. Electronic structure and magnetism in (Ga,Mn)As

The elements in the (Ga,Mn)As compound have nominal atomic structures $[Ar]3d^{10}4s^2p^1$ for Ga, $[Ar]3d^5 4s^2$ for Mn, and $[Ar]3d^{10}4s^2p^3$ for As. This circumstance correctly suggests that the most stable position of Mn in the GaAs host lattice, at least up to a certain level of Mn doping, is on the Ga site where its two 4s electrons can participate in crystal bonding in much the same way as the two Ga 4s electrons. Because of the missing valence 4p electron, the substitutional $Mn_{Ga}$ impurity acts as an acceptor. In the electrically neutral state, the isolated $Mn_{Ga}$ has the character of a local moment with zero angular momentum and spin $S = 5/2$ (Landé g factor $g = 2$) due to the five 3d electrons and a moderately bound hole. GaAs is an intermediate band-gap III-V semiconductor, with $E_g = 1.5$ eV at low temperatures. The experimental acceptor binding energy of an isolated Mn impurity substituting for Ga is of an intermediate strength $E_a^0 \approx 0.1$ eV (Chapman and Hutchinson, 1967; Blakemore *et al.*, 1973; Bhattacharjee and à la Guillaume, 2000; Madelung, Rössler, and Schulz, 2003; Yakunin *et al.*, 2004).

The perturbation of the crystal potential of GaAs due to a single Mn impurity has three main components as shown in Fig. 1 (Mašek *et al.*, 2010). (i) The first is the long-range hydrogeniclike potential of a single acceptor in GaAs which alone produces a bound state at about 30 meV above the valence band (Marder, 2000). (ii) The second contribution is a short-range central-cell potential. It is specific to a given impurity and reflects the difference in the electronegativity of the impurity and the host atom (Harrison, 1980). For a conventional nonmagnetic acceptor $Zn_{Ga}$, which is the first

nearest neighbor of Ga in the periodic table, the atomic p levels are shifted by ~0.25 eV which increases the binding energy by ~5 meV. For Mn, the sixth nearest neighbor of Ga, the p-level shift, is ~1.5 eV which when compared to $Zn_{Ga}$ implies the central-cell contribution to the acceptor level of $Mn_{Ga}$ ~30 meV (Bhattacharjee and à la Guillaume, 2000). (iii) The remaining part of the $Mn_{Ga}$ binding energy is due to the spin-dependent hybridization of Mn d states with neighboring As p states. Its contribution, which has been directly inferred from spectroscopic measurements of uncoupled $Mn_{Ga}$ impurities (Schneider *et al.*, 1987; Linnarsson *et al.*, 1997; Bhattacharjee and à la Guillaume, 2000), is again comparable to the binding energy of the hydrogenic single-acceptor potential. Combining (i)–(iii) accounts for the experimental binding energy of the $Mn_{Ga}$ acceptor of 0.1 eV. An important caveat to these elementary considerations is that the short-range potentials alone of strengths inferred in (ii) and (iii) would not produce a bound state above the top of the valence band but only a broad region of scattering states inside the valence band.

The low-energy degrees of freedom in (Ga,Mn)As materials are the orientations of Mn local moments and the occupation numbers of acceptor levels near the top of the valence band. The number of local moments and the number of holes may differ from the number of $Mn_{Ga}$ impurities in the GaAs host due to the presence of charge and moment compensating defects. Hybridization between Mn d orbitals and valence As/Ga sp orbitals, mainly the As p orbitals on the neighboring sites, leads to an antiferromagnetic exchange interaction between the spins that they carry (Schneider *et al.*, 1987; Linnarsson *et al.*, 1997; Okabayashi *et al.*, 1998; Bhattacharjee and à la Guillaume, 2000).

At concentrations ≪ 1% of substitutional Mn, the average distance between Mn impurities (or between holes bound to Mn ions) is much larger than the size of the bound hole characterized approximately by the impurity effective Bohr radius. These very dilute (Ga,Mn)As systems are insulating, with the holes occupying a narrow impurity band, and paramagnetic. Experimentally, ferromagnetism in (Ga,Mn)As is observed when Mn doping reaches approximately 1% and the system is still below but near the insulator-to-metal transition (Ohno, 1999; Potashnik *et al.*, 2002; Campion *et al.*, 2003; Jungwirth *et al.*, 2007). ($x = 1$% Mn doping corresponds to Mn density $c = 4x/a^3 = 2.2 \times 10^{20}$ cm$^{-3}$, where a is the lattice constant in $Ga_{1-x}Mn_xAs$.)

At these Mn concentrations, the localization length of the holes is extended to a degree that allows them to mediate, via the p-d hybridization, ferromagnetic exchange interaction between Mn local moments, even though the moments are dilute.

Beyond a critical Mn doping, which in experiments is about 1.5%, Mn-doped GaAs exhibits a transition to a state in which the Mn-impurity levels overlap sufficiently strongly that the ground state is metallic, i.e., that states at the Fermi level are not bound to a single or a group of Mn atoms but are delocalized across the system (Matsukura, Ohno, and Dietl, 2002; Jungwirth, Sinova *et al.*, 2006; Jungwirth *et al.*, 2007). In the metallic regime Mn can, like a shallow acceptor (e.g., C, Be, Mg, Zn), provide delocalized holes with a low-temperature density comparable to Mn density
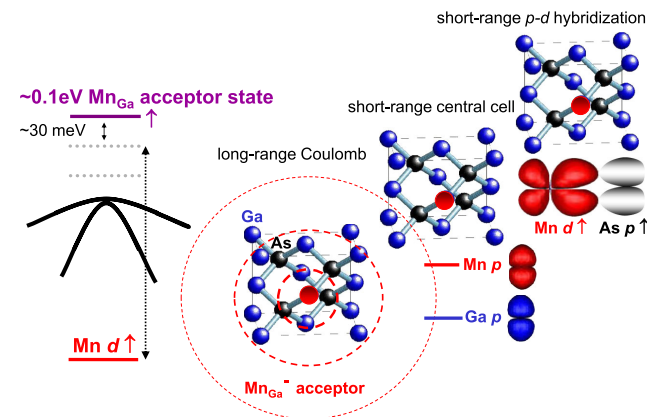


FIG. 1 (color online). Schematic illustration of the long-range Coulomb and the two short-range potentials each contributing ~30 meV to the binding energy of the $Mn_{Ga}$ acceptor. From Mašek *et al.*, 2010.

(Ruzmetov *et al.*, 2004; Jungwirth *et al.*, 2005; MacDonald, Schiffer, and Samarth, 2005). The transition to the metallic state occurs at Mn density which is about 2 orders of magnitude larger than in GaAs doped with shallow acceptors (Ferreira da Silva *et al.*, 2004). This is because of the central cell and *p-d* hybridization contributions to the binding energy which make Mn acceptors more localized than the shallow acceptors. A crude estimate of the critical metal-insulator transition density can be obtained with a short-range potential model, using the experimental binding energy and assuming an effective mass of valence band holes $m^* = 0.5 m_e$. This model implies an isolated acceptor level with effective Bohr radius $a_0 = (\hbar^2 / 2 m^* E_a^0)^{1/2} = 10$ Å. The radius $a_0$ then equals the Mn-impurity spacing scale $c^{-1/3}$ at $c \approx 10^{21}$ cm$^{-3}$. This explains qualitatively the higher metal-insulator-transition critical density in Mn-doped GaAs compared to the case of systems doped with shallow, more hydrogeniclike acceptors which have binding energies $E_a^0 \approx 30$ meV (Madelung, Rössler, and Schulz, 2003; Ferreira da Silva *et al.*, 2004).

Unlike the metal-insulator phase transition, which is sharply defined in terms of the temperature $T = 0$ limit of the conductivity, the crossover in the character of states near the Fermi level in semiconductors with increased doping is gradual (Shklovskii and Efros, 1984; Lee and Ramakrishnan, 1985; Paalanen and Bhatt, 1991; Jungwirth, Sinova *et al.*, 2006; Dietl, 2007, 2008). At very weak doping, the Fermi level resides inside a narrow impurity band (assuming some compensation) separated from the valence band by an energy gap of a magnitude close to the impurity binding energy. In this regime strong electronic correlations are an essential element of the physics and a single-particle picture has limited utility. Well into the metallic state, on the other hand, the impurities are sufficiently close together, and the long-range Coulomb potentials which contribute to the binding energy of an isolated impurity are sufficiently screened, in which the system can be viewed as an imperfect crystal with disorder-broadened and shifted host bands. In this regime, electronic correlations are usually less strong and a single-particle picture often suffices. The short-range components of the Mn binding energy in GaAs, which are not screened by the carriers, move the crossover to higher dopings and contribute significantly to carrier scattering in the metallic state. The picture of disorder-broadened and shifted Bloch bands has to be applied, therefore, with care even in the most metallic (Ga,Mn)As materials. While for some properties it may provide even a semiquantitatively reliable description, for other properties it may fail, as we discuss in more detail below.

Although neither picture is very helpful for describing the physics in the crossover regime which spans some finite range of dopings, the notion of the impurity band on the lower doping side from the crossover and of the disordered exchange-split host band on the higher doping side from the crossover still have a clear qualitative meaning. The former implies that there is a deep minimum in the density of states between separate impurity and host band states. In the latter case the impurity band and the host band merge into one inseparable band whose tail may still contain localized states depending on the carrier concentration and disorder. In metallic ferromagnetic (Ga,Mn)As materials, hard x-ray angle-resolved photoemission (Gray *et al.*, 2012) and the

differential off- and on-resonance photoemission (Di Marco *et al.*, 2013) data do not show a separation or intensity drop near the Fermi energy that would indicate the presence of a gap between the valence band and a Mn-impurity band. The host and impurity bands are merged in ferromagnetic (Ga,Mn)As according to these spectroscopic measurements. Note that terms overlapping and merging impurity and valence bands describe the same basic physics in (Ga,Mn)As. This is because the Mn-acceptor states span several unit cells even in the very dilute limit and many unit cells as the impurity band broadens with increasing doping. The localized and delocalized states then have a similarly mixed As-Ga-Mn *spd* character. This applies to systems on either side of the metal-insulator transition. By recognizing that the bands are merged, that is, overlapped and mixed, in ferromagnetic (Ga,Mn)As materials, the distinction between valence and impurity states becomes mere semantics which can lead to seemingly controversial statements on the material's electronic structure but has no fundamental physics relevance.

A microscopic theory directly linked to the above qualitative considerations is based on the *spd* tight-binding approximation (TBA) Hamiltonian of (Ga,Mn)As in which electronic correlations on the localized Mn *d* orbitals are treated using the Anderson model of the magnetic impurity (Mašek *et al.*, 2010). In Fig. 2 we plot examples of the total and orbital resolved densities of states (DOSs) for 10% of Mn$_{Ga}$ impurities. The Mn-*d* spectral weight is peaked at several eV below the top of the valence band, in agreement with photoemission data (Okabayashi *et al.*, 1998; Gray *et al.*, 2012; Di Marco *et al.*, 2013), and is significantly smaller near the Fermi energy $E_F$. The Fermi level states at the top of the valence band have a dominant As(Ga) *p*-orbital character. The *p-d* coupling strength $N_0 \beta \equiv N_0 J_{ex} = \Delta / Sx$ ($N_0 = 1/\Omega_{u.c.}$, where $\Omega_{u.c.}$ is the unit cell volume) (Jungwirth, Sinova *et al.*, 2006), determined from the calculated valence band exchange splitting $\Delta$ (and taking $S = 5/2$), is close to the upper bound of the reported experimental range of $N_0 \beta \sim 1$–3 eV (Matsukura *et al.*, 1998; Okabayashi *et al.*, 1998; Szczytko *et al.*, 1999; Bhattacharjee and à la Guillaume, 2000; Omiya



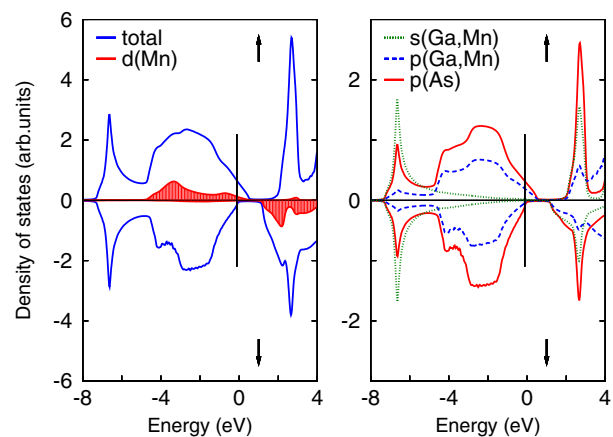FIG. 2 (color online). TBA-Anderson density of states of Ga$_{0.9}$Mn$_{0.1}$As and its orbital composition. The position of the Fermi energy is indicated by a vertical line. From Mašek *et al.*, 2010.

*et al.*, 2000). This is regarded as a moderately weak *p-d* coupling because the corresponding Fermi level states of the (Ga,Mn)As have a similar orbital character to the states in the host GaAs valence band. These spectral features are among the key characteristics of the hole mediated ferromagnetism in (Ga,Mn)As.

The effective Hamiltonian theory of (Ga,Mn)As, based on the kinetic-exchange (Zener) model (Dietl, Haury, and d'Aubigne, 1997; Jungwirth *et al.*, 1999; Dietl *et al.*, 2000; Jungwirth, Sinova *et al.*, 2006), assumes also a value of $N_0\beta$ within the above experimental range, namely, $N_0\beta = 1.2$ eV ($J_{\mathrm{ex}} = 55$ meV nm$^3$) which is closer to the lower experimental bound (Jungwirth, Sinova *et al.*, 2006). It is this moderate *p-d* hybridization that allows it to be treated perturbatively and to perform the Schrieffer-Wolff transformation from the microscopic TBA-Anderson Hamiltonian to the effective model in which valence band states experience a spin-dependent kinetic-exchange field (Jungwirth, Sinova *et al.*, 2006). Hence, the effective kinetic-exchange model and the microscopic TBA-Anderson theory provide a consistent physical picture of ferromagnetic (Ga,Mn)As. These two models of the electronic structure of (Ga,Mn)As have represented the most extensively used basis for analyzing the spin-dependent phenomena and device functionalities in (Ga,Mn)As.

In Fig. 3 we show DOSs over the entire $Mn_{Ga}$ doping range obtained from the generalized gradient approximation (GGA + *U*) density-functional calculations (Mašek *et al.*, 2010; Sato *et al.*, 2010). The GGA + *U*, the TBA-Anderson, and the kinetic-exchange Zener theories all provide a consistent picture of the band structure of ferromagnetic (Ga,Mn)As. Simultaneously, it is important to keep in mind that the moderate acceptor binding energy of $Mn_{Ga}$ shifts the insulator-to-metal transition to orders of magnitude higher doping densities than in the case of common shallow non-magnetic acceptors, as mentioned above (Jungwirth *et al.*, 2007; Mašek *et al.*, 2010). Disorder and correlation effects, therefore, play a comparatively more significant role in (Ga,Mn)As than in degenerate semiconductors with common shallow dopants and any simplified one-particle band picture
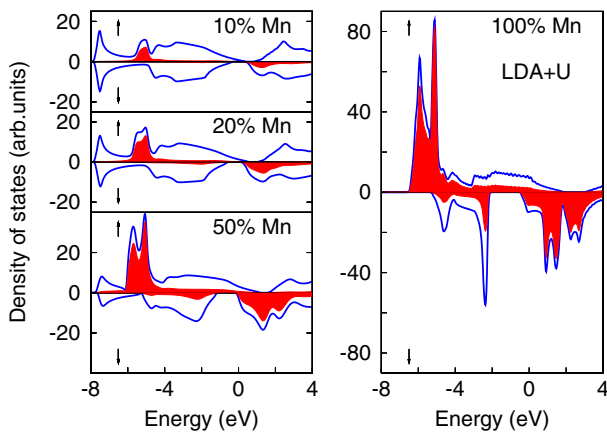
of ferromagnetic (Ga,Mn)As can represent a proxy only to the electronic structure of the material.

As seen in Fig. 3, the bands evolve continuously from the intrinsic nonmagnetic semiconductor GaAs via the degenerate ferromagnetic semiconductor (Ga,Mn)As to the ferromagnetic metal MnAs. From this it can be expected that $T_c$ of MnAs, with the value close to room temperature [350 K for cubic MnAs inclusions in (Ga,Mn)As (Yokoyama *et al.*, 2005; Kovacs *et al.*, 2011)], sets the upper theoretical bound of achievable $T_c$'s in (Ga,Mn)As across the entire doping range. In experiment, as discussed in Sec. II.B, the $Mn_{Ga}$ doping is limited to approximately 10% with corresponding $T_c$ reaching 190 K in uniform thin-film crystals prepared by optimized LT-MBE synthesis and postgrowth annealing. In these samples the hole density is in the $\sim10^{20}$–$10^{21}$ cm$^{-3}$ range, i.e., several orders of magnitude higher than densities in commonly used nonmagnetic semiconductors but also 1–2 orders of magnitude lower than is typical for metals.

### 1. Curie point singularities

Ferromagnetic (Ga,Mn)As with Mn doping ranging from $\sim1\%$ to $\sim10\%$ is a very heavily doped compound semiconductor or can be also regarded at these high Mn concentrations as a random alloy. Quantities such as the residual resistivity are then inevitably affected by strong disorder effects. Even in the most metallic (Ga,Mn)As materials the hole mean free path is comparable to the separation of the Mn impurities so the diffusivity is low. Typically, the product of the Fermi wave vector and the mean free path is $k_F\Lambda = \hbar\mu k_F^2/e \sim 1$–10, estimated from the experimental mobilities $\mu$ and hole densities (Jungwirth *et al.*, 2007). For thermodynamic properties, as well as for the spintronics effects discussed in Sec. III, the disordered nature of (Ga,Mn)As can, however, play a less significant role. This makes the spin-dependent phenomena and device functionalities discovered and explored in (Ga,Mn)As applicable to a broad class of materials beyond the dilute-moment ferromagnetic semiconductor compounds.

An example of the seemingly surprising similarity between the basic magnetic characteristics of (Ga,Mn)As and the common transition-metal ferromagnets such as Ni is shown in Fig. 4. Here we illustrate that (Ga,Mn)As can have Curie point singularities (Novák *et al.*, 2008; Yuldashev *et al.*, 2010) which are typical of uniform itinerant ferromagnets (Shacklette, 1974; Joynt, 1984). Figure 4(a) shows remanent magnetization $M(T)$ which vanishes sharply at $T \to T_c^-$. For the same 11% Mn-doped sample, Fig. 4(a) also shows the resistivity $\rho(T)$ and its temperature derivative $d\rho/dT$. While $\rho(T)$ has a broad shoulder near $T_c$, $d\rho/dT$ has a singularity at $T_c$ which precisely coincides with $T_c$ inferred from the remanence measurement in the same (Ga,Mn)As material (Novák *et al.*, 2008; Jungwirth *et al.*, 2010; Nemec *et al.*, 2013). We explain below that the Curie point singularity in $d\rho/dT$ is related to the singularity in the specific heat which was also detected in (Ga,Mn)As (Yuldashev *et al.*, 2010) and is shown in Fig. 4(b). The specific heat measurements were performed in lower Mn-doped samples (Ga,Mn)As [2.6% Mn doping in Fig. 4(b)] and therefore the singularity occurs in these samples at a correspondingly lower $T_c$.

FIG. 3 (color online). Density of states for (Ga,Mn)As mixed crystals with various content of Mn obtained in the GGA + *U* theory. The lines represent the total DOS while the shaded areas show the partial density of Mn *d* states. From Mašek *et al.*, 2010.
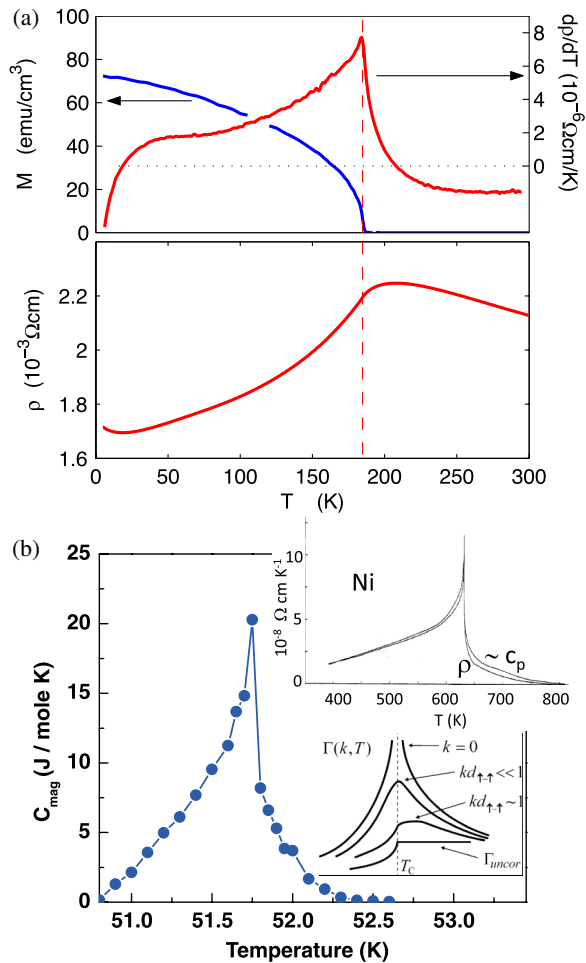
FIG. 4 (color online). (a) Temperature dependent remanent magnetization, resistivity, and temperature derivative of the resistivity of a nominally 11% Mn-doped (Ga,Mn)As. From Jungwirth *et al.*, 2010. (b) Magnetic contribution to the specific heat of a 2.6% Mn-doped (Ga,Mn)As. Adapted from Yuldashev *et al.*, 2010. Upper inset: Temperature derivative of resistance and a multiple of the specific heat plotted against temperature for Ni. From Joynt, 1984. Lower inset: Schematic diagram of the spin-spin correlation function in low and large $k$-vector limits. From Fisher and Langer, 1968.

Since seminal works of de Gennes and Friedel (1958) and Fisher and Langer (1968), critical behavior of resistivity has been one of the central problems in the physics of itinerant ferromagnets. Theories of coherent scattering from long wavelength spin fluctuations, based on the original paper by de Gennes and Friedel, have been used to explain the large peak in the resistivity $\rho(T)$ at $T_c$ observed in Eu-chalcogenide dense-moment magnetic semiconductors (Haas, 1970). The emphasis on the long wavelength limit of the spin-spin correlation function, reflecting critical behavior of the magnetic susceptibility, is justified in these systems by the small density of carriers relative to the density of magnetic moments and corresponding small Fermi wave vectors of carriers.

As pointed out by Fisher and Langer (1968), the resistivity anomaly in high carrier density transition-metal ferromagnets is qualitatively different and associated with the critical behavior of correlations between nearby moments. When

approaching $T_c$ from above, thermal fluctuations between nearby moments are partially suppressed by short-range magnetic order. Their singular behavior is like that of the internal energy and unlike that of the magnetic susceptibility. The singularity at $T_c$ occurs in $d\rho/dT$ and is closely related to the critical behavior of the specific heat. While Fisher and Langer expected this behavior for $T \to T_c^+$ and a dominant role of uncorrelated spin fluctuations at $T \to T_c^-$, later studies of elemental transition metals found a proportionality between $d\rho/dT$ and specific heat on both sides of the Curie point, as shown in the upper inset of Fig. 4(b) (Shacklette, 1974; Joynt, 1984).

The character of the transport anomaly in (Ga,Mn)As is distinct from the critical contribution to transport in the dense-moment magnetic semiconductors (Haas, 1970) and is reminiscent of the $d\rho/dT$ singularity in transition-metal ferromagnets (Shacklette, 1974; Joynt, 1984). Ferromagnetism in (Ga,Mn)As originates from spin-spin coupling between local Mn moments and valence band holes $J\sum_i \delta(\mathbf{r} - \mathbf{R}_i)\boldsymbol{\sigma} \cdot \mathbf{S}_i$ (Dietl, Haury, and d'Aubigne, 1997; Jungwirth *et al.*, 1999; Dietl *et al.*, 2000; Jungwirth, Sinova *et al.*, 2006). Here $\mathbf{S}_i$ represents the local spin and $\boldsymbol{\sigma}$ is the hole spin operator. This local-itinerant exchange interaction plays a central role in theories of the critical transport anomaly. When treated in the Born approximation, the interaction yields a carrier scattering rate from magnetic fluctuations, and the corresponding contribution to $\rho(T)$, which is proportional to the static spin-spin correlation function $\Gamma(\mathbf{R}_i, T) \sim J^2[\langle \mathbf{S}_i \cdot \mathbf{S}_0 \rangle - \langle \mathbf{S}_i \rangle \cdot \langle \mathbf{S}_0 \rangle]$ (de Gennes and Friedel, 1958). Typical temperature dependences of the uncorrelated part $\Gamma_{\mathrm{uncor}}(\mathbf{R}_i, T) \sim \delta_{i,0} J^2[S(S+1) - \langle \mathbf{S}_i \rangle^2]$ and of the Fourier components of the correlation function $\Gamma(\mathbf{k}, T) = \sum_{i \neq 0} \Gamma(\mathbf{R}_i, T) \exp(\mathbf{k} \cdot \mathbf{R}_i)$ are illustrated in the lower inset of Fig. 4(b) (Fisher and Langer, 1968). At small wave vectors, $\Gamma(\mathbf{k}, T)$ and correspondingly $\rho(T)$ have a peak at $T_c$. At $k$ similar to the inverse separation of the local moments ($kd_{\uparrow-\uparrow} \sim 1$) the peak broadens into a shoulder while the singular behavior at $T_c$ is in the temperature derivative of the spin-spin correlator and, therefore, in $d\rho/dT$.

$M^2$ expansion providing a good fit to the magnetic contribution to the resistivity at $T < T_c$ (Novák *et al.*, 2008) corresponds to the dominant contribution from $\Gamma_{\mathrm{uncor}}$ on the ferromagnetic side of the transition. The shoulder in $\rho(T)$ on the paramagnetic side and the presence of the singularity in $d\rho/dT$ suggest that large wave-vector components of $\Gamma(\mathbf{k}, T)$ dominate the temperature dependence of the scattering in the $T \to T_c^+$ critical region (Novák *et al.*, 2008). The large $k$-vector limit is consistent with the ratio between hole and Mn local-moment densities approaching unity in high-quality (Ga,Mn)As materials with low charge compensation by unintentional impurities (Nemec *et al.*, 2013).

### 2. Localization effects in transport

While the sharp transport Curie point singularities highlight the fact that ferromagnetic (Ga,Mn)As epilayers can have a high degree of uniformity (Kodzuka *et al.*, 2009) and can behave similarly to common, weakly disordered itinerant ferromagnets, the magnitude of the resistivity at zero and finite frequencies and over the broad temperature range is significantly affected by the vicinity of the metal-insulator

transition in (Ga,Mn)As. The valence band calculations treating disorder in the first-order Born approximation over-estimate the experimental conductivities of metallic (Ga,Mn) As by up to a factor of 10 (Jungwirth *et al.*, 2002; Sinova *et al.*, 2002). This discrepancy is removed by accounting for strong disorder and localization effects using, e.g., exact-diagonalization calculations (Yang *et al.*, 2003; Jungwirth *et al.*, 2007). Even the most metallic (Ga,Mn)As materials with delocalized carriers at the Fermi level may contain localized states in the valence band tail which modify the finite-frequency absorption spectra (Burch *et al.*, 2006; Jungwirth *et al.*, 2007, 2010; Chapler *et al.*, 2011).

The low diffusivity of carriers implies that quantum interference and electron-electron interactions can produce sizable effects in (Ga,Mn)As. Weak localization (WL) quantum corrections are due to constructive interference between partial waves undergoing multiple scattering from a state with wave vector $k$ to a state $-k$ and partial waves traversing the time-reversed trajectory. The effect is also referred to as coherent backscattering and it leads to a reduction of the conductivity. A distinct, electron-electron interaction quantum correction to the conductivity (Lee and Ramakrishnan, 1985) can arise in disordered conductors which often has a similar magnitude to the WL correction. This arises because electron-electron interactions cannot be treated independently of the disorder scattering for strong disorder.

Explicit expressions for the WL corrections can be obtained for $L_\Phi \gg \Lambda \gg \lambda_F$, where $L_\Phi$, $\Lambda$, and $\lambda_F$ are the carrier phase coherence length, mean free path, and Fermi wavelength. The second condition can be rewritten as $k_F \Lambda \gg 1$, where $k_F$ is the Fermi wave vector. The corrections are of the order of $(k_F \Lambda)^{-1}$ and so become important for small $k_F \Lambda$. It has been argued that higher order corrections are small and that the condition $k_F \Lambda \gg 1$ can be relaxed to $k_F \Lambda > 1$. Application of a magnetic field can suppress the resistance enhancement due to WL as it removes time-reversal invariance leading to negative magnetoresistance. The magnetic field begins to have a significant effect when $\ell_B \sim L_\Phi$, where $\ell_B = (\hbar/eB)^{1/2}$ is the magnetic length, and the magnetic field completely suppresses WL when $\ell_B \sim \Lambda$. Since WL quantum corrections are suppressed by sufficiently large magnetic fields one expects a similar suppression by the internal magnetization. For dense-moment ferromagnets like Fe, Ni, etc., $\mu_0 M \sim 2$ T and the mean free path is usually quite large so WL is strongly suppressed. However, WL is observed, for example, in highly disordered Ni films (Aprili *et al.*, 1997). For the dilute-moment ferromagnet (Ga,Mn)As, $\mu_0 M \sim$ 50 mT while the field needed to suppresses WL, i.e., when $\ell_B \sim \Lambda \sim 1$ nm, is $\sim$1000 T. So one expects WL effects to be present, and since typically $k_F \Lambda \sim 1$–10, they may be large.

The identification of WL contributions to the temperature dependence of resistance is difficult as they generally coexist with other temperature dependent contributions and because the expected functional form can be very different for the different possible phase breaking mechanisms. In disordered ferromagnets like (Ga,Mn)As, spin-disorder scattering can, e.g., produce large magnetoresistance, particularly close to the localization boundary (Kramer and MacKinnon, 1993; Nagaev, 1998; Omiya *et al.*, 2000).
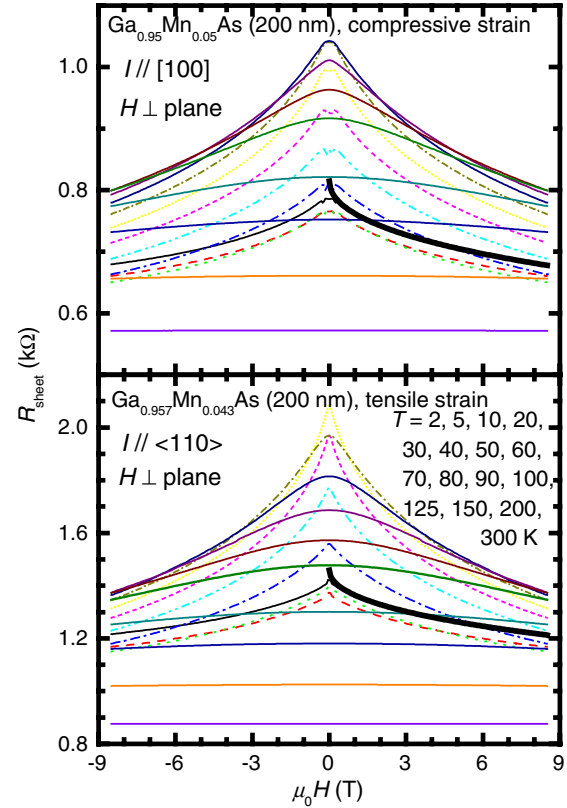


FIG. 5 (color online). Field and temperature dependences of resistance in $Ga_{0.95}Mn_{0.05}As/GaAs$ (compressive strain, upper panel) and in tensile strained $Ga_{0.957}Mn_{0.043}As/(In,Ga)As$ (lower panel) for magnetic field perpendicular to the film plane. Starting from the top, subsequent curves at $B = 0$ correspond to temperatures in K: 70, 60, 80, 50, 90, 40, 100, 30, 125, 20, 2, 5, 10, 150, 200, 300 (upper panel) and to 50, 60, 40, 70, 30, 80, 90, 20, 100, 2, 10, 5, 125, 150, 200, 300 (lower panel). From Matsukura *et al.*, 2004.

For external magnetic fields less than the coercive fields the magnetoresistance response is usually dominated by AMR (see Secs. III.A and III.B). At larger fields a negative isotropic magnetoresistance is observed which can be very large for low conductivity material (Matsukura *et al.*, 2004). This could be due to the suppression of spin disorder (Lee, Stone, and Fukuyama, 1987). However, as shown in Fig. 5 (Matsukura *et al.*, 2004), the negative magnetoresistance does not seem to saturate, even in extremely strong magnetic fields. It has been argued (Matsukura *et al.*, 2004) that the negative magneto-resistance arises from WL and gives a correction consistent with the predicted form proportional to $-B^{1/2}$ (Kawabata, 1980), which assumes a complete suppression of spin-disorder and spin-orbit scattering (see Fig. 5).

The role of spin-orbit coupling in WL phenomena in (Ga,Mn)As has been extensively discussed (Neumaier *et al.*, 2007; Rokhinson *et al.*, 2007; Garate, Sinova *et al.*, 2009). In the context of the spintronic phenomena and functionalities in (Ga,Mn)As and their applicability to other materials, discussed in Sec. III, an important conclusion is drawn from numerical studies of WL in (Ga,Mn)As (Garate, Sinova *et al.*, 2009). They showed that while WL corrections can significantly contribute to the absolute residual resistivity, the

relative changes in resistivity associated with magnetization reorientations, namely, the AMR ratios, are nearly independent on whether the WL corrections are included or not (Garate, Sinova *et al.*, 2009). These results, which agree qualitatively with analytical considerations on simpler models (Bhatt, Wolfle, and Ramakrishnan, 1985), illustrate that the intrinsically strong disorder in (Ga,Mn)As can qualitatively play a minor role in not only the thermodynamic properties but also in the spintronic phenomena reflecting the interactions of carrier spins with electrical current, light, or heat. What determines these phenomena is primarily the magnetic exchange and spin-orbit fields acting on the carrier states. Disorder can mix the carrier states but as long as this mixing does not significantly alter the effects of the exchange field and spin-orbit coupling on the carriers the spintronic phenomena remain robust against disorder. This explains the qualitative and often semiquantitative success, and justifies the applicability, of microscopic theories of spintronic phenomena in (Ga,Mn)As starting from a Bloch-band description of the material's electronic structure. Simultaneously it should be noted that due to strong disorder and the vicinity of the metal-insulator transition a full quantitative description is unlikely to be achievable within any of the existing theoretical models of (Ga,Mn)As.

We conclude this section by discussing the universal conductance fluctuations (UCFs) in (Ga,Mn)As. These result from the interference between partial waves from scattering centers within a conductor. In the usual semiclassical theory of electron conduction this is neglected since it is assumed that such effects will be averaged away. However, for conductors of size comparable with $L_\Phi$ the interference effects are intrinsically non-self-averaging. This leads to corrections to the conductivity of order $e^2/h$. Application of a magnetic field modifies the interference effects, giving reproducible but aperiodic UCFs (Lee, Stone, and Fukuyama, 1987) of amplitude $\sim e^2/h$. One can think of a conductor with dimensions $> L_\Phi$ as made up of a number of independent phase coherent subunits leading to averaging. UCFs are then diminished for dimensions $\gg L_\Phi$ and only WL due to the coherent backscattering may still contribute in macroscopic samples.

At temperatures which are a significant fraction of the Curie temperature one expects spin-disorder and spin-orbit scattering to lead to the phase coherence length $L_\Phi \sim \Lambda$, strongly suppressing quantum corrections. However, in high-quality metallic (Ga,Mn)As it has been argued (Matsukura *et al.*, 2004) that $L_\Phi$ need not be very small at low temperatures because virtually all spins contribute to the ferromagnetic ordering and the large splitting of the valence band makes both spin-disorder and spin-orbit scattering relatively inefficient. The strong magnetocrystalline anisotropies also tend to suppress magnon scattering at low temperatures.

Recent observations (Wagner *et al.*, 2006; Vila *et al.*, 2007) of large UCFs in (Ga,Mn)As microdevices, and the evidence for the closely related Aharonov-Bohm effect (ABE) in (Ga,Mn)As microrings, confirm that $L_\Phi$ can be large at low temperatures. Figure 6 shows UCFs measured (Wagner *et al.*, 2006) in (Ga,Mn)As wires of approximate width 20 nm and thickness 50 nm. Figure 6(a) shows that the UCF amplitude is $\sim e^2/h$ in a 100 nm long wire at 20 mK. This directly demonstrates that $L_\Phi \sim 100$ nm. Similar measurements in
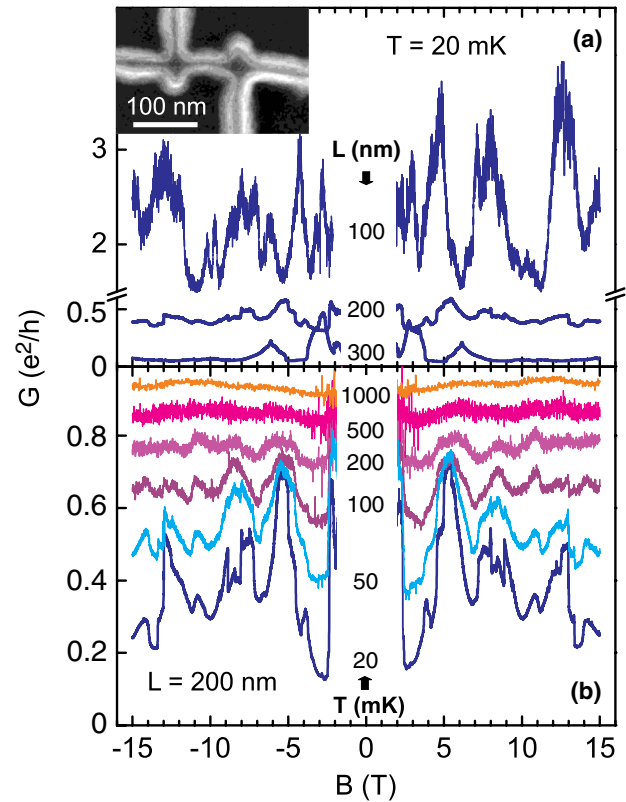


FIG. 6 (color online). (a) Conductance fluctuations for three wires of different length $L$. For the shortest wire the amplitude of the conductance fluctuations is about $e^2/h$, expected for conductors with all spatial dimensions smaller or comparable to $L_\Phi$. The inset shows an electron micrograph of a 20 nm wide wire with a potential probe separation of $\sim 100$ nm. (b) Conductance vs magnetic field of the 200 nm wire for different temperatures between 20 mK and 1 K. From Wagner *et al.*, 2006.

higher conductivity (Ga,Mn)As give $L_\Phi \sim 100$ nm at 100 mK. These are large values corresponding to a phase relaxation time that is orders of magnitude larger than the elastic scattering time.

Figure 7 shows measurements (Wagner *et al.*, 2006) of the magnetic field dependence of the conductivity of a lithographically defined 100 nm diameter (Ga,Mn)As ring compared to that of a 200 nm long (Ga,Mn)As wire. Additional small period oscillations are observed for the ring which the Fourier transform shows to be consistent with the expected ABE period. This confirms the long $L_\Phi$ indicated by the large amplitude UCFs and confirms that almost all spins are participating in the magnetic order with strong suppression of spin scattering.

### B. Doping trends in basic magnetic and transport properties of (Ga,Mn)As

#### 1. Low Mn-doped bulk materials

Narrow impurity bands have been clearly observed in Mn-doped GaAs samples with carrier densities much lower than the metal-insulator transition density, for example, in equilibrium grown bulk materials with Mn density $c = 10^{17}$–$10^{19}$ cm$^{-3}$ (Brown and Blakemore, 1972; Blakemore
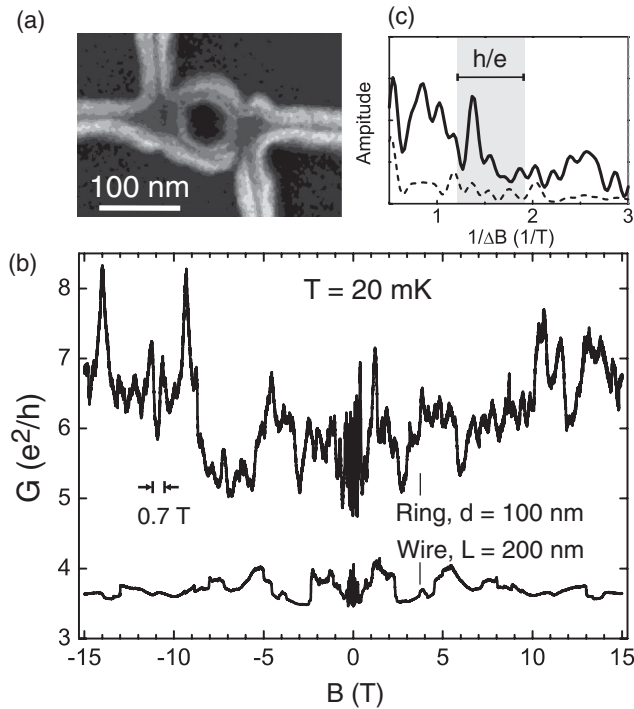
FIG. 7.   (a) Electron micrograph of a (Ga,Mn)As ring sample with a diameter of ~100 nm. (b) Comparison of the magnetoconductance trace of the ring sample with the conductance of a wire of comparable length and 20 nm width. (c) The corresponding Fourier transform taken from the conductance of the ring and wire. The region where ABE oscillations are expected is highlighted. From Wagner *et al.*, 2006.



FIG. 8 (color online).    (a) Magnetization $M$, temperature derivative of the resistivity normalized to the peak value $(d\rho/dT)^*$, and resistivity $\rho(T)$ of an optimized 20 nm thick epilayer with 7% nominal Mn doping. (b), (c) Frequency dependence of the damping factor and field dependence of the SWR frequencies of the same sample. (d)–(f) Same as (a)–(c) for a material differing by having only one of the synthesis parameters not optimized (epilayer thickness of 500 nm is too large). From Nemec *et al.*, 2013.

*et al.*, 1973; Woodbury and Blakemore, 1973). The energy gap between the impurity band and the valence band $E_a$ can be measured by studying the temperature dependence of longitudinal and Hall conductivities, which show activated behavior because of thermal excitation of holes from the impurity band to the much more conductive valence band (Blakemore *et al.*, 1973; Woodbury and Blakemore, 1973; Marder, 2000).

The activation energy decreases with increasing Mn density (Blakemore *et al.*, 1973). The lowering of impurity binding energies at larger $c$, which is expected to scale with the mean impurity separation, is apparent already in the equilibrium grown bulk materials with $c = 10^{17}$–$10^{19}$ cm$^{-3}$. The degenerate semiconductor regime was, however, not reached in the bulk materials.

### 2. Synthesis of high Mn-doped epilayers

A comprehensive experimental assessment of basic doping trends including the regimes near and above the insulator-to-metal transition became possible since the late 1990s with the development of LT-MBE (Ga,Mn)As films (Ohno, 1998). The epilayers can be doped well beyond the equilibrium Mn solubility limit while avoiding phase segregation and maintaining a high degree of uniformity (Kodzuka *et al.*, 2009). Because of the highly nonequilibrium nature of the heavily doped ferromagnetic (Ga,Mn)As, the growth and postgrowth annealing procedures have to be individually optimized for
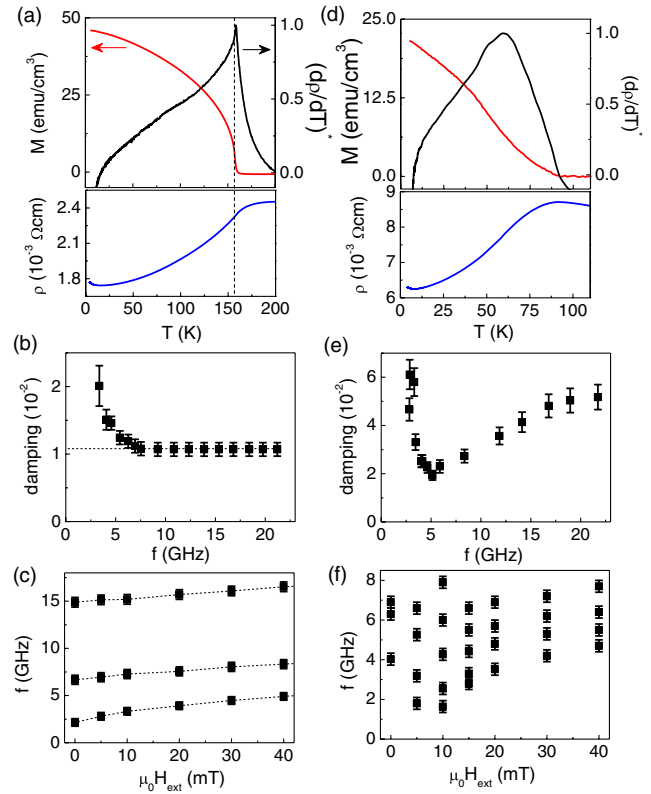
each Mn-doping level in order to obtain films which are as close as possible to idealized uniform (Ga,Mn)As mixed crystals with the minimal density of compensating and other unintentional defects. This is illustrated in Fig. 8 showing, side by side, basic electrical and magnetic characteristics of two medium, 7% Mn-doped epilayers (Nemec *et al.*, 2013). The left column shows data measured on a material which was prepared under optimized conditions for the given nominal Mn doping. The sample has sharp Curie point singularities in magnetization and $d\rho/dT$ [Fig. 8(a)]. The magnetization precession damping factor and spin-wave resonances (SWRs) obtained from magneto-optical measurements [Figs. 8(b), and 8(c)] confirm the high magnetic quality of the material. The initial decrease of the damping factor with frequency followed by a frequency independent part [Fig. 1(b)] is typical of uniform ferromagnets (Walowski *et al.*, 2008). It allows one to accurately separate the intrinsic Gilbert damping constant $\alpha$, corresponding to the frequency independent part, from effects that lead to inhomogeneous broadening of ferromagnetic resonance (FMR) linewidths. Similarly, the observed Kittel SWR modes of a uniform ferromagnet [Fig. 1(c)] allows one to accurately measure the magnetic anisotropy and spin-stiffness parameters of (Ga,Mn)As.

The right column data [Figs. 8(d)–8(f)] were measured on a 7% Mn-doped epilayer differing from the sample of the left column in only one of the synthesis parameters not being optimized. The stoichiometry, substrate growth temperature, postgrowth annealing temperature and time, and epilayer thickness are among the key synthesis parameters. All these parameters were equally optimized in the two samples except for the epilayer thickness. In the medium and high Mn-doped samples, full material optimization is possible only for film thicknesses $\lesssim 50$ nm. The epilayer whose measurements are shown in the right panels of Fig. 8 is 500 nm thick. Its magnetization and transport Curie point singularities are largely smeared out, the damping factor is strongly frequency dependent, and an alternating number of SWRs is observed with increasing applied field whose spacings are inconsistent with Kittel modes. The material is nonuniform, the magnetization and transport data indicate strong moment and charge compensation by extrinsic impurities, and for this material it is impossible to reliably extract any of the intrinsic micromagnetic parameters of (Ga,Mn)As.

In Fig. 9 we illustrate the fact that even in films thinner than 50 nm apparently small changes in the remaining key
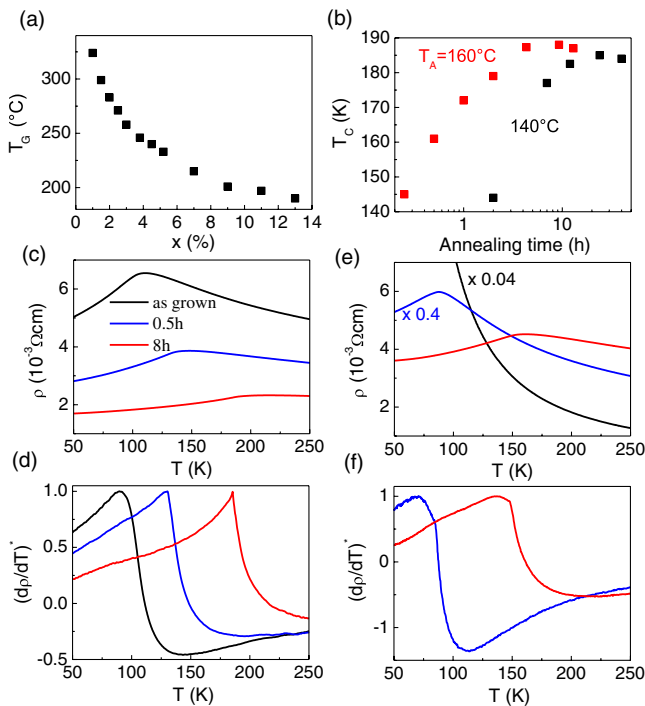


FIG. 9 (color online). (a) Optimal growth temperature $T_G$ as a function of the nominal Mn doping $x$. (b) Dependence of the Curie temperature $T_c$ on the annealing time for two different annealing temperatures $T_A$ in a 15 nm thick (Ga,Mn)As epilayer with 13% nominal Mn doping grown at optimal $T_G$. (c), (d) $\rho(T)$ and $(d\rho/dT)^*$ in the $x = 13\%$ epilayer grown at optimal $T_G$ in the as-grown state, for optimal $T_A$ and annealing time 0.5 h, and for optimal $T_A$ and optimal annealing time of 8 h. (e), (f) Same as (c), (d) for a $x = 13\%$ epilayer grown at 10° below the optimal $T_G$; $(d\rho/dT)^*$ is not plotted for the as-grown insulating and paramagnetic sample. From Nemec *et al.*, 2013.

synthesis parameters can significantly affect the material quality (Nemec *et al.*, 2013). Staying near the 1:1 stoichiometric As : (Ga + Mn) ratio is favorable for the LT-MBE growth of (Ga,Mn)As (Myers *et al.*, 2006; Wang *et al.*, 2008). Figure 9(a) shows the optimal growth temperature $T_G$ for the stoichiometric growth as a function of the nominal Mn doping $x$. The optimal $T_G$ remains near (from the lower temperature side) the 2D/3D growth-mode boundary which implies its strong dependence on $x$. Figure 9(b) shows $T_c$ as a function of the annealing time for the optimal $T_G = 190\,^\circ\text{C}$ for the 13% Mn-doped sample and for two annealing temperatures. One is the optimal annealing temperature $T_A = 160\,^\circ\text{C}$ and the other one is 20° lower. The maximum $T_c = 188$ K sample is obtained by simultaneously optimizing the annealing time and $T_A$. Figures 9(c) and 9(d) illustrate how the increasing $T_c$ is accompanied by the improving material quality (reduction of extrinsic compensation and sample inhomogeneity) over the annealing time for optimal $T_G$ and $T_A$. The importance of the optimal $T_G$ during the growth is highlighted in Figs. 9(e) and 9(f) showing the same annealing sequence measurements as in Figs. 9(c) and 9(d) on a 13% doped sample grown at a temperature of only 10° below the optimal $T_G$. In contrast to the material grown at the optimal $T_G$, the sample is insulating and paramagnetic in the as-grown state. Ferromagnetism and metallic conduction can be recovered by annealing; however, the compensation and inhomogeneity cannot be removed and the ferromagnetic transition temperature remains tens of degrees below the $T_c$ of the sample grown at the optimal $T_G$. Similarly lower quality samples are obtained by growing at higher than optimal $T_G$.

Figures 8 and 9 illustrate the following general conclusions drawn from extensive material optimization studies (Nemec *et al.*, 2013). Inferring doping trends in basic material properties of (Ga,Mn)As from sample series mixing as-grown and annealed materials is unsuitable as the quality of the samples may strongly vary in such a series. Choosing one *a priori* fixed $T_G$, $T_A$, and annealing time for a range of Mn dopings is unlikely to produce a high-quality, uniform and uncompensated (Ga,Mn)As material even for one of the considered dopings and is bound to produce low-quality samples for most of the studied Mn dopings. Finally, optimized (Ga,Mn)As samples require exceedingly long annealing times for film thicknesses $\gtrsim 50$ nm and are impossible to achieve in $\sim 100$ nm and thicker films by the known (Ga,Mn)As synthesis approaches.

When limited attention is paid to the details of the synthesis of the highly nonequilibrium (Ga,Mn)As alloy, seemingly contradictory experimental results can be found in these materials (Burch *et al.*, 2006; Tang and Flatté, 2008; Dobrowolska, Liu *et al.*, 2012; Dobrowolska, Tivakornsasithorn *et al.*, 2012) as compared to measurements on samples prepared under the above optimized growth conditions (Jungwirth *et al.*, 2010; Wang *et al.*, 2013). As an example we show in Fig. 10 measurements of $T_c$ versus hole density $p$ (Dobrowolska, Tivakornsasithorn *et al.*, 2012; Wang *et al.*, 2013). The data are normalized to $x_\text{eff}$ ($N_\text{eff} = 4x_\text{eff}/a^3$) representing the concentration of Mn magnetic moments which contribute to the magnetic order. The results obtained by Dobrowolska, Tivakornsasithorn *et al.* (2012) indicated a strong suppression of $T_c$ in (Ga,Mn)As layers with close to one hole per
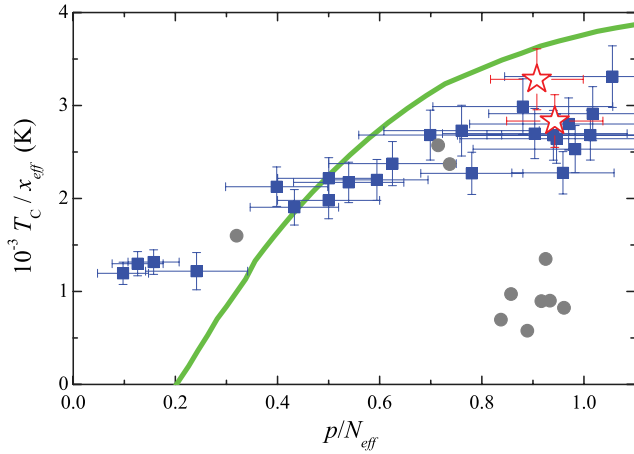
FIG. 10 (color online). Curie temperature $T_c$ vs hole density $p$ normalized to $x_{eff}$ ($N_{eff} = 4x_{eff}/a^3$) representing the concentration of Mn magnetic moments which contribute to the magnetic order. The squares correspond to samples from Wang *et al.* (2013) prepared under optimized growth conditions where the hole density $p$ is obtained from high-field Hall measurements. The circles correspond to samples from Dobrowolska, Tivakornsasithorn *et al.* (2012), where $p$ is obtained from ion channeling measurements. The stars correspond to samples from Rushforth, Farley *et al.* (2008) prepared under optimized growth conditions, where $p$ is obtained from ion channeling measurements. The line is the prediction of the microscopic calculation of Jungwirth *et al.* (2005).

substitutional Mn. It was thus suggested that $T_c$ in ferromagnetic (Ga,Mn)As is determined by the location of the Fermi level within a narrow impurity band, separated from the valence band. On the other hand, experiments on epilayers prepared under the optimized growth conditions found that $T_c$ takes its largest values in weakly compensated samples when $p$ is comparable to the concentration of substitutional Mn acceptors. This is inconsistent with models in which the Fermi level is located within a narrow isolated impurity band and corroborates predictions for $T_c$ of the above discussed microscopic theories (see Fig. 10) in which valence and impurity bands are merged in ferromagnetic (Ga,Mn)As.

Reliable measurements of systematic doping trends in intrinsic semiconducting and magnetic properties of materials which represent as close as possible idealized uniform (Ga,Mn)As mixed crystals with the minimal density of compensating and other unintentional defects require the careful optimization of the synthesis. Many studies of the spintronics phenomena in (Ga,Mn)As, discussed in Sec. III, have also benefited from the high-quality optimized epilayers. This applies, in particular, to experiments sensitive to small tilts of carrier spins from the equilibrium direction which is the case, e.g., of the magneto-optical phenomena observed in the pump-and-probe experiments discussed in Sec. III.C. While for the detailed analysis the optimally synthesized and thoroughly characterized (Ga,Mn)As epilayers are always favorable, many of the spintronics effects and functionalities have been demonstrated in materials with extrinsic disorder not fully removed from the film. As shown in Figs. 8 and 9 these materials can still

be ferromagnetic and conductive and as discussed in Secs. II.A.1 and II.A.2 the spintronics phenomena can be, at least on a qualitative level, relatively robust against strong disorder, whether intrinsic or extrinsic.

### 3. Curie temperature and conductivity

Uniform (Ga,Mn)As materials with minimized extrinsic disorder can be divided into the following groups: at nominal dopings below $\sim 0.1\%$ the (Ga,Mn)As materials are paramagnetic, strongly insulating, showing signatures of the activated transport corresponding to valence band–impurity band transitions at intermediate temperatures, and valence band–conduction band transitions at high temperatures [see Fig. 11(a)] (Jungwirth *et al.*, 2007; Nemec *et al.*, 2013). For higher nominal dopings, $0.5 \lesssim x \lesssim 1.5\%$, no clear signatures of activation from the valence band to the impurity band are seen in the dc transport, indicating that the bands start to overlap and mix, yet the materials remain insulating. At $x \approx 1.5\%$, the low-temperature conductivity of the film increases abruptly by several orders of magnitude [see Fig. 11(b)], and the system turns into a degenerate semiconductor. The onset of ferromagnetism occurs already on the insulating side of the transition at $x \approx 1\%$. All ferromagnetic samples over a broad nominal Mn-doping range can have sharp Curie point singularities when synthesized under
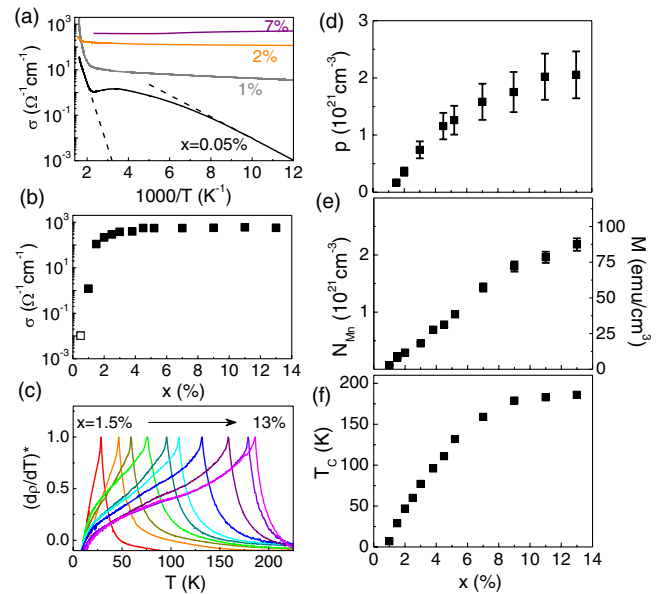


FIG. 11 (color online). (a) Temperature dependence of the conductivity $\sigma(T)$ of optimized (Ga,Mn)As epilayers with depicted nominal Mn doping. Dashed lines indicate the activated parts of $\sigma(T)$ of the insulating paramagnetic (Ga,Mn)As with 0.05% Mn doping, corresponding to the Mn acceptor level and the band gap, respectively. (b) Conductivity at 4 K as a function of the nominal Mn doping. The open symbol corresponds to a paramagnetic sample. (c) Sharp Curie point singularities in the temperature derivative of the resistivity in the series of optimized ferromagnetic (Ga,Mn)As epilayers with metallic conduction. (d)–(f) Hole density $p$, magnetization $M$ and corresponding Mn-moment density $N_{Mn}$, and Curie temperature $T_c$ as a function of the nominal Mn doping in the series of optimized (Ga,Mn)As epilayers. From Nemec *et al.*, 2013.
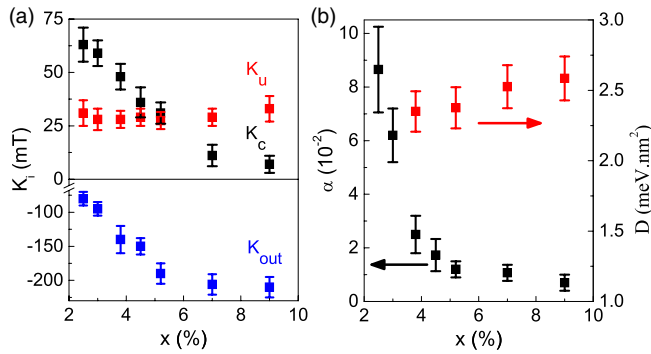
FIG. 12 (color online). (a) Dependence of magnetic anisotropy constants on nominal Mn doping. (b) Dependence of the Gilbert damping constant $\alpha$ and the spin-stiffness constant $D$ on nominal Mn doping. Measurements were performed at 15 K. From Nemec *et al.*, 2013.

individually optimized growth and postgrowth annealing conditions [see Fig. 11(c)].

The hole concentration $p$ can be measured by the slope of the Hall curve at high fields with an error bar due to the multiband nature estimated to ∼20% (Jungwirth *et al.*, 2005). Within this uncertainty, the overall trend shows increasing $p$ with increasing doping in the optimized materials, as shown in Fig. 11(d). Similarly, the saturation moment and $T_c$ steadily increase with increasing nominal doping up to $x \approx 13\%$, as shown in Figs. 11(e) and 11(f). Assuming $4.5\mu_B$ per Mn atom (Jungwirth *et al.*, 2006) the density $c \equiv N_{Mn}$ of uncompensated $Mn_{Ga}$ moments can be inferred from the magnetization data [see the left $y$ axis in Fig. 11(e)]. Since there is no apparent deficit of $p$ compared to $N_{Mn}$, and since the interstitial Mn impurity (Edmonds *et al.*, 2002; Máca and Mašek, 2002; Yu *et al.*, 2002) compensates one local moment but two holes it can be concluded that interstitial Mn, which is the key contributor to extrinsic disorder, is removed in the optimally grown and annealed epilayers. Hence, a broad series of optimized (Ga,Mn) As materials can be prepared with reproducible characteristics, showing an overall trend of increasing saturation moment with increasing $x$, increasing $T_c$ (reaching 188 K), and increasing hole density. The materials have no measurable charge or moment compensation of the substitutional $Mn_{Ga}$ impurities and have a large degree of uniformity.

Figure 12 demonstrates that the intrinsic micromagnetic parameters of (Ga,Mn)As measured on the optimized materials show also a smooth monotonic doping dependence (Nemec *et al.*, 2013). As detailed below, their values are characteristic of common band ferromagnets and all the semiconducting and magnetic properties summarized in Figs. 11 and 12 are consistent with the microscopically established electronic structure of (Ga,Mn)As. The control and reproducibility of material properties of (Ga,Mn)As have been confirmed in the optimized films by multiple material synthesis and characterization experiments in different MBE chambers (Nemec *et al.*, 2013; Wang *et al.*, 2013).

## 4. Micromagnetic parameters

Micromagnetic parameters of (Ga,Mn)As and related (III,Mn)V ferromagnetic semiconductors were studied by

magnetization, magnetotransport, magneto-optical, or ferromagnetic or spin-wave resonance (FMR or SWR) measurements (Munekata *et al.*, 1993; Ohno, 1998; Abolfath *et al.*, 2001; Dietl, Ohno, and Matsukura, 2001; Potashnik *et al.*, 2002; Rappoport *et al.*, 2004; Sinova, Jungwirth *et al.*, 2004; Sawicki *et al.*, 2005; Gourdon *et al.*, 2007; Hümpfner *et al.*, 2007; Liu, Zhou, and Furdyna, 2007; Pappert *et al.*, 2007; Wang *et al.*, 2007a; Wenisch *et al.*, 2007; Wunderlich *et al.*, 2007; Zhou *et al.*, 2007; Chiba *et al.*, 2008; Goennenwein *et al.*, 2008; Gould *et al.*, 2008; Khazen *et al.*, 2008; Overby *et al.*, 2008; Rushforth *et al.*, 2008; Rushforth, Wang *et al.*, 2008; Stolichnov *et al.*, 2008; Bihler *et al.*, 2009; Owen *et al.*, 2009; Zemen *et al.*, 2009; Cubukcu, von Bardeleben, Cantin, and Lemaitre, 2010; Cubukcu, von Bardeleben, Khazen *et al.*, 2010; Haghgoo *et al.*, 2010; Werpachowska and Dietl, 2010; De Ranieri *et al.*, 2013; Nemec *et al.*, 2013). A large experimental scatter of the measured micromagnetic parameters can be found in the literature which partly reflects the issues related to the control of extrinsic disorder in the synthesis of (Ga,Mn)As. The experimental scatter also reflects, however, the favorable intrinsic tunability of (Ga,Mn)As properties by varying the temperature, hole and Mn-moment densities, III-V substrate on which the (Ga,Mn) As film is deposited, or by alloying the magnetic film with other III or V elements, by device microfabrication, by applying electrostatic or piezoelectric fields on the film, etc.

When measuring the micromagnetic parameters on the optimally and consistently synthesized series of bare (Ga,Mn)As epilayers on a GaAs substrate, fully reproducible and systematic trends can be inferred when simultaneously determining the magnetic anisotropy $K_i$, Gilbert damping $\alpha$, and spin-stiffness $D$ constants from one set of measurements. This has been demonstrated, e.g., on a series of (Ga, Mn)As/ GaAs epilayers over a broad range of Mn dopings by employing the magneto-optical pump-and-probe technique, as shown in Fig. 12 (Nemec *et al.*, 2013).

The magnetic anisotropy fields are dominated by three components. The out-of-plane component $K_{out}$ is a sum of the thin-film shape anisotropy and the magnetocrystalline anisotropy due to the substrate lattice-matching growth strain. In (Ga,Mn)As grown on GaAs the strain in the (Ga,Mn)As epilayer is compressive and $K_{out}$ favors for most Mn dopings in-plane magnetization [see Fig. 12(a)]. However, when using an InGaAs substrate or adding phosphorus into the magnetic film, the growth strain can change from compressive to tensile, $K_{out}$ flips sign, and the film turns into an out-of-plane ferromagnet (Abolfath *et al.*, 2001; Dietl, Ohno, and Matsukura, 2001; Yamanouchi *et al.*, 2004; Rushforth, Wang *et al.*, 2008; Cubukcu, von Bardeleben, Khazen *et al.*, 2010). This transition from an in-plane to an out-of-plane magnet has been exploited, e.g., in studies of the current-induced domain wall motion and spin-orbit torque discussed in Secs. III.B.6 and III.B.7 (Yamanouchi *et al.*, 2004; Wang *et al.*, 2010; Fang *et al.*, 2011; Curiale *et al.*, 2012; De Ranieri *et al.*, 2013).

The cubic magnetocrystalline anisotropy $K_c$ reflects the zinc-blende crystal structure of the host semiconductor. The origin of the additional uniaxial anisotropy component along the in-plane diagonal $K_u$ is associated with a more subtle symmetry breaking mechanism introduced during the epilayer

growth (Kopecky *et al.*, 2011; Mankovsky *et al.*, 2011; Birowska *et al.*, 2012). The sizable magnitudes of $K_c$ and $K_u$ and the different doping trends of these two in-plane magnetic anisotropy constants [see Fig. 12(a)] are crucial for the micromagnetics of the in-plane magnetized (Ga,Mn)As materials. The cubic anisotropy $K_c$ dominates at very low dopings and the easy axis (EA) aligns with the main crystal axis [100] or [010]. At intermediate dopings, the uniaxial anisotropy $K_u$ is still weaker but comparable in magnitude to $K_c$. In these samples the two equilibrium easy axes are tilted toward the $[1\bar{1}0]$ direction and their angle is sensitive to changes of temperature [the ratio of $K_u/K_c$ tends to increase with temperature (Wang, Sawicki *et al.*, 2005)] or externally applied electrostatic or piezovoltages which have been exploited in numerous studies of spintronics effects and device functionalities in (Ga,Mn)As (Ohno *et al.*, 2000; Chiba *et al.*, 2003, 2008; Goennenwein *et al.*, 2008; Olejník *et al.*, 2008; Overby *et al.*, 2008; Rushforth *et al.*, 2008; Stolichnov *et al.*, 2008; Owen *et al.*, 2009; De Ranieri *et al.*, 2013). The origin of the magnetocrystalline anisotropies is in the spin-orbit coupling of the valence band holes mediating the ferromagnetic Mn-Mn coupling, as described on a qualitative or semiquantitative level by the model, kinetic-exchange Hamiltonian theory (Abolfath *et al.*, 2001; Dietl, Ohno, and Matsukura, 2001; Zemen *et al.*, 2009).

A systematic doping trend of the Gilbert damping constant is also found across the series of optimized materials [see Fig. 12(b)]. The magnitudes of $\alpha \sim 0.1 - 0.01$ and the doping dependence are consistent with Gilbert damping constants in conventional transition-metal ferromagnets. In metals, $\alpha$ typically increases with increasing resistivity and is enhanced in alloys with enhanced spin-orbit coupling (Ingvarsson *et al.*, 2002; Rantschler *et al.*, 2007; Gilmore, Idzerda, and Stiles, 2008). Similarly in (Ga,Mn)As the increase of $\alpha$ correlates with an increase of the resistivity in the lower Mn-doped samples. Moreover, the spin-orbit coupling effects tend to be stronger in the lower doped samples with lower filling of the hole bands and with the carriers closer to the metal-insulator transition. Theory ascribing magnetization relaxation to the kinetic-exchange coupling of Mn moments with the spin-orbit coupled holes yields a comparable range of values of $\alpha$ as observed in experiment [see Fig. 12(b)] (Sinova, Jungwirth *et al.*, 2004; Nemec *et al.*, 2013).

The direct measurement of the spin stiffness requires a rather delicate balance between thin enough epilayers whose material quality can be optimized and thick enough films allowing one to observe the higher-index Kittel spin-wave modes (Kittel, 1958) of a uniform thin-film ferromagnet. The magneto-optical pump-and-probe technique (Nemec *et al.*, 2013) has an advantage that, unlike FMR, it is not limited to odd index spin-wave modes (Kittel, 1958). The ability to excite and detect the $n = 0, 1$, and 2 resonances is essential for the observation of the Kittel modes in the optimized (Ga,Mn)As epilayers whose thickness $L$ is limited to $\sim 50$ nm. The modes in the optimized films show the expected quadratic scaling with $n$ and with $1/L$, and could be fitted by one set of magnetic anisotropy constants and spin-stiffness constant $D$ (Nemec *et al.*, 2013). In the optimized series of (Ga,Mn)As epilayers a consistent, weakly increasing trend in $D$ with increasing doping is observed [see Fig. 12(b)] with values of

$D$ between $\sim 2$ and 3 meV nm$^2$. Similar to the Gilbert damping constant, the measured spin-stiffness constant in the optimized (Ga,Mn)As epilayers is comparable to the spin stiffness in conventional transition-metal ferromagnets (Collins *et al.*, 1969). The values of the spin stiffness of the order meV nm$^2$ are consistent with calculations based on the model kinetic-exchange and tight-binding Hamiltonians, or the *ab initio* electronic structure of (Ga,Mn)As (König, Jungwirth, and MacDonald, 2001; Brey and Gómez-Santos, 2003; Bouzerar, 2007; Werpachowska and Dietl, 2010).

To conclude Sec. II, the micromagnetic parameters of optimized (Ga,Mn)As epilayers are characteristic of common band ferromagnets and the semiconducting and magnetic properties summarized in Figs. 11 and 12 are consistent with the model Hamiltonian or *ab initio* theories of the electronic structure of (Ga,Mn)As. The materials research reviewed in Sec. II establishes the overall view of (Ga,Mn)As as a well-behaved and understood degenerate semiconductor and band ferromagnet. Combined with the tunability of its electronic and magnetic properties, strong exchange and spin-orbit interactions in the carrier bands, special symmetries of the host zinc-blende lattice, and the compatibility with established III-V semiconductor microfabrication techniques, this makes (Ga,Mn)As an ideal model system for spintronics research.

# III. PHENOMENA AND DEVICE CONCEPTS FOR SPINTRONICS

## A. Nonrelativistic versus relativistic based spintronics concepts

Most of the spintronic devices discussed in Sec. III can be associated with one of two basic physical principles. The first one stems from Mott's two-spin-channel picture of transport in ferromagnets with exchange-split bands (Mott, 1936) and we will label it a Mott spintronics principle. Phenomena which follow from the Mott picture can be typically understood using the nonrelativistic band structure with momentum-independent spin quantization axis. The second paradigm is due to the quantum-relativistic spin-orbit coupling (Strange, 1998) and we will label it a Dirac principle. Spintronics effects based on the Dirac principle stem from a relativistic band structure comprising states with momentum dependent spin expectation values. Mott devices require that spins are transported between at least two noncollinear parts of a nonuniform magnetic structure with the magnetization in one part serving as a reference to the other one. Dirac devices, on the other hand, can rely on a single uniform magnetic component and the reference for detecting or manipulating spins by charge carriers is provided internally by the spin-orbit coupling.

The archetype Ohmic Mott device, schematically illustrated in Fig. 13, is based on the giant magnetoresistance (GMR) of a ferromagnet–normal-metal–ferromagnet multilayer in which magnetizations in the ferromagnets are switched between parallel and antiparallel configurations (Baibich *et al.*, 1988; Binasch *et al.*, 1989). The archetype Ohmic Dirac device (see Fig. 13), which is discussed in Sec. III.B.2, is based on the relativistic AMR of a uniform magnetic conductor in which magnetization is rotated with respect to the current direction or crystal axes (Thomson, 1857; McGuire and Potter, 1975). In the early 1990s the AMR and subsequently the GMR sensors
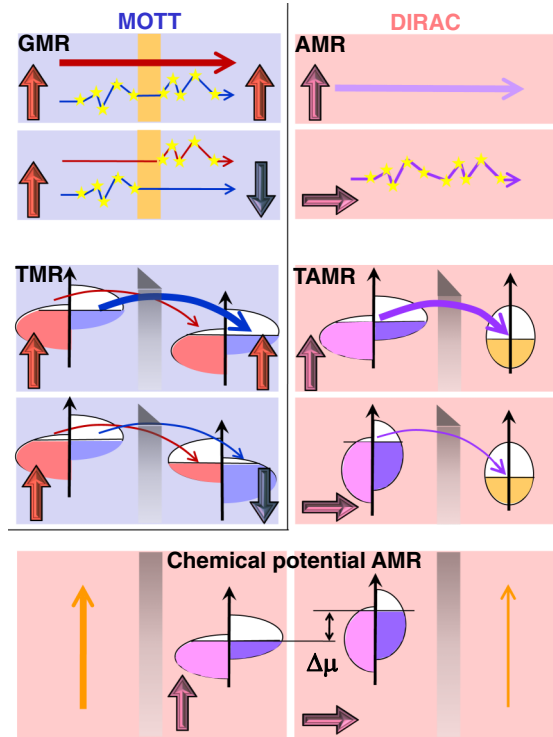
FIG. 13 (color online). Schematic comparison of Ohmic Mott (GMR) and Dirac (AMR) devices and tunneling Mott (TMR) and Dirac (TAMR) devices. At the bottom a Dirac device is shown based on the chemical potential anisotropy which has no immediate counterpart in Mott spintronics. The short thick arrows show the magnetization direction, and the long thin (thick) lines with arrows depict low (high) electrical current. The broken current lines illustrate stronger scattering. Non-relativistic (relativistic) densities of states are schematically illustrated in the TMR (TAMR, chemical potential AMR) panels.

were introduced in hard disk drive read-heads launching the field of applied spintronics (Chappert, Fert, and Dau, 2007). In these Ohmic devices, the exchange-split and, in the case of the AMR, spin-orbit coupled bands enter the physics of spin transport in a complex way via electron scattering which is often difficult to control and accurately model.

A more direct connection between spin-dependent transport and band structure is realized in tunneling devices. Here the TMR stack with two ferromagnetic electrodes (Julliere, 1975; Miyazaki and Tezuka, 1995; Moodera *et al.*, 1995) operates on the Mott principle and the TAMR stack with one magnetic electrode (Brey, Fernández-Rossier, and Tejedor, 2004; Gould *et al.*, 2004; Giraud *et al.*, 2005; Ciorga *et al.*, 2007; Gao *et al.*, 2007; Moser *et al.*, 2007; Sankowski *et al.*, 2007; Park *et al.*, 2008, 2011), discussed in Sec. III.B.3, is the corresponding Dirac spintronics device (see Fig. 13). The more direct connection between transport and electronic structure in tunneling devices implies that tunneling spintronics effects can be significantly larger than their Ohmic counterparts. The large TMR signals are used, e.g., to represent logical 0 and 1 in MRAMs (Chappert, Fert, and Dau, 2007).

CB-AMR devices discussed in Sec. III.B.4 represent an ultimate simplification in the relation between the

magnetotransport and the relativistic exchange-split band structure. Transport is governed here by a single electronic structure parameter which is the magnetization-direction dependent chemical potential, resulting in a large magneto-resistance response of the device (Wunderlich *et al.*, 2006). A CB-AMR device with the spin-orbit coupled magnet forming a gate electrode of the SET (Ciccarelli *et al.*, 2012) illustrates the fact that the Dirac spintronics principle not only works without a spin current connecting two separate magnetic electrodes but also with the spin-orbit-coupled magnetic component completely removed from the transport channel (see Fig. 13). Such a spintronic device operating without spin current cannot be realized within the more commonly considered Mott spintronics principle which may explain why it falls beyond the Wikipedia's definition of spintronics as "a portmanteau meaning spin transport electronics" (http://en .wikipedia.org/wiki/Spintronics).

The Mott GMR and TMR effects have their spin-caloritronic counterparts in the giant magnetothermopower (GMT) (Sakurai *et al.*, 1991) and TMT (Liebing *et al.*, 2011; Walter *et al.*, 2011). A similar correspondence is between the Dirac electrical transport AMR and TAMR effects and the spin-caloritronic AMT (Pu *et al.*, 2006; Wisniewski, 2007; Tang *et al.*, 2011; Anwar, Lacoste, and Aarts, 2012; Mitdank *et al.*, 2012) and TAMT (Naydenova *et al.*, 2011), discussed in Sec. III.D.3.

The distinction between Mott and Dirac spintronics can be analogously applied to the inverse magnetotransport effects (spin torques), discussed in Secs. III.B.6 and III.B.7. The STT (Berger, 1996; Slonczewski, 1996; Zhang and Li, 2004; Ralph and Stiles, 2008) applied to switch the magnetization of a free layer by a vertical current driven through the TMR stack is a Mott spin-torque effect. The in-plane current-induced SOT in a uniform magnet with a broken space-inversion symmetry (Bernevig and Vafek, 2005; Manchon and Zhang, 2008; Chernyshov *et al.*, 2009; Miron *et al.*, 2010) is the Dirac spin-torque counterpart. Similarly the optical STT and SOT (Fernández-Rossier *et al.*, 2003; Núñez *et al.*, 2004; Nemec *et al.*, 2012; Tesarova *et al.*, 2013) reviewed in Sec. III.C can be viewed as Mott and Dirac phenomena arising from the interaction of spin with light.

Observations of the Ohmic AMR in an antiferromagnetic metal FeRh (Marti *et al.*, 2014) and antiferromagnetic semiconductor $Sr_2IrO_4$ (Marti *et al.*, 2013), and of the TAMR in tunnel junctions with a magnetic electrode made of a metal antiferromagnet IrMn (Park *et al.*, 2011; Wang *et al.*, 2012), illustrate the fact that the Dirac approach to spintronics can be equally applicable to spin-orbit coupled ferromagnets and antiferromagnets. The anisotropic magnetoresistance phenomena make in principle no difference between the parallel-aligned moments in ferromagnets and antiparallel-aligned moments in antiferromagnets because they are an even function of the microscopic magnetic moments. In nonmagnetic conductors the SHE is an example of a spintronic phenomenon converting a normal electrical current into a spin current or vice versa (Kato *et al.*, 2004; Wunderlich *et al.*, 2005; Valenzuela and Tinkham, 2006; Jungwirth, Wunderlich, and Olejník, 2012). It has a similar microscopic physics origin to the AHE (Hall, 1881; Nagaosa *et al.*, 2010) in uniform spin-orbit coupled ferromagnets and the SHE can be therefore

regarded as an example of the Dirac spintronic phenomenon in nonmagnetic systems. The relevance of the research in (Ga,Mn)As to these Dirac spintronic phenomena observed in antiferromagnetic and nonmagnetic conductors will also be discussed in the following sections.

## B. Interaction of spin with electrical current

### 1. Anomalous and spin Hall effects

Advanced computational techniques and experiments in new unconventional ferromagnets have recently led to significant progress in coping with the subtle nature of the magnetoresistance effects based on relativistic spin-orbit coupling. There are two distinct relativistic MR coefficients in uniformly magnetized Ohmic devices, the AHE (Hall, 1881) and the AMR (Thomson, 1857). The AHE is the antisymmetric transverse MR coefficient obeying $\rho_{xy}(\mathbf{M}) = -\rho_{xy}(-\mathbf{M})$, where the magnetization vector $\mathbf{M}$ is pointing perpendicular to the plane of the Hall bar sample. The AMR, discussed in Sec. III.B.2, is the symmetric MR coefficient with the longitudinal and transverse resistivities obeying $\rho_{xx}(\mathbf{M}) = \rho_{xx}(-\mathbf{M})$ and $\rho_{xy}(\mathbf{M}) = \rho_{xy}(-\mathbf{M})$, where $\mathbf{M}$ has an arbitrary orientation. Note that in this review we use the term transverse AMR rather than the alternative term planar Hall effect (Tang *et al.*, 2003) to clearly distinguish this symmetric off-diagonal magnetoresistance coefficient which is even in $\mathbf{M}$ from the above antisymmetric off-diagonal Hall coefficient which is odd in $\mathbf{M}$.

(Ga,Mn)As has become one of the favorable test-bed systems for the investigation of the AHE. Here the unique position of (Ga,Mn)As ferromagnets stems from their tunability and the relatively simple, yet strongly spin-orbit coupled and exchange-split carrier bands. The principles of the microscopic description of the AHE in the metallic (Ga,Mn)As materials, based on the scattering-independent intrinsic mechanism (Luttinger, 1958; Jungwirth, Niu, and MacDonald, 2002; Onoda and Nagaosa, 2002), have been successfully applied to explain the effect in other itinerant ferromagnets (Fang *et al.*, 2003; Haldane, 2004; Lee *et al.*, 2004; Yao *et al.*, 2004; Dugaev *et al.*, 2005; Kötzler and Gil, 2005; Sinitsyn *et al.*, 2005), including conventional transition metals such as iron and cobalt, a pattern that has since then been repeated for other relativistic magnetotransport effects. The advances in the understanding of the AHE are discussed in several reviews (Chien and Westgate, 1980; Dietl *et al.*, 2003; Sinova, Jungwirth, and Černe, 2004; Jungwirth, Sinova *et al.*, 2006; Nagaosa *et al.*, 2010). Here we recall the link between the AHE and SHE.

Since the 1881 discovery of the AHE by Hall in Ni and Co, the phenomenon has been extensively employed in polarimetry measurements of electron spins in ferromagnets. One line of physical descriptions, illustrated in Fig. 14, associates the AHE with the same physical mechanism as the electron spin-dependent scattering from heavy nuclei which is used in polarimetry of high-energy electron beams in accelerators. This relativistic spin-dependent skew-scattering mechanism is referred to as Mott scattering (Mott, 1929). [To avoid confusion we point out that Mott scattering (Mott, 1929) is unrelated to the other work of Mott on the nonrelativistic two-channel description of transport in ferromagnets (Mott,
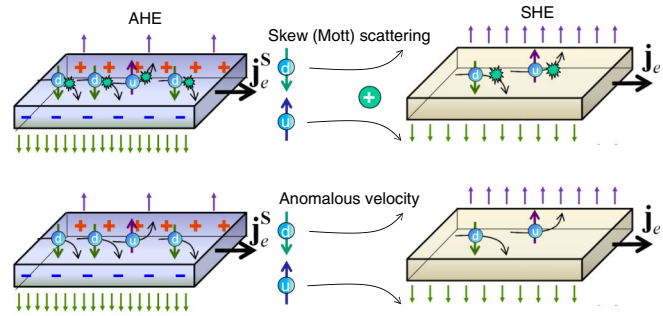


FIG. 14 (color online). Schematic illustrations of the skew (Mott) scattering AHE and SHE (top panels) and the intrinsic AHE and SHE due to the anomalous transverse component of the spin-dependent velocity originating from the spin-orbit coupled band structure in a clean crystal (bottom panels). In the AHE, an electrical current driven through a ferromagnetic conductor $j_e^s$ is spin polarized and the spin-dependent transverse deflection of electrons produces a transverse voltage. In the SHE, an unpolarized electrical current $j_e$ is driven through a normal conductor and the spin-dependent transverse deflection of electrons produces a transverse spin current. Opposite spins accumulate at opposite edges but unlike the AHE the transverse voltage remains zero.

1936) mentioned earlier; the AHE and SHE physics discussed here is relativistic in nature and falls within the family of Dirac spintronics phenomena, in the terminology used in the previous section.] The applicability of the Mott skew-scattering mechanism to electrons scattering from heavy nuclei in the vacuum environment of accelerators as well as to electrons scattering off impurities in the solid-state environment of ferromagnets implies the presence of the same mechanism in nonmagnetic conductors. This was recognized by Dyakonov and Perel (1971) in their theoretical prediction of the skew-scattering SHE.

A complementary line of research, also illustrated in Fig. 14 and prompted by AHE experiments in the highly doped metallic (Ga,Mn)As epilayers (Jungwirth, Niu, and MacDonald, 2002; Jungwirth *et al.*, 2003; Chun *et al.*, 2007; Glunk *et al.*, 2009), ascribes the AHE to a scattering-independent based mechanism in which the anomalous transverse component of the spin-dependent velocity stems directly from the spin-orbit coupled band structure in a clean crystal. In analogy with the skew-scattering AHE and SHE, a link was proposed between the scattering-independent mechanism of the AHE and a corresponding intrinsic SHE (Murakami, Nagaosa, and Zhang, 2003; Sinova, Culcer *et al.*, 2004), followed by experimental discoveries of the SHE (Kato *et al.*, 2004; Wunderlich *et al.*, 2005). We return to the physical description of these phenomena in Sec. III.B.7 where the link is extended from the AHE and SHE to the SOT.

### 2. Anisotropic magnetoresistance

Phenomenologically, the AMR has "noncrystalline" and "crystalline" components (Döring, 1938; McGuire and Potter, 1975). The former corresponds to the dependence of the resistance of the ferromagnet on the angle between magnetization and the direction of the electrical current while the latter depends on the angle between magnetization and crystal axes.

The noncrystalline AMR is the only component contributing to the AMR in polycrystalline samples in which the crystal axes directions average out. It is the component identified in Kelvin's seminal AMR measurements in Ni and Fe (Thomson, 1857). The crystalline AMR components can be isolated in single-crystal materials patterned into a Corbino-disk microdevice geometry for which the averaging over the radial current lines eliminates all effects originating from a specific direction of the current. This was demonstrated in experiments in (Ga,Mn)As (Rushforth *et al.*, 2007). The measurements took advantage of the near perfect single-crystal epilayers of (Ga,Mn)As and, simultaneously, of the low carrier density and mobility (compared with single-crystal metals) resulting in large source-drain resistances compared with the contact resistances even in the short current-line Corbino geometry. Moreover, the strong spin-orbit coupling in the (Ga,Mn)As electronic structure yields sizable and tunable crystalline AMR components which in the lower conductive (Ga,Mn) As materials can even dominate over the noncrystalline AMR component (Rushforth *et al.*, 2007). In contrast, crystalline AMR components in common transition-metal ferromagnets have been extracted indirectly from fitting the total AMR angular dependences (van Gorkom *et al.*, 2001).

Apart from the distinct phenomenologies there is also a qualitative difference between the microscopic origins of the noncrystalline and crystalline AMR components. Since the former component depends only on the angle between magnetization and current, the effects of the rotating magnetization on the equilibrium electronic structure of the ferromagnet do not contribute to the noncrystalline AMR. Instead, in the leading order, the noncrystalline AMR reflects the difference between transport scattering matrix elements of electrons with momentum parallel to the current for the current parallel or perpendicular to **M**.

Unlike the noncrystalline AMR, the crystalline AMR originates from the changes in the equilibrium relativistic electronic structure induced by the rotating magnetization with respect to crystal axes. The picture applies not only to the Ohmic crystalline AMR but also to the TAMR and CB-AMR discovered in (Ga,Mn)As (Gould *et al.*, 2004; Wunderlich *et al.*, 2006). In the CB-AMR case, the anisotropy of the electronic structure with respect to the magnetization angle, or more specifically the anisotropy of the DOS and the corresponding position of the chemical potential, provides a direct quantitative description of the measured transport effect (Wunderlich *et al.*, 2006; Ciccarelli *et al.*, 2012). In the case of the TAMR or the crystalline Ohmic AMR, the quantitative relativistic transport theory requires one to combine the calculated DOS anisotropy with the tunneling or scattering matrix elements, respectively (Jungwirth *et al.*, 2003; Brey, Tejedor, and Fernández-Rossier, 2004; Giddings *et al.*, 2005; Elsen *et al.*, 2007). Because of the anisotropy of the electronic structure with respect to the magnetization angle the matrix elements may also change when magnetization is rotated.

A physically appealing picture has been used to explain the positive sign of the noncrystalline AMR (defined as the relative difference between resistances for current parallel and perpendicular to **M**) observed in most transition-metal ferromagnets (Smit, 1951; McGuire and Potter, 1975). The interpretation is based on the model of the spin-up and

spin-down two-channel conductance corrected for perturbative spin-orbit coupling effects. In the model most of the current is carried by the light-mass *s* electrons which experience no spin-orbit coupling and a negligible exchange splitting but can scatter to the heavy-mass *d* states. AMR is then explained by considering the spin-orbit potential which mixes the exchange-split spin-up and spin-down *d* states in a way which leads to an anisotropic scattering rate of the current carrying *s* states (Smit, 1951; McGuire and Potter, 1975). Controversial interpretations, however, have appeared in the literature based on this model (Smit, 1951; Potter, 1974) and no clear connection has been established between the intuitive picture of the AMR the model provides and the numerical *ab initio* transport theories (Banhart and Ebert, 1995; Ebert, Vernes, and Banhart, 1999; Khmelevskyi *et al.*, 2003).

Among the remarkable AMR features of (Ga,Mn)As are the opposite sign of the noncrystalline component, as compared to most metal ferromagnets, and the sizable crystalline terms reflecting the rich magnetocrystalline anisotropies of (Ga,Mn) As (Baxter *et al.*, 2002; Jungwirth *et al.*, 2003; Tang *et al.*, 2003; Matsukura *et al.*, 2004; Goennenwein *et al.*, 2005; Wang, Edmonds *et al.*, 2005; Limmer *et al.*, 2006; Rushforth *et al.*, 2007). In Fig. 15 we show an example of AMR data from a systematic experimental and phenomenological study of the
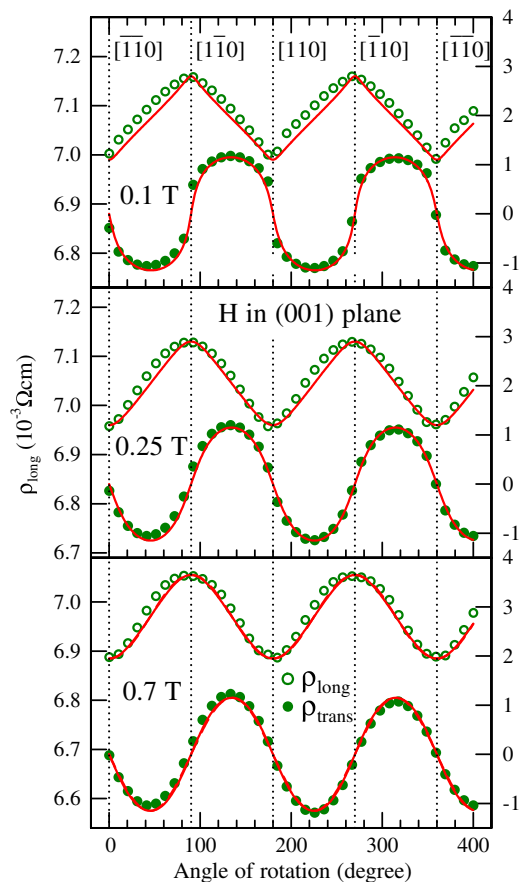


FIG. 15 (color online). Measured longitudinal and transverse in-plane AMR curves at external fields smaller than the saturation field (0.1 and 0.25 T) and larger than the saturation field (0.7 T). The solid lines represent fits to the experimental data. From Limmer *et al.*, 2006.

AMR coefficients in (Ga,Mn)As films grown on (001)- and (113)*A*-oriented GaAs substrates at nonsaturating and saturating in-plane and out-of-plane magnetic fields (Limmer *et al.*, 2006). In the following we describe the AMR phenomenology in (Ga,Mn)As in more detail and explain the basic microscopic physics origin of the noncrystalline AMR in (Ga,Mn)As. For simplicity we focus on the AMR in saturating magnetic fields, for **M** oriented in the plane of the device, and for (Ga,Mn)As films grown on the (001)-GaAs substrate.

The phenomenological decomposition of the AMR of (Ga,Mn)As into various terms allowed by symmetry is obtained by extending the standard phenomenology (Döring, 1938) to systems with the cubic and in-plane uniaxial anisotropy. The corresponding AMR is then phenomenologically described as (Rushforth *et al.*, 2007; De Ranieri *et al.*, 2008)

$$\frac{\Delta\rho_{xx}}{\rho_{\mathrm{av}}} = C_I \cos 2\phi + C_U \cos 2\psi + C_C \cos 4\psi$$
$$+ C_{I,C} \cos(4\psi - 2\phi), \tag{1}$$

where $\Delta\rho_{xx} = \rho_{xx} - \rho_{\mathrm{av}}$, $\rho_{\mathrm{av}}$ is the $\rho_{xx}$ averaged over 360° in the plane of the film, $\phi$ is the angle between the magnetization unit vector $\hat{\mathbf{M}}$ and the current **I**, and $\psi$ is the angle between $\hat{\mathbf{M}}$ and the [110] crystal direction. The four contributions are the noncrystalline term, the lowest order uniaxial and cubic crystalline terms, and a crossed noncrystalline or crystalline term. The purely crystalline terms are excluded by symmetry for the transverse AMR and one obtains (Rushforth *et al.*, 2007; De Ranieri *et al.*, 2008)

$$\frac{\Delta\rho_{xy}}{\rho_{\mathrm{av}}} = C_I \sin 2\phi - C_{I,C} \sin(4\psi - 2\phi). \tag{2}$$

Microscopic numerical simulations (Jungwirth *et al.*, 2002, 2003; Rushforth *et al.*, 2007; Vyborny *et al.*, 2009) consistently describe the sign and magnitudes of the noncrystalline AMR in (Ga,Mn)As materials with metallic conductivities and capture the presence of the more subtle crystalline terms (Jungwirth *et al.*, 2002; Matsukura *et al.*, 2004). Based on the numerical simulations the origin and sign of the noncrystalline AMR in (Ga,Mn)As was qualitatively explained using a simplified model in which carriers, represented by the heavy-hole Fermi surface in the spherical spin-texture approximation (see Fig. 16), scatter off random Mn impurity potential approximated by $\propto (r\mathbb{1} + \hat{\mathbf{M}}\cdot\mathbf{s})$. Here $\mathbf{s} = \mathbf{j}/3$ is the carrier spin operator in the spherical approximation with $\mathbf{j}$ representing the total angular momentum operator of heavy holes ($j = 3/2$), and $r$ effectively models the ratio of nonmagnetic (Coulomb and central cell) and magnetic (*p-d* kinetic exchange) parts of the Mn-impurity potential (Rushforth *et al.*, 2007; Trushin *et al.*, 2009; Vyborny *et al.*, 2009).

The qualitative AMR considerations focus on scattering matrix elements of state with momentum along the current **I** and, in particular, on the strongest contribution to the transport lifetime which comes from backscattering (see Fig. 16) (Rushforth *et al.*, 2007; Trushin *et al.*, 2009; Vyborny *et al.*, 2009). When neglecting the nonmagnetic part of the impurity potential ($r = 0$), nonzero backscattering matrix elements
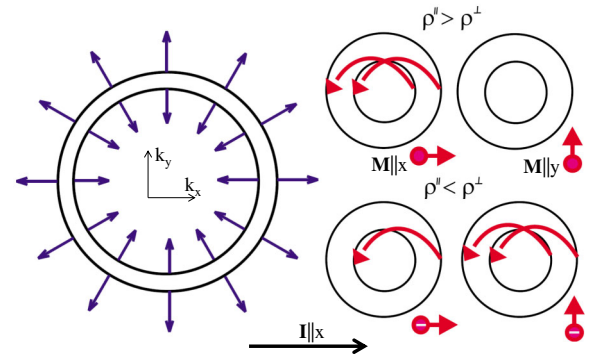


FIG. 16 (color online). Left panel: Cross section (parallel to the $k_x$, $k_y$ plane) of the 3D radial spin texture belonging to the two heavy-hole bands of (Ga,Mn)As in a spherical approximation. Right top panel: Nonzero backscattering elements when neglecting the nonmagnetic part of the Mn-impurity potential. The corresponding AMR has a positive sign. The purely magnetic Mn impurity is illustrated by a dot with an arrow. Right bottom panel: Nonzero backscattering elements for the same strengths of the nonmagnetic and magnetic parts of the Mn-impurity potential. The corresponding AMR has a negative sign. The combined ionized acceptor and magnetic nature of the Mn impurity is illustrated by a dot with a negative sign and an arrow. (Electrical current **I**∥*x*.) From Trushin *et al.*, 2009.

occur only for **M**∥**I** and in the notation of Fig. 16 they correspond to the elements $\langle \to |j_x| \to \rangle$ and $\langle \leftarrow |j_x| \leftarrow \rangle$. For **M**⊥**I**, all backscattering elements $\langle \to |j_y| \to \rangle = 0$, $\langle \leftarrow |j_y| \to \rangle = 0$, etc., i.e., the backscattering is completely suppressed. The picture changes when the nonmagnetic part of the Mn-impurity potential is included, as illustrated in Fig. 16 for $r = 1/2$. For **M**∥**I**, the coherent scattering of the nonmagnetic and magnetic parts interferes constructively or destructively leaving only one of the backscattering elements nonzero (see Fig. 16). For **M**⊥**I**, the nonmagnetic and magnetic parts do not interfere and now the nonmagnetic part of the scattering potential results in two nonzero backscattering elements (see Fig. 16). As a result the resistivity $\rho_{xx}^{\parallel}$ for **M**∥**I** is larger than $\rho_{xx}^{\perp}$ for **M**⊥**I** when $r = 0$ and $\rho_{xx}^{\parallel}$ is smaller than $\rho_{xx}^{\perp}$ when $r = 1/2$. The presence of the nonmagnetic part of the impurity potential can, therefore, flip the sign of the AMR from the positive which is seen in common transition-metal ferromagnets to the negative which is typical of (Ga,Mn)As. The negative sign is obtained in the above simplified model for $r > 1/\sqrt{20}$ which is safely satisfied in (Ga,Mn)As (Rushforth *et al.*, 2007; Trushin *et al.*, 2009; Vyborny *et al.*, 2009).

### 3. Tunneling anisotropic magnetoresistance

The electrical response to changes in the magnetic state is strongly enhanced in layered structures consisting of alternating ferromagnetic and nonmagnetic materials. The GMR and TMR effects which are widely exploited in metal spintronics technologies reflect the large difference between resistivities in configurations with parallel and antiparallel polarizations of ferromagnetic layers in magnetic multilayers, or trilayers like spin valves and magnetic tunnel junctions (Gregg *et al.*, 2002; Chappert, Fert, and Dau, 2007). The effect relies on transporting spin information between the layers. In

(Ga,Mn)As, functional magnetic tunnel junction devices can be built, as demonstrated by the measured large TMR effects (Tanaka and Higo, 2001; Brey, Tejedor, and Fernández-Rossier, 2004; Chiba, Matsukura, and Ohno, 2004; Chiba *et al.*, 2004; Mattana *et al.*, 2005; Saito, Yuasa, and Ando, 2005; Saffarzadeh and Shokri, 2006; Elsen *et al.*, 2007; Ohya *et al.*, 2007; Sankowski *et al.*, 2007).

Here we focus on the physics of the TAMR which was discovered in (Ga,Mn)As based tunnel devices (Brey, Tejedor, and Fernández-Rossier, 2004; Gould *et al.*, 2004; Giraud *et al.*, 2005; Rüster, Gould, Jungwirth, Sinova *et al.*, 2005; Saito, Yuasa, and Ando, 2005; Ciorga *et al.*, 2007; Elsen *et al.*, 2007; Sankowski *et al.*, 2007). TAMR, like AMR, arises from spin-orbit coupling and reflects the dependence of the tunneling density of states of the ferromagnetic layer on the orientation of the magnetization. The effect does not rely on spin coherence in the tunneling process and requires only one ferromagnetic contact.

In Fig. 17 we show the TAMR signal which was measured in a $(Ga,Mn)As/AlO_x/Au$ vertical tunnel junction (Gould *et al.*, 2004; Rüster, Gould, Jungwirth, Girgis *et al.*, 2005). For the in-plane magnetic field applied at an angle 50° off the [100] axis the magnetoresistance is reminiscent of the conventional spin-valve signal with hysteretic high-resistance states at low fields and low-resistance states at saturation. Unlike the TMR or GMR, however, the sign changes when the field is applied along the [100] axis. Complementary superconducting quantum interference device (SQUID) magnetization measurements confirmed that for the sample measured in Fig. 17 the high-resistance state corresponds to magnetization in the (Ga,Mn)As contact aligned along the [100] direction and the low-resistance state along the [010] direction, and that this TAMR effect reflects the underlying magnetocrystalline
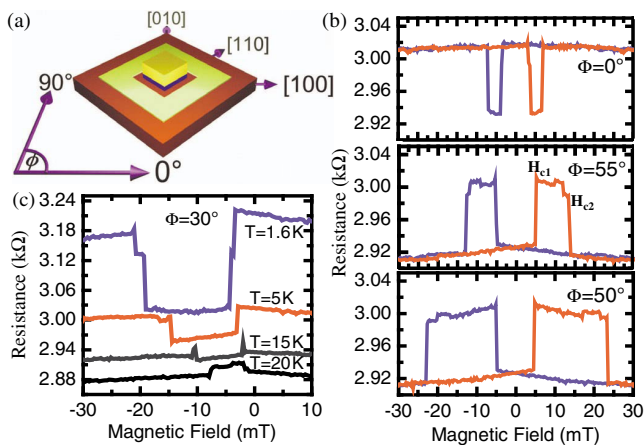


FIG. 17 (color online). (a) Device schematic showing the contact geometry and the crystallographic directions. (b) Hysteretic magnetoresistance curves acquired at 4.2 K with 1 mV bias by sweeping the magnetic field along the 0°, 50°, and 55° directions. Spin-valve-like features of varying widths and signs are clearly visible, delimited by two switching events labeled $H_{c1}$ and $H_{c2}$. The magnetoresistance is independent of the bias direction or amplitudes up to 1 meV. (c) TAMR along 30° for temperatures from 1.6 to 20 K, showing a change of sign of the signal. The curves are vertically offset for clarity. From Gould *et al.*, 2004.

anisotropy between the $\mathbf{M} \| [100]$ and $\mathbf{M} \| [010]$ magnetic states of the specific (Ga,Mn)As material used in the study. Since the field is rotated in the plane perpendicular to the current, the Lorentz force effects on the tunnel transport can be ruled out. Microscopic calculations consistently showed that the spin-orbit coupling induced density-of-states anisotropies with respect to the magnetization orientation can produce TAMR effects in (Ga,Mn)As of the order ~1% to ~10% (Gould *et al.*, 2004; Rüster, Gould, Jungwirth, Girgis *et al.*, 2005).

All-semiconductor TAMR devices with a single ferromagnetic electrode were realized in $p$-(Ga,Mn)As/$n$-GaAs Zener-Esaki diodes (Giraud *et al.*, 2005; Ciorga *et al.*, 2007). For magnetization rotations in the (Ga,Mn)As plane (Ciorga *et al.*, 2007) comparable TAMR ratios were detected as in the $(Ga,Mn)As/AlO_x/Au$ tunnel junction. About an order of magnitude larger TAMR (40%) was observed when magnetization was rotated out of the (Ga,Mn)As plane toward the current direction (Giraud *et al.*, 2005).

Several detailed numerical studies have been performed based on microscopic tight-binding or kinetic-exchange models of the (Ga,Mn)As electronic structure and the Landauer-Büttiker quantum transport theory (Brey, Tejedor, and Fernández-Rossier, 2004; Giddings *et al.*, 2005; Elsen *et al.*, 2007; Sankowski *et al.*, 2007). Besides the Zener-Esaki diode geometry (Sankowski *et al.*, 2007) the simulations consider magnetic tunnel junctions with two ferromagnetic (Ga,Mn)As contacts and focus on comparison between the TMR and TAMR signals in structures with different barrier materials and (Ga,Mn)As parameters (Brey, Tejedor, and Fernández-Rossier, 2004; Elsen *et al.*, 2007; Sankowski *et al.*, 2007). Figure 18 shows the theoretical dependence of the TMR ratio for parallel and antiparallel configurations of the two (Ga,Mn)As contacts and $\mathbf{M}$ along the [100] direction and the TAMR ratio for parallel magnetizations in the (Ga,Mn)As films and $\mathbf{M}$ along the [100] direction and the [001] direction (current direction) in a tunneling device with an InGaAs barrier (Elsen *et al.*, 2007). The corresponding experimental measurements are shown in Fig. 19. There is an overall agreement between the theory and experiment, seen also in tunnel junctions with other barrier materials, showing that the TMR is typically ten times larger than the TAMR. Both the theory and experiment also find that the TMR signal is always positive, i.e., the magnetoresistance increases as the field is swept from saturation to the switching field. The TAMR can have both signs depending on the field angle but also depending on the parameters of the (Ga,Mn)As film such as the hole concentration and polarization, on the barrier characteristics, or on the temperature (Gould *et al.*, 2004; Elsen *et al.*, 2007).

At very low temperatures and bias voltages large TAMR signals were observed (Rüster, Gould, Jungwirth, Girgis *et al.*, 2005) in a $(Ga,Mn)As/GaAs/(Ga,Mn)As$ tunnel junction which are not described by the one-body theories of anisotropic tunneling transmission coefficients. The observation was interpreted as a consequence of electron-electron correlation effects near the metal-insulator transition (Pappert *et al.*, 2006). Large anisotropic magnetoresistance effects were also measured in lateral nanoconstriction devices fabricated in ultrathin (Ga,Mn)As materials (Rüster *et al.*,
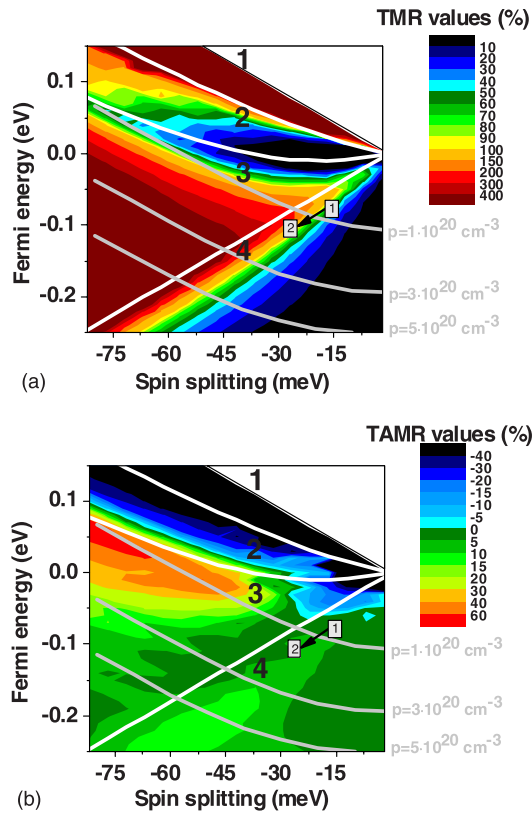
FIG. 18 (color online).    Calculated (a) TMR values and (b) TAMR values represented as a function of the Fermi and spin splitting energy for a 6 nm (In,Ga)As barrier with a band offset of 450 meV. White lines represent the four bands at the center of the Brillouin zone. Gray lines indicate the Fermi energy for different hole concentrations. From Elsen *et al.*, 2007.



FIG. 19 (color online).    (a) TMR measurements as a function of the magnetic field at 1 mV and 3 K for a 128 $\mu m^2$ junction. (b) TMR measurements as a function of resistance area (RA) product at 3 K for four (un)annealed junctions. (c) TMR at 1 mV as a function of the temperature before and after annealing. (d) TAMR measurements as a function of the magnetic field at 1 mV and 3 K. From Elsen *et al.*, 2007.

2003; Giddings *et al.*, 2005; Schlapps *et al.*, 2006). The comparison of the anisotropic magnetoresistance signals in the unstructured part of the device and in the nanoconstriction showed a significant enhancement of the signal in the constriction (Giddings *et al.*, 2005). Subsequent studies of these nanoconstrictions with an additional side gate patterned along the constriction, discussed in detail in Sec. III.B.4 (Wunderlich *et al.*, 2006; Wunderlich, Jungwirth, Irvine *et al.*, 2007; Wunderlich, Jungwirth, Novák *et al.*, 2007; Schlapps *et al.*, 2009), indicated that single-electron charging effects were responsible for the observed large anisotropic magnetoresistance signals.

Before moving on to the (Ga,Mn)As-based field-effect transistors we conclude this section with a remark on the impact of the TAMR discovery in (Ga,Mn)As on spintronics research in other magnetic materials. *Ab initio* relativistic calculations of the anisotropies in the density of states predicted sizable TAMR effects in transition-metal ferromagnets (Shick *et al.*, 2006). Landauer-Büttiker transport theory calculations for a Fe/vacuum/Cu structure pointed out that apart from the density-of-states anisotropies in the ferromagnetic metal itself, the TAMR in the tunnel devices can arise from spin-orbit coupling induced anisotropies of resonant surface or interface states (Chantis *et al.*, 2007). Experimentally, se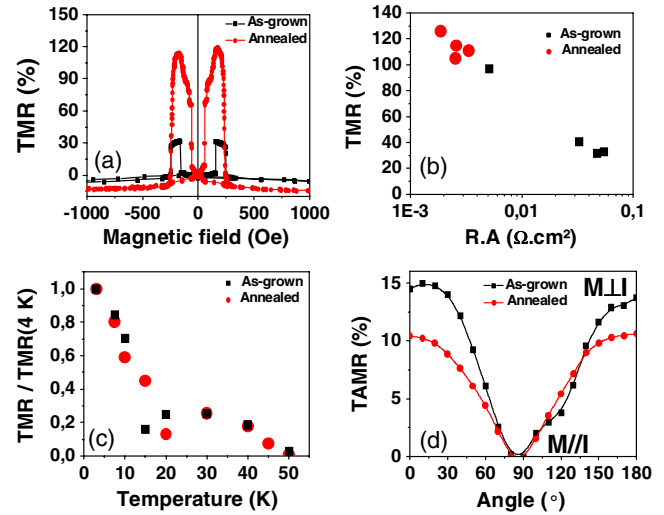veral reports of metal TAMR devices have already appeared in the literature including Fe, Ni, and Co lateral break junctions (Bolotin, Kuemmeth, and Ralph, 2006; Viret *et al.*, 2006) which showed comparable (∼10%) low-temperature TMR and TAMR signals, Fe/GaAs/Au and Fe/*n*-GaAs vertical tunnel junctions (Moser *et al.*, 2007; Uemura *et al.*, 2009) with a ∼1% TAMR at low temperatures reflecting the spin-orbit fields and symmetries at the metal/semiconductor interface, a $Co/Al_2O_3/NiFe$ magnetic tunnel junction with a 15% TAMR at room temperature (Grigorenko, Novoselov, and Mapps, 2006), reports of strongly bias dependent TAMRs in devices with CoFe (Gao *et al.*, 2007) and CoPt electrodes (Park *et al.*, 2008), and larger than 100% TAMRs in tunneling devices with an antiferromagnetic IrMn electrode (Park *et al.*, 2011; Wang *et al.*, 2012).

### 4. Transistor and chemical potential anisotropy devices

As mentioned in the Introduction, (In,Mn)As, (Ga,Mn)As, and (Ga,Mn)(As,P) based field-effect transistors were fabricated to demonstrate the electric-field control of ferromagnetism. It was shown that changes in the carrier density and distribution in thin ferromagnetic semiconductor films due to an applied gate voltage can change the Curie temperature, as illustrated in Fig. 20, and thus reversibly induce the ferromagnetic-paramagnetic transition (Ohno *et al.*, 2000; Chiba, Matsukura, and Ohno, 2006; Stolichnov *et al.*, 2008; Riester *et al.*, 2009; Sawicki *et al.*, 2010). Another remarkable effect observed in these transistors is the electric-field control of the magnetization orientation (Chiba *et al.*, 2003, 2008, 2013; Chiba, Matsukura, and Ohno, 2006; Wunderlich, Jungwirth, Irvine *et al.*, 2007; Olejník *et al.*, 2008; Stolichnov *et al.*, 2008; Owen *et al.*, 2009; Niazi *et al.*, 2013). This functionality is based on the dependence of the magnetic anisotropies on the gate voltage, again through the modified charge density profile in the ferromagnetic semiconductor thin film.

FIG. 21 (color online). (a) Electron micrograph of the central part of a (Ga,Mn)As SET device. (b) Polar plot of the source-drain resistance $R_{sd}$ at 1.6 K showing the strong anisotropy as a function of the magnetization direction. From Schlapps *et al.*, 2009.
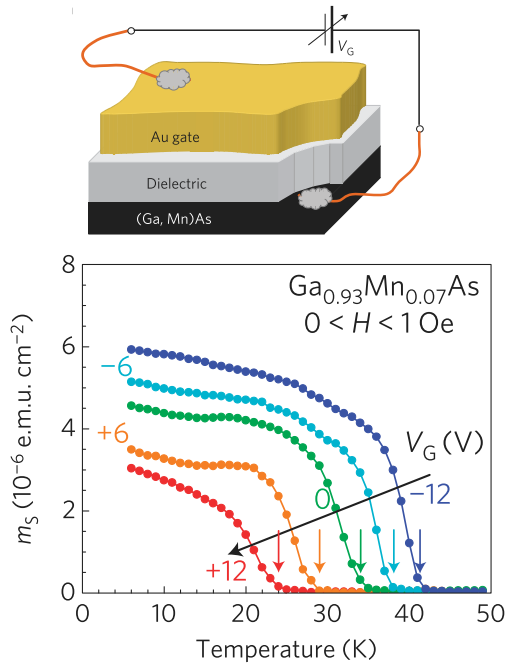


FIG. 20 (color online). Top panel: Schematics of a capacitor with an ultrathin (3.5 nm) (Ga,Mn)As layer. Bottom panel: Experimental temperature dependence of the spontaneous moment for selected values of gate voltage. Temperatures at which the moment disappears define the Curie temperature $T_c$, as marked by arrows. From Sawicki *et al.*, 2010.

For a spintronic transistor, the magnetoresistance is another key characteristic which should be controllable by the gate electric field. Large and voltage-dependent AMR effects were reported in Ohmic (Ga,Mn)(As,P) channels with an integrated polymer ferroelectric gate (Mikheev *et al.*, 2012) and CB-AMR effects were demonstrated in (Ga,Mn)As SETs (Wunderlich *et al.*, 2006; Wunderlich, Jungwirth, Irvine *et al.*, 2007; Wunderlich, Jungwirth, Novák *et al.*, 2007; Schlapps *et al.*, 2009; Ciccarelli *et al.*, 2012), as illustrated in Fig. 21.

In the conventional SET, the transfer of an electron from a source lead to a drain lead via a small, weakly coupled island is blocked due to the charging energy of $e^2/2C_\Sigma$, where $C_\Sigma$ is the total capacitance of the island (Likharev, 1999). Applying a voltage $V_G$ between the source lead and a gate electrode changes the electrostatic energy function of the charge $Q$ on the island to $Q^2/2C_\Sigma + QC_GV_G/C_\Sigma$ which has a minimum at $Q_0 = -C_GV_G$. By tuning the continuous external variable $Q_0$ to $(n + 1/2)e$, the energy associated with increasing the charge $Q$ on the island from $ne$ to $(n + 1)e$ vanishes and electrical current can flow between the leads. Changing the gate voltage then leads to CB oscillations in the source-drain current where each period corresponds to increasing or decreasing the charge state of the island by one electron. The energy can be written as a sum of the internal, electrostatic charging energy term and the term associated with, in general, different chemical potentials of the lead and of the island:

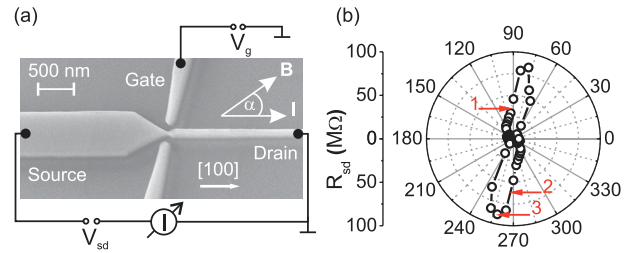$$U = \int_0^Q dQ' \Delta V_D(Q') + Q\Delta\mu/e, \qquad (3)$$

where $\Delta V_D(Q) = (Q + C_GV_G)/C_\Sigma$. The Gibbs energy $U$ is minimized at $Q_0 = -C_G(V_G + V_M)$.

The ferromagnetic SETs with (Ga,Mn)As in the transport channel of the transistor (Wunderlich *et al.*, 2006; Schlapps *et al.*, 2009) were fabricated by trench isolating a side-gated narrow (tens of nm) channel in a thin-film (Ga,Mn)As epilayer. The narrow channel technique is a simple approach to realize a SET and was used previously to produce nonmagnetic thin-film Si and GaAs-based SETs in which disorder potential fluctuations create small islands in the channel without the need for a lithographically defined island (Kastner, 1992; Tsukagoshi, Alphenaar, and Nakazato, 1998). The nonuniform carrier concentration produces differences between chemical potentials $\Delta\mu$ of the lead and of the island in the constriction. There are two mechanisms through which $\Delta\mu$ depends on the magnetic field. One is caused by the direct Zeeman coupling of the external magnetic field and leads to a CB magnetoresistance previously observed in ferromagnetic metal SETs (Ono, Shimada, and Ootuka, 1997).

The CB-AMR effect, discovered in the (Ga,Mn)As SETs, is attributed to the spin-orbit coupling induced anisotropy of the carrier chemical potential, i.e., to magnetization orientation dependent differences between chemical potentials of the lead and of the island in the constriction (Wunderlich *et al.*, 2006). For the CB-AMR effect, the magnetization orientation dependent shift of the CB oscillations is given by $V_M = [C_\Sigma/C_G\Delta\mu(\mathbf{M})]/e$. Since $|C_GV_M|$ has to be of the order of $|e|$ to cause a marked shift in the oscillation pattern, the corresponding $|\Delta\mu(\mathbf{M})|$ has to be similar to $e^2/C_\Sigma$, i.e., of the order of the island single-electron charging energy. The fact that CB-AMR occurs when the anisotropy in a band structure derived parameter is comparable to an independent scale (single-electron charging energy) makes the effect distinct and potentially much larger in magnitude as compared to the AMR and TAMR. Indeed, resistance variations by more than 3 orders of magnitude were observed in the (Ga,Mn)As SETs.

The sensitivity of the magnetoresistance to the orientation of the applied magnetic field is an indication of the anisotropic magnetoresistance origin of the effect. This is confirmed by the observation of comparably large and gate-controlled magnetoresistance in a field-sweep experiment and when the saturation magnetization is rotated with respect to the crystallographic axes. The field-sweep and rotation

measurements are shown in Figs. 22(c) and 22(d) and compared with analogous measurements of the Ohmic AMR in the unstructured part of the (Ga,Mn)As bar, plotted in Figs. 22(a) and 22(b) (Wunderlich *et al.*, 2006). In the unstructured bar, higher or lower resistance states correspond to magnetization along or perpendicular to the current direction. Similar behavior is seen in the SET part of the device at, for example, $V_G = -0.4$ V, but the anisotropic magnetoresistance is now largely increased and strongly depends on the gate voltage.

The large magnetoresistance signals can also be hysteretic which shows that CB-AMR SETs can act as a nonvolatile memory-transistor element. In nonmagnetic SETs, the CB "on" (low-resistance) and "off" (high-resistance) states can represent logical "1" and "0" and the switching between the two states can be realized by applying a gate voltage, in analogy with a standard field-effect transistor. The CB-AMR SET can be addressed also magnetically with comparable on to off resistance ratios in the electric and magnetic modes. The functionality is illustrated in Fig. 23 (Wunderlich, Jungwirth, Irvine *et al.*, 2007). The inset of Fig. 23(a) shows two CB oscillation curves corresponding to two different magnetization states $M_0$ and $M_1$. As illustrated in Fig. 23(b), $M_0$ can be achieved by performing a small loop in the magnetic field $B \rightarrow B_0 \rightarrow 0$, where $B_0$ is larger than the first switching field $B_{c1}$ and smaller than the second switching field $B_{c2}$, and $M_1$ is achieved by performing the large field loop $B \rightarrow B_1 \rightarrow 0$, where $B_1 < -B_{c2}$. The main plot of Fig. 23(a) shows that the high-resistance 0 state can be set by either the combinations $(M_1, V_{G0})$ or $(M_0, V_{G1})$ and the low-resistance 1 state by $(M_1, V_{G1})$ or $(M_0, V_{G0})$. One can therefore switch between states 0 and 1 either by changing $V_G$ in a given magnetic state



FIG. 23 (color online). (a) Two opposite transistor characteristics in a gate-voltage range $V$ ($V_{G0}$) to 1.04 V ($V_{G1}$) for two different magnetization orientations $M_0$ and $M_1$; corresponding Coulomb blockade oscillations in a larger range of $V_G = 0.6$ to 1.15 V are shown in the inset. Switching between low-resistance (1) and high-resistance (0) states can be performed electrically or magnetically. (b) Hysteretic magnetoresistance at constant gate voltage $V_{G1}$ illustrating the nonvolatile memory effect in the magnetic mode. (c) Illustration of integrated transistor (electric mode) and permanent storage (magnetic mode) functions in a single nanoscale element. (d) The transistor characteristic for $M = M_1$ is reminiscent of an *n*-type field-effect transistor and is inverted (reminiscent of a *p*-type field-effect transistor) for $M = M_0$; the inversion can also be realized in the nonvolatile magnetic mode. From Wunderlich, Jungwirth, Irvine *et al.*, 2007.
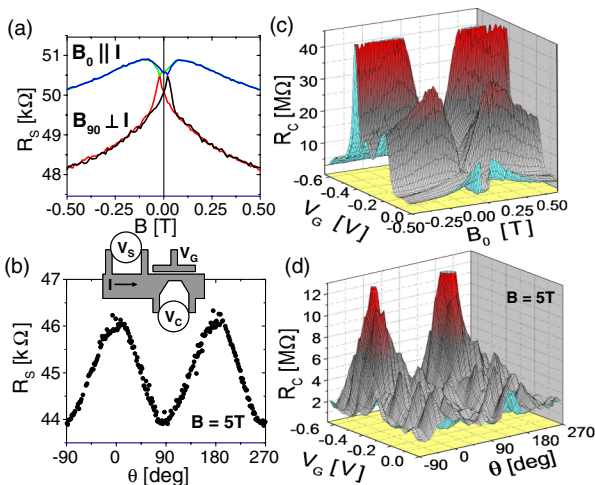


FIG. 22 (color online). (a) Resistance $R_S = V_S/I$ of the unstructured bar (see schematic diagram) vs up and down sweeps of in-plane magnetic field parallel and perpendicular to the current direction. (b) $R_S$ vs the angle between the current direction and an applied in-plane magnetic field of 5 T, at which $M \| B$. (c) Channel resistance $R_C$ vs gate voltage and down sweep of the magnetic field parallel to current. (d) $R_C$ vs gate voltage and the angle between the current direction and an applied in-plane magnetic field of 5 T. From Wunderlich *et al.*, 2006.
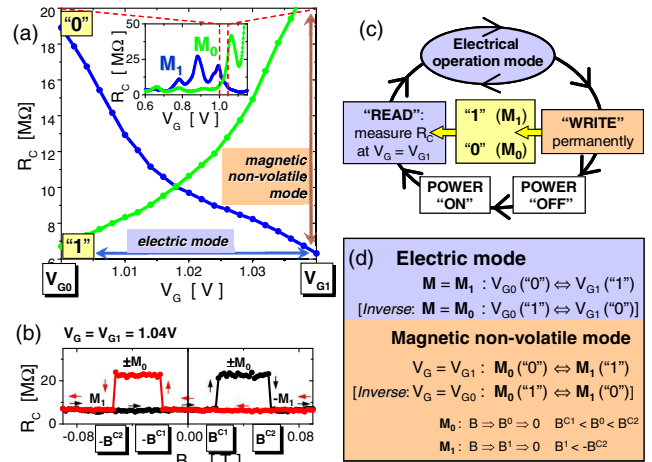
(the electric mode) or by changing the magnetic state at fixed $V_G$ (the magnetic mode). Because of the hysteresis, the magnetic mode represents a nonvolatile memory effect. Figure 23(c) illustrates one of the new functionality concepts the device suggests in which low-power electrical manipulation and permanent storage of information are realized in one physical nanoscale element. Figure 23(d) highlights the possibility to invert the transistor characteristic; for example, the system is in the low-resistance "1" state at $V_{G1}$ and in the high-resistance "0" state at $V_{G0}$ (reminiscent of an *n*-type field-effect transistor) for the magnetization $M_1$ while the characteristic is inverted (reminiscent of a *p*-type field-effect transistor) by changing magnetization to $M_0$.

Chemical potential shifts in the relativistic band structure of solids have rarely been discussed in the scientific literature. This reflects the conceptual difficulty in describing the chemical potential shifts by quantitative theories, the lack of direct measurements of the effect, and the lack of proposals in which the phenomenon could open unconventional paths in microelectronic device designs. Wunderlich *et al.* (2006), Shick *et al.* (2010), and Ciccarelli *et al.* (2012) are among the few who attempted to quantify chemical potential anisotropies with respect to the spin orientation in semiconductor and metal magnets using relativistic model Hamiltonian or full-potential density-functional band structure calculations. The theories could account for chemical potential shifts due to the distortion in the dispersion of the spin-orbit coupled bands but for principle reasons omit possible shifts of the vacuum level

with respect to band edges, in other words, possible shifts in band lineups in realistic heterostructure systems.

In experiments described above and in other related measurements, the magnetic materials have been integrated in a conventional design of a magnetoelectronic device, i.e., embedded in the transport channel, and the chemical potential shifts could have been inferred only indirectly from the measured data (Ono, Shimada, and Ootuka, 1997; Deshmukh and Ralph, 2002; Wunderlich *et al.*, 2006; van der Molen, Tombros, and van Wees, 2006; Bernand-Mantel *et al.*, 2009; Schlapps *et al.*, 2009; Tran *et al.*, 2009). One exception is the work discussed in more detail below, which has demonstrated direct measurements of chemical potential shifts in a spin-orbit coupled ferromagnet (Ciccarelli *et al.*, 2012). The corresponding spintronic device operates without spin currents, i.e., it demonstrates a functionality which goes beyond the common concepts of spintronics. The device represents an unconventional spin transistor where the charge state of the transport channel is sensitive to the spin state of its magnetic gate.

The SET from Ciccarelli *et al.* (2012) has a micron-scale Al island separated by aluminum oxide tunnel junctions from Al source and drain leads [Fig. 24(a)]. It is fabricated on top of an epitaxially grown (Ga,Mn)As layer, which is electrically insulated from the SET by an alumina dielectric, and acts as a spin back gate to the SET. By sweeping the externally applied potential to the SET gate ($V_g$), one obtains the conductance oscillations that characterize the CB as shown in Fig. 24(b). Because of the magnetic gate a shift is observed in these oscillations by an applied saturating magnetic field which rotates the magnetization in the (Ga,Mn)As gate. Figure 24(b) shows measurements for the in-plane ($\Phi = 90°$) and for the

perpendicular-to-plane ($\Phi = 0°$) directions of magnetization. Alternatively, Fig. 24(c) shows the channel conductance as a function of the magnetization angle $\Phi$ for a fixed external potential $V_g$ applied to the gate. The oscillations in $\Phi$ seen in Fig. 24(c) are of comparable amplitude as the oscillations in $V_g$ in Fig. 24(b).

Since the (Ga,Mn)As back gate is attached to a charge reservoir, any change in the internal chemical potential of the gate induced by the rotating magnetization vector causes an inward, or outward, flow of charge in the gate, as illustrated in Fig. 24(e). This change in back-gate charge offsets the Coulomb oscillations [Fig. 24(b)] and changes the conductance of the transistor channel for a fixed external potential applied to the gate [Fig. 24(c)].

In the case of the SET with the magnetic gate no capacitance scaling factors are required and the chemical potential shift may be directly read off as a shift in gate voltage. This removes a source of systematic error, present in experiments on the magneto-Coulomb effect (Ono, Shimada, and Ootuka, 1997; Deshmukh and Ralph, 2002; van der Molen, Tombros, and van Wees, 2006) or chemical potential anisotropy in SETs with the ferromagnet forming part of the transport channel (lead or island) (Wunderlich *et al.*, 2006; Bernand-Mantel *et al.*, 2009; Schlapps *et al.*, 2009; Tran *et al.*, 2009), where the gate-voltage shift must be scaled due to the presence of a capacitive divider.

In agreement with experiment, the theoretical chemical potential anisotropies in the studied (Ga,Mn)As epilayers with Mn doping of several percent are of the order of 10–100 $\mu$eV (Ciccarelli *et al.*, 2012). So far, the spin-gating technique was employed to accurately measure the anisotropic [and also isotropic Zeeman (Ciccarelli *et al.*, 2012)] chemical potential shifts in (Ga,Mn)As. However, the technique can be applied to catalog these effects in other magnetic materials by the simple step of exchanging the magnetic gate electrode.

## 5. Spin torques and spin pumping

When spin-polarized carriers are injected into a magnetic region whose moments are misaligned with the injected spin polarization of the carriers, STTs can act on the magnetic moments (Ohno and Dietl, 2008; Ralph and Stiles, 2008). The phenomena belong to an important area of spintronics research focusing on the means for manipulating magnetization by electrical currents and are the basis of the emerging technologies for scalable MRAMs (Chappert, Fert, and Dau, 2007). Apart from STTs in nonuniform magnetic structures, whose research in (Ga,Mn)As is reviewed later in Sec. III.B.6, experiments in (Ga,Mn)As devices established the presence of current-induced spin torques in uniform magnetic structures originating from the internal spin-orbit coupling. These current-induced SOT phenomena are reviewed in Sec. III.B.7, and in Secs. III.C.2 and III.C.3 we discuss the optical counterparts of the STT and SOT which were also discovered in (Ga,Mn)As. A theoretical framework outlined in this section can be used to highlight the key common and distinct characteristics of all these spin-torque phenomena (Fernández-Rossier *et al.*, 2003; Zhang and Li, 2004; Vanhaverbeke and Viret, 2007; Ralph and Stiles, 2008; Nemec *et al.*, 2012; De Ranieri *et al.*, 2013; Tesarova *et al.*,
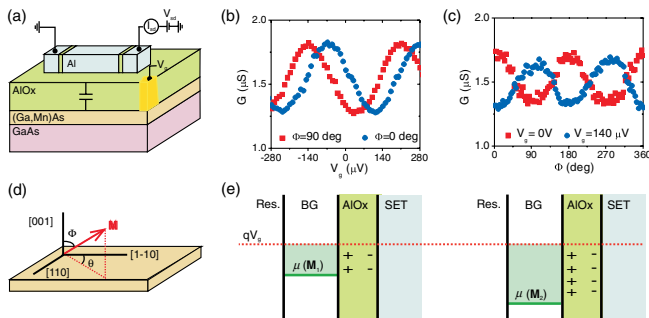


FIG. 24 (color online). (a) Schematic showing the SET channel separated by AlO$_x$ dielectric from the ferromagnetic (Ga,Mn)As back gate (BG). The SET comprises Al leads and island, and AlO$_x$ tunnel barriers. (b) Coulomb oscillations for the SET on Ga$_{0.97}$Mn$_{0.03}$As for two different polar angles $\Phi$ of the magnetization. (c) Magneto-Coulomb oscillations shown by the same SET by varying the angle of magnetization for two different gate voltages. (d) Magnetization vector with respect to (Ga,Mn)As crystal axes. (e) Schematic explaining the spin-gating phenomenon: reorientation of the magnetization from $\mathbf{M}_1$ to $\mathbf{M}_2$ causes a change in the chemical potential of the (Ga,Mn)As BG. This causes charge to flow onto the back gate from the reservoir (Res.). The net effect is to alter the charge on the back gate and therefore the SET conductance. The externally applied electrochemical potential on the gate $\mu_{ec} = qV_g$ is held constant. From Ciccarelli *et al.*, 2012.

2013). At the end of this section we also introduce the Onsager related reciprocal effects to the STT (spin pumping) and to the SOT (Tserkovnyak *et al.*, 2005; Hals, Brataas, and Tserkovnyak, 2010).

The framework for describing spin-torque phenomena treats the nonequilibrium spin density of carriers **s** and magnetization of the ferromagnet as separate degrees of freedom and explores their coupled dynamics. The dilute-moment ferromagnetic semiconductor (Ga,Mn)As is a model system in which the separation is well justified microscopically; magnetization is primarily due to Mn *d*-orbital local moments while the carrier states near the top of the valence band (or bottom of the conduction band) are dominated by As *p* orbitals (or Ga *s* orbitals).

The carrier Hamiltonian can be written as

$$H = H_0 + H_{\mathrm{ex}} + H_{\mathrm{so}}, \tag{4}$$

where $H_0$ is the spin-independent part of the Hamiltonian, the kinetic-exchange term

$$H_{\mathrm{ex}} = J\mathbf{M} \cdot \boldsymbol{\sigma}, \tag{5}$$

where $J$ is the exchange-coupling constant (in units of energy × volume), $\mathbf{M} = cS\hat{\mathbf{M}}$ ($S = 5/2$) is the spin density of Mn local moments, $\hat{\mathbf{M}}$ is the magnetization unit vector, $\boldsymbol{\sigma}$ is the carrier spin operator, and $H_{\mathrm{so}}$ is the spin-orbit coupling Hamiltonian. The current-induced and optical STT phenomena are determined by the following dynamics equations for the nonequilibrium carrier-spin density **s** and for the magnetic moment density **M**,

$$\frac{d\mathbf{s}}{dt} = \frac{J}{\hbar}\mathbf{s} \times \mathbf{M} + P\mathbf{n} - \frac{\mathbf{s}}{\tau_s}, \tag{6}$$

$$\frac{d\mathbf{M}}{dt} = \frac{J}{\hbar}\mathbf{M} \times \mathbf{s}. \tag{7}$$

The first term on the right-hand side of Eq. (6) is obtained from the Hamiltonian dynamics,

$$\frac{d\langle\boldsymbol{\sigma}\rangle}{dt} = \frac{1}{i\hbar}\langle[\boldsymbol{\sigma}, H]\rangle, \tag{8}$$

where $\langle\cdots\rangle$ represents quantum-mechanical averaging over the nonequilibrium carrier states, $\langle\boldsymbol{\sigma}\rangle = \mathbf{s}$, and $H_{\mathrm{so}}$ was neglected in $H$ for the STT effects which are basically nonrelativistic. The second term in Eq. (6) is the rate $P$ of carriers with spin polarization along a unit vector **n** injected from an external polarizer. In the current-induced STT, the external polarizer may be, e.g., an adjacent magnetic layer in a multilayer structure. In the optical STT, $P$ and **n** of non-equilibrium photocarrier spins are governed again by the properties of an external polarizer which are the intensity, propagation axis, and helicity of the circularly polarized pump laser pulse. The last term in Eq. (6) reflects a finite spin lifetime of the nonequilibrium carriers in the ferromagnet.

Two components of the STT can be distinguished when considering two limiting cases of Eq. (6) (Fernández-Rossier *et al.*, 2003; Zhang and Li, 2004; Vanhaverbeke and Viret, 2007; Ralph and Stiles, 2008; Nemec *et al.*, 2012). One limit

is when the carrier spin lifetime $\tau_s \gg \tau_{\mathrm{ex}}$, where the carrier precession time $\tau_{\mathrm{ex}} = \hbar/JcS$. In this limit the last term on the right-hand side of Eq. (6) can be neglected and introducing the steady-state solution of Eq. (6) ($d\mathbf{s}/dt = 0$),

$$\mathbf{s} = P\tau_{\mathrm{ex}}(\mathbf{n} \times \hat{\mathbf{M}}), \tag{9}$$

into Eq. (7) yields the antidamping adiabatic STT (Berger, 1996; Slonczewski, 1996),

$$\frac{d\mathbf{M}}{dt} = P\hat{\mathbf{M}} \times (\mathbf{n} \times \hat{\mathbf{M}}). \tag{10}$$

(Recall that the form of this torque is the same as the damping term in the Landau-Lifshitz-Gilbert equation.) In this adiabatic STT the entire spin-angular momentum of the injected carriers is transferred to the magnetization, independent of $\tau_s$, $\tau_{\mathrm{ex}}$, and other parameters of the system. The adiabatic STT has been considered since the seminal theory works (Berger, 1996; Slonczewski, 1996) on carrier induced magnetization dynamics which opened a large field ranging from metal magnetic tunnel junctions switched by the current to tunable oscillators (Ralph and Stiles, 2008) and ultrafast photomagnetic laser excitations of ferromagnetic semiconductors (Fernández-Rossier *et al.*, 2003; Nemec *et al.*, 2012).

In the opposite limit of $\tau_s \ll \tau_{\mathrm{ex}}$, the first term on the right-hand side of Eq. (6) can be neglected resulting in the fieldlike nonadiabatic STT (Zhang and Li, 2004),

$$\frac{d\mathbf{M}}{dt} = \frac{\tau_s}{\tau_{\mathrm{ex}}}P(\hat{\mathbf{M}} \times \mathbf{n}). \tag{11}$$

The nonadiabatic STT is perpendicular to the adiabatic STT and only a fraction $\tau_s/\tau_{\mathrm{ex}}$ of the injected spin-angular momentum is transferred to the magnetization. For intermediate ratios $\tau_{\mathrm{ex}}/\tau_s$, both the nonadiabatic and adiabatic torques are present and the ratio of their magnitudes (nonadiabatic to adiabatic) is given by $\beta = \tau_{\mathrm{ex}}/\tau_s$ (Fernández-Rossier *et al.*, 2003; Zhang and Li, 2004; Vanhaverbeke and Viret, 2007). The nonadiabatic STT plays a crucial role in current-induced DW motion (Zhang and Li, 2004; Metaxas *et al.*, 2007; Mougin *et al.*, 2007; Vanhaverbeke and Viret, 2007) and, as we discuss, (Ga,Mn)As is a favorable material for exploring the effects of the nonadiabatic and adiabatic STTs.

The SOT is distinct from the STT as it is a relativistic phenomenon in which magnetization dynamics is induced in a uniform spin-orbit coupled ferromagnet in the absence of the external polarizer (Linnarsson *et al.*, 1997; Bernevig and Vafek, 2005; Manchon and Zhang, 2008, 2009; Chernyshov *et al.*, 2009; Endo, Matsukura, and Ohno, 2010; Garate and MacDonald, 2009; Fang *et al.*, 2011; Gambardella and Miron, 2011; Liu *et al.*, 2012; Kurebayashi *et al.*, 2014). The Hamiltonian spin dynamics described by Eq. (8) with the $H_{\mathrm{so}}$ term included in the carrier Hamiltonian implies that Eq. (6) is replaced with

$$\frac{d\mathbf{s}}{dt} = \frac{J}{\hbar}\mathbf{s} \times \mathbf{M} + \frac{1}{i\hbar}\langle[\boldsymbol{\sigma}, H_{\mathrm{so}}]\rangle. \tag{12}$$

The SOT is obtained by introducing the steady-state solution of Eq. (12) into Eq. (7),

$$\frac{d\mathbf{M}}{dt} = \frac{J}{\hbar}\mathbf{M} \times \mathbf{s} = \frac{1}{i\hbar}\langle[\boldsymbol{\sigma}, H_{\mathrm{so}}]\rangle. \tag{13}$$

In the current-induced SOT the absence of an external polarizer implies that the effect can be observed when electrical current is driven through a uniform magnetic structure (Linnarsson *et al.*, 1997; Bernevig and Vafek, 2005; Manchon and Zhang, 2008, 2009; Chernyshov *et al.*, 2009; Endo, Matsukura, and Ohno, 2010; Garate and MacDonald, 2009; Fang *et al.*, 2011; Gambardella and Miron, 2011; Kurebayashi *et al.*, 2014). The optical SOT analogy of the absence of an external polarizer is that the nonequilibrium photocarriers are excited by helicity independent pump laser pulses which do not impart angular momentum (Tesarova *et al.*, 2013).

The electrical and optical SOTs may differ in the specific contributions to $H_{\mathrm{so}}$ which dominate the effect. This can be illustrated considering the Boltzmann linear-response transport theory of the current-induced SOT. Here $\langle\cdots\rangle$ represents quantum-mechanical averaging constructed from the equilibrium eigenstates of $H$ and with the nonequilibrium steady state entering through an asymmetric redistribution of the occupation numbers of these eigenstates on the Fermi surface due to the applied electrical drift and relaxation. Because of this specific form of the asymmetric nonequilibrium charge redistribution with a conserved total number of carriers, the current-induced SOT requires broken inversion symmetry terms in $H_{\mathrm{so}}$ (Manchon and Zhang, 2008, 2009; Chernyshov *et al.*, 2009; Garate and MacDonald, 2009; Miron *et al.*, 2010; Fang *et al.*, 2011). The optical SOT is caused by optical generation and relaxation of photocarriers without an applied drift (without a defined direction of the carrier flow) and without conserving the equilibrium number of carriers in the dark. Therefore, the broken inversion symmetry in the crystal is not required, and inversion symmetric $H_{\mathrm{so}}$ plus the time-reversal symmetry breaking the exchange-coupling term in the carrier Hamiltonian are sufficient for observing the optical SOT.

In the STT, spin-angular momentum is transferred from the carriers to the magnet, applying a torque to the magnetization. Via the STT, the injected spin current is able to excite magnetization dynamics. A reciprocal effect to the STT is the spin-pumping phenomenon in which pure spin current is generated from magnetization precession (Mizukami, Ando, and Miyazaki, 2001; Tserkovnyak *et al.*, 2005). The spin pumping has been measured, e.g., in ferromagnet–normal-metal–ferromagnet GMR structures (Heinrich *et al.*, 2003; Woltersdorf *et al.*, 2007) or in ferromagnet–normal-metal bilayers (Saitoh *et al.*, 2006; Czeschka *et al.*, 2011). In the latter structure, the inverse SHE in the spin-orbit coupled paramagnet adjacent to the ferromagnet serves as a spin-charge converter and provides a direct means for detecting the spin-pumping phenomenon electrically. Spin pumping can, therefore, be used not only for probing magnetization dynamics in ferromagnets but also spin physics in paramagnets, e.g., for measuring the SHE angles. Magnetization dynamics of ferromagnetic resonance also produces electrical signals in the ferromagnetic layer through galvanomagnetic effects. Experiments in a (Ga, Mn)As/*p*-GaAs model system, where sizable galvanomagnetic effects are present, have demonstrated that neglecting the galvanomagnetic effects in the

ferromagnet can lead to a large overestimate of the SHE angle in the paramagnet. The study has also shown a method to separate voltages of these different origins in the spin-pumping experiments in the ferromagnet-paramagnet bilayers (Chen, Matsukura, and Ohno, 2013).

The Onsager reciprocity relations imply that, as for the STT and spin pumping, there exists a reciprocal phenomenon of the SOT in which the electrical signal is generated from magnetization precession in a uniform, spin-orbit coupled magnetic system with broken spatial inversion symmetry (Hals, Brataas, and Tserkovnyak, 2010; Tatara, Nakabayashi, and Lee, 2013). In this reciprocal SOT effect no secondary spin-charge conversion element is required and, as for the SOT, (Ga,Mn)As with broken inversion symmetry in its bulk crystal structure and strongly spin-orbit coupled holes represents a favorable model system to explore this phenomenon.

### 6. Current-induced spin-transfer torque

In this section we focus on the current-induced STT studies in (Ga,Mn)As. The dilute-moment ferromagnet (Ga,Mn)As has a low saturation magnetization, as compared to conventional dense-moment metal ferromagnets. Together with the high degree of spin polarization of carriers it implies that electrical currents required to excite magnetization by STT in (Ga,Mn)As are also comparatively low. In magnetic tunnel junctions with (Ga,Mn)As electrodes, STT induced switching was observed at current densities of the order $10^4$–$10^5$ A cm$^{-2}$ (Chiba *et al.*, 2004), consistent with theory expectations (Sinova, Jungwirth *et al.*, 2004). These are 1–2 orders of magnitude lower current densities than in the STT experiments in common dense-moment metal ferromagnets.

Current-induced DW motion in the creep regime at $\sim 10^5$ A cm$^{-2}$ current densities was reported and thoroughly explored in perpendicularly magnetized (Ga,Mn)As thin-film devices, shown in Fig. 25 (Yamanouchi *et al.*, 2004, 2006,
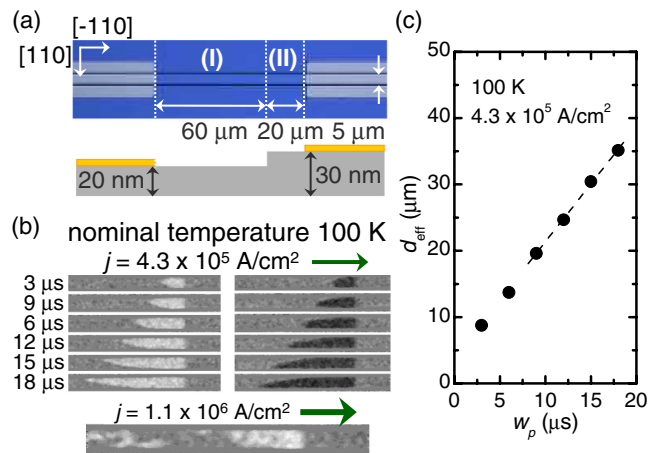
FIG. 25 (color online). (a) Layout of the device showing the 5 $\mu$m mesa and step for DW pinning in perpendicular magnetic anisotropy (Ga,Mn)As film. (b) 7 $\mu$m wide magneto-optical images with a 5 $\mu$m mesa in the center show that DW moves in the opposite direction to the current independent of the initial magnetization orientation, and that DW displacement is proportional to pulse duration (c). The lowest panel in (b) shows destruction of the ferromagnetic phase by Joule heating. From Yamanouchi *et al.*, 2006.

2007; Chiba *et al.*, 2006). The perpendicular magnetization geometry was achieved by growing the films under a tensile strain on a (In,Ga)As substrate and allowed for a direct magneto-optical Kerr-effect imaging of the magnetic domains, as illustrated in Fig. 25.

Alternatively, tensile-strained perpendicularly magnetized films for DW studies were grown on a GaAs substrate with P added into the magnetic film (Wang *et al.*, 2010; Curiale *et al.*, 2012; De Ranieri *et al.*, 2013). In high crystal quality $(Ga, Mn)(As, P)/GaAs$ epilayers the viscous flow regime was achieved over a wide current range allowing one to observe (De Ranieri *et al.*, 2013) the lower-current steady DW motion regime separated from a higher-current precessional regime by the Walker breakdown (WB) (Thiaville *et al.*, 2005; Metaxas *et al.*, 2007; Mougin *et al.*, 2007). This in turn enabled one to assess the ratio of adiabatic and nonadiabatic STTs in the current driven DW motion. When the non-adiabatic STT is strong enough that $\beta/\alpha > 1$, where $\alpha$ is the DW Gilbert damping parameter, the mobility of a DW (velocity divided by the DW driving current) is larger below the WB. For $\beta/\alpha < 1$, on the other hand, the DW mobility is larger above the WB critical current. From the experiments in (Ga,Mn)(As,P) samples, shown in Fig. 26, it was concluded
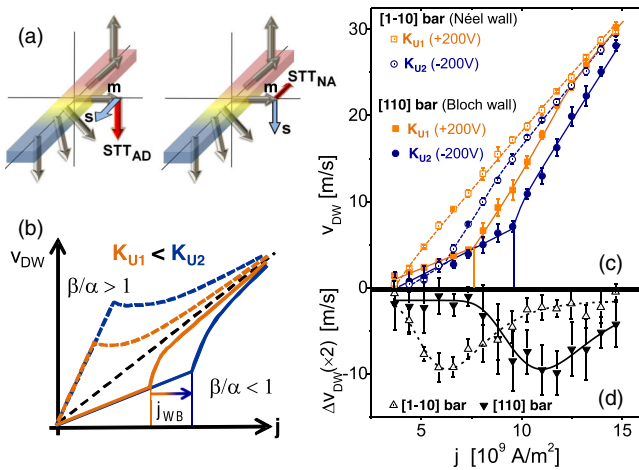
that $1 > \beta/\alpha \gtrsim 0.5$ (De Ranieri *et al.*, 2013), i.e., that the nonadiabatic STT plays a significantly more important role than in conventional transition metals where typically $\beta/\alpha \ll 1$ (Zhang and Li, 2004). Relatively large values of $\beta = \tau_{ex}/\tau_s$, compared to common dense-moment ferromagnets, are both due to larger $\tau_{ex}$ in the dilute-moment ferromagnetic semiconductors and due to smaller $\tau_s$ of the strongly spin-orbit coupled holes in the ferromagnetic semiconductor valence band (Adam *et al.*, 2009; Garate, Gilmore *et al.*, 2009; Hals, Nguyen, and Brataas, 2009; Curiale *et al.*, 2012; De Ranieri *et al.*, 2013).

The combination of low saturation moment and strong spin-orbit coupling has yet another key advantage which is the dominant role of magnetocrystalline anisotropy fields over the shape anisotropy fields. It allows one to control the internal DW structure and stability *ex situ* by strain relaxation in (Ga,Mn)As microstructures (Wunderlich *et al.*, 2007) or *in situ* by a piezoelectric stressor attached to the ferromagnetic semiconductor epilayer (De Ranieri *et al.*, 2013). As a result, the WB critical current can be tuned (Roy and Wunderlich, 2011) resulting in the observed 500% variations of the DW mobility induced by the applied piezovoltage (De Ranieri *et al.*, 2013).

## 7. Current-induced spin-orbit torque

Following the theoretical prediction for III-V zinc-blende crystals with broken inversion symmetry (Bernevig and Vafek, 2005), the experimental discovery of the SOT was reported in a (Ga,Mn)As device whose image is shown Fig. 27(a) (Chernyshov *et al.*, 2009). The sample was patterned into a circular device with eight nonmagnetic Ohmic contacts [Fig. 27(a)]. In the presence of a saturating external magnetic



FIG. 26. (color online). (a) Illustration of the steady-state non-equilibrium carrier spin polarization **s** and corresponding adiabatic STT ($STT_{AD}$) acting on magnetization **m** in the $\tau_s \gg \tau_{ex}$ limit (left) and nonadiabatic STT ($STT_{NA}$) in the $\tau_s \ll \tau_{ex}$ limit (right). (b) Schematic diagram of the predicted DW velocity as a function of the driving current in the presence of adiabatic and nonadiabatic STTs and $\beta/\alpha < 1$ or $\beta/\alpha > 1$, and of the predicted shift of the WB threshold current $j_{WB}$ for two values of the in-plane magnetocrystalline constant $K_{u,1} < K_{u,2}$, controlled *in situ* by a piezostressor. (c) Measured DW velocity vs driving current density at piezovoltages $-200$ or $+200$ V, strengthening or weakening the $[1\bar{1}0]$ in-plane easy axis, respectively. Open symbols correspond to the $[1\bar{1}0]$-oriented microbar with less internally stable Néel DW and filled symbols to the [110]-oriented microbar with more internally stable Bloch DW. The character of the measured data, including the shift of the WB threshold current, implies STTs with $\beta/\alpha < 1$. (d) $\Delta v_{DW} = v_{DW}(+200 \text{ V}) - v_{DW}(-200 \text{ V})$ vs current density illustrates the piezoelectric control of the DW mobility achieved starting from lower currents in the $[1\bar{1}0]$-oriented microbar with less internally stable DW. From De Ranieri *et al.*, 2013.
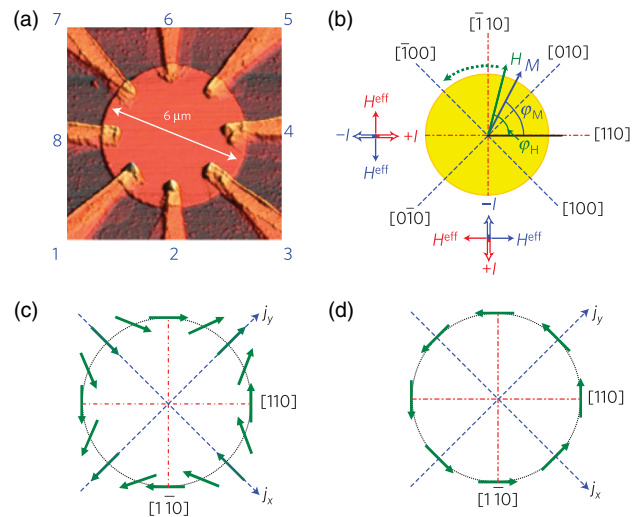


FIG. 27 (color online). (a) Atomic force micrograph of the studied sample with eight nonmagnetic metal contacts. (b) Diagram of device orientation with respect to crystallographic axes, with easy and hard magnetization axes marked with dashed and dot-dashed lines, respectively. Measured directions of the $H_{eff}$ field are shown for different current directions. Orientation of the effective SOT field with respect to the current direction for (c) Dresselhaus and (d) Rashba spin-orbit interactions. From Chernyshov *et al.*, 2009.

field $H$, the magnetization of the (Ga,Mn)As sample is aligned with the field. For weak fields, however, the direction of magnetization is primarily determined by magnetic anisotropy. As a small field ($5 < H < 20$ mT) is rotated in the plane of the sample, the magnetization is realigned along the easy axis closest to the field direction. Such rotation of magnetization by an external field is demonstrated in Figs. 28(a) and 28(b). For the current $\mathbf{I} \| [1\bar{1}0]$, the measured transverse AMR ($R_{xy}$) is positive for $\mathbf{M} \| [100]$ and negative for $\mathbf{M} \| [010]$. The switching angles where $R_{xy}$ changes sign are denoted as $\varphi_H^{(i)}$ on the plot. The data can be qualitatively understood if one considers an extra current-induced effective magnetic field $H_{\text{eff}}$, as shown in Fig. 27(b). The symmetry of the measured $H_{\text{eff}}$ with respect to the direction of current is sketched in Fig. 27(c) and this current-induced SOT field has been shown to allow for reversibly switching magnetization between the [010] and [$\bar{1}$00] directions at a fixed magnetic field when applying positive and negative current pulses with the current $\mathbf{I} \| [1\bar{1}0]$, as shown in Fig. 28(c). It was also demonstrated that the SOT in (Ga,Mn)As can generate a 180° magnetization reversal in the absence of an external magnetic field (Endo, Matsukura, and Ohno, 2010). Apart from the current-induced magnetization switching of a uniform ferromagnet, the SOT was shown to provide the means for developing an all-electrical broadband FMR technique applicable to individual nanomagnets (Fang *et al.*, 2011). The SOT-FMR was used for determining micromagnetic parameters of (Ga,Mn)As nanobars which were not accessible by conventional FMR t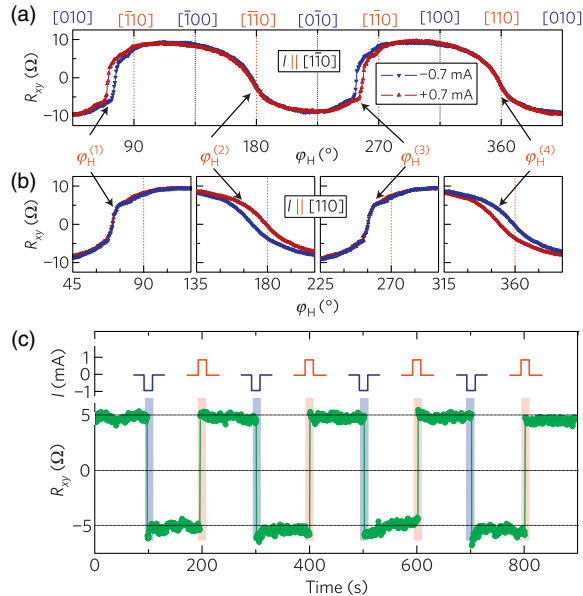echniques and simultaneously allowed to perform 3D vector magnetometry on the driving SOT fields (Fang *et al.*, 2011; Kurebayashi *et al.*, 2014).

The SOT fields of the Dresselhaus and Rashba symmetries shown in Figs. 27(c), and 27(d), respectively, can arise in (Ga,Mn)As due to the following broken inversion symmetry terms in the spin-orbit-coupling Hamiltonian:

$$H_{\text{so}}^{D,R} = -3C_4[\sigma_x k_x(\epsilon_{yy} - \epsilon_{zz}) - \sigma_y k_y(\epsilon_{xx} - \epsilon_{zz})] - 3C_5[(\sigma_x k_y - \sigma_y k_x)\epsilon_{xy}]. \tag{14}$$

The first Dresselhaus term is due to the broken inversion symmetry of the host zinc-blende lattice combined with the growth-induced strain in the (Ga,Mn)As epilayer ($\epsilon_{xx} = \epsilon_{yy} \neq \epsilon_{zz}$) while the second Rashba term combines the zinc-blende inversion asymmetry with a shear strain in the epilayer ($\epsilon_{xy} \neq 0$) (Silver *et al.*, 1992; Chernyshov *et al.*, 2009; Stefanowicz *et al.*, 2010; Fang *et al.*, 2011; Kurebayashi *et al.*, 2014). Chernyshov *et al.* (2009) identified a Dresselhaus SOT field corresponding to a compressively strained (Ga,Mn)As epilayer grown on a GaAs substrate. Fang *et al.* (2011) observed a sign change of the Dresselhaus SOT field between (Ga, Mn)As/GaAs and (Ga, Mn)(As, P)/GaAs samples consistent with the change in the growth-induced strain in the epilayer from compressive in the former sample to tensile in the latter sample. A weaker Rashba SOT field was also observed in these experiments (Fang *et al.*, 2011). The shear-strain component which yields the Rashba SOT field is not physically present in the crystal structure of (Ga,Mn)As epilayers. It has been introduced, however, in magnetization and SOT studies to effectively model the in-plane uniaxial anisotropy present in (Ga,Mn)As epilayers (Sawicki *et al.*, 2005; Zemen *et al.*, 2009; Fang *et al.*, 2011).

The correspondence between the in-plane Dresselhaus and Rashba spin-orbit Hamiltonian terms in Eq. (14) and the in-plane SOT fields shown in Figs. 27(c) and 27(d) can be understood from Eq. (13) within the Boltzmann transport theory description of the nonequilibrium state. In this semi-classical transport theory, the linear response of the carrier system to the applied electric field is described by the nonequilibrium distribution function of carrier eigenstates which are considered to be unperturbed by the electric field. The form of the nonequilibrium distribution function is obtained by accounting for the combined effects of the carrier acceleration in the field and of scattering. In particular, the nonequilibrium distribution function is used here to evaluate the current-induced SOT.

Equation (13) explicitly shows that the SOT is nonzero only when both the exchange and spin-orbit fields act on the carrier states. However, when evaluating the SOT from $(J/\hbar)\mathbf{M} \times \langle\boldsymbol{\sigma}\rangle$, where part of the effect of the exchange field is explicitly factored out in the expression, an approximate form of the SOT can be obtained by considering in $\langle\boldsymbol{\sigma}\rangle$ eigenstates of the Hamiltonian $H$ with $H_{\text{ex}}$ neglected. Since the resulting

$$\mathbf{s} = \langle\boldsymbol{\sigma}\rangle = \frac{1}{V}\sum_{n,\mathbf{k}} \boldsymbol{\sigma}_{n,\mathbf{k}} g_{n,\mathbf{k}} \tag{15}$$

is independent of $\mathbf{M}$ this approximate form describes a pure fieldlike SOT whose origin is illustrated in Fig. 29 for the



FIG. 28 (color online). (a), (b) Transverse anisotropic magnetoresistance $R_{xy}$ as a function of external field direction $\varphi_H$ for $H = 10$ mT and current $I = \pm 0.7$ mA. The angles $\varphi_H^{(i)}$ mark magnetization switchings. (c) Magnetization switches between the [010] and [$\bar{1}$00] directions when alternating $I = \pm 1$ mA current pulses are applied with the current $\mathbf{I} \| [1\bar{1}0]$. The pulses have 100 ms duration and are shown schematically above the data curve. $R_{xy}$ is measured with $I = 10$ $\mu$A. Adapted from Chernyshov *et al.*, 2009.
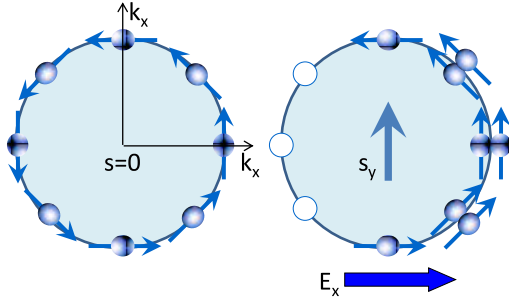
FIG. 29 (color online). Left panel: Rashba spin texture in equilibrium with zero net spin density. Right panel: Nonequilibrium redistribution of eigenstates in applied electric field resulting in a nonzero spin density due to broken inversion symmetry of the spin texture.

Rashba spin-orbit coupling (analogous images apply for the Dresselhaus or another broken inversion symmetry $H_{so}$). The nonequilibrium spin density in the $H_{ex} = 0$ approximation is a direct consequence of an electric field and scattering induced redistribution of carriers $g_{n,\mathbf{k}}$ on the Fermi surface whose texture of spin expectation values $\sigma_{n,\mathbf{k}}$ has a broken inversion symmetry. For the Rashba spin-orbit coupling, the in-plane nonequilibrium spin polarization is perpendicular to the applied electric field for all crystal directions of the electric field. For the Dresselhaus spin-orbit coupling the relative angle between the in-plane nonequilibrium spin polarization and the applied electric field depends on the crystal direction of the electric field [see Fig. 27(c)]. This current-induced spin-polarization phenomenon was discussed in nonmagnetic semiconductors (Aronov and Lyanda-Geller, 1989; Edelstein, 1990; Ganichev *et al.*, 2002) prior to the SOT experiments in (Ga,Mn)As. An analogous fieldlike SOT mechanism was subsequently considered in nonmagnetic and ferromagnetic transition-metal bilayers with broken structural inversion symmetry at the interface (Manchon *et al.*, 2008; Manchon and Zhang, 2009; Miron *et al.*, 2010).

Studies of the SOT in (Ga,Mn)As have identified an additional, antidamping SOT contribution which has a common microscopic origin with the intrinsic SHE (Kurebayashi *et al.*, 2014). Unlike the above scattering-related fieldlike SOT, described within the semiclassical Boltzmann theory, the presence of an antidamping SOT with a scattering-independent origin is captured by the time-dependent quantum-mechanical perturbation theory. Here the linear-response theory considers the equilibrium distribution function and the applied electric field perturbs the carrier wave functions. This can be visualized by solving the Bloch equations of the carrier spin dynamics during the acceleration of the carriers in the applied electric field, i.e., between the scattering events, as shown in Fig. 30 (Kurebayashi *et al.*, 2014). In the limit of large $H_{ex}$ compared to $H_{so}$ the spins are approximately aligned with the exchange field in equilibrium. During the acceleration, the field acting on the carriers acquires a time-dependent component due to $H_{so}$, as illustrated in Fig. 30(b) for the Rashba spin-orbit coupling. This yields a nonequilibrium spin reorientation. In the linear response, i.e., for small tilts of the spins from equilibrium, the carriers acquire a time and momentum-independent out-of-plane component, resulting in a net out-of-plane spin density proportional to the strength of the spin-orbit field and inverse
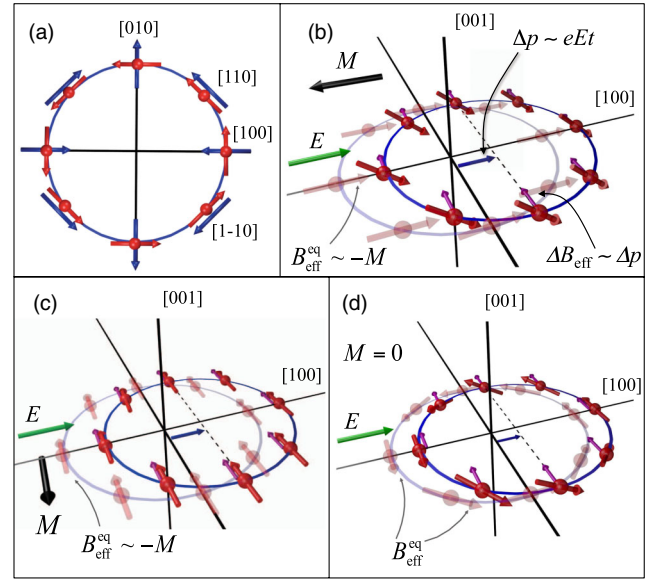


FIG. 30 (color online). (a) Rashba and Dresselhaus spin textures. (b) For the case of a Rashba-like symmetry, the out-of-plane nonequilibrium carrier spin density that generates the intrinsic antidamping SOT has a maximum for $\mathbf{E}$ (anti)parallel to $\mathbf{M}$. In this configuration the equilibrium effective field $B_{eff}^{eq}$ and the additional field $\Delta B_{eff} \perp \mathbf{M}$ due to the acceleration are perpendicular to each other causing all spins to tilt in the same out-of-plane direction. (c) For the case of a Rashba-like symmetry, the out-of-plane nonequilibrium carrier spin density is zero for $\mathbf{E} \perp \mathbf{M}$ since $B_{eff}^{eq}$ and $\Delta B_{eff}$ are parallel to each other. (d) The analogous physical phenomena for zero magnetization induces a tilt of the spin out of the plane that has opposite sign for momenta pointing to the left or the right of the electric field, inducing in this way the intrinsic SHE. From Sinova, Culcer *et al.*, 2004, and Kurebayashi *et al.*, 2014.

proportional to the strength of the exchange field (Kurebayashi *et al.*, 2014).

As illustrated in Figs. 30(b) and 30(c), the nonequilibrium out-of-plane spin density $s_z$ depends on the direction of the magnetization $\mathbf{M}$ with respect to the applied electric field. For the Rashba spin-orbit coupling it has a maximum for $\mathbf{M}$ (anti) parallel to $\mathbf{E}$ and vanishes for $\mathbf{M}$ perpendicular to $\mathbf{E}$. For a general angle $\theta_{\mathbf{M}-\mathbf{E}}$ between $\mathbf{M}$ and $\mathbf{E}$, $s_z \sim \cos\theta_{\mathbf{M}-\mathbf{E}}$. The nonequilibrium spin polarization produces an out-of-plane field which exerts a torque on the in-plane magnetization given by Eq. (13). This intrinsic SOT is antidamping like,

$$\frac{d\mathbf{M}}{dt} = \frac{J}{\hbar}(\mathbf{M} \times s_z \hat{z}) \sim \mathbf{M} \times ([\mathbf{E} \times \hat{z}] \times \mathbf{M}). \qquad (16)$$

For the Rashba spin-orbit coupling, Eq. (16) applies to all directions of the applied electric field with respect to crystal axes. In the case of the Dresselhaus spin-orbit coupling, the symmetry of the antidamping SOT depends on the direction of $\mathbf{E}$ with respect to crystal axes, as seen in Fig. 30(a).

To highlight the analogy between the intrinsic antidamping SOT and the intrinsic SHE (Murakami, Nagaosa, and Zhang, 2003; Sinova, Culcer *et al.*, 2004) the solution of the Bloch equations in the absence of the exchange Hamiltonian term is illustrated in Fig. 30(d) (Sinova, Culcer *et al.*, 2004). In the
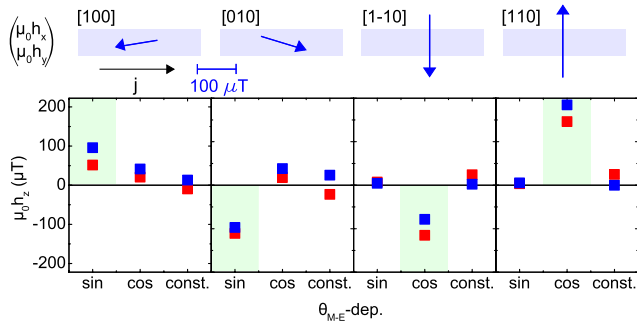
FIG. 31 (color online). Measured in-plane and out-of-plane SOT fields in (Ga.Mn)As. In-plane spin-orbit field and coefficients of the $\cos\theta_{M-E}$ and $\sin\theta_{M-E}$ fits to the angle dependence of the out-of-plane SOT field for our sample set. For the in-plane fields, a single sample in each microbar direction is shown (corresponding to the same samples that yield the out-of-plane data points). In the out-of-plane data, two samples are shown in each microbar direction. The symmetries expected for the antidamping SOT, on the basis of the theoretical model for the Dresselhaus term in the spin-orbit interaction, are shown by shading. All data are normalized to a current density of $10^5$ A cm$^{-2}$. From Kurebayashi *et al.*, 2014.

SHE case, the sense of the out-of-plane spin rotation depends on the carrier momentum resulting in a nonzero transverse spin current but no net nonequilibrium spin density.

The antidamping like SOT with the theoretically predicted symmetries was identified in measurements in (Ga,Mn)As, as shown in Fig. 31 (Kurebayashi *et al.*, 2014). The all-electrical broadband SOT-FMR technique (Fang *et al.*, 2011) was applied which allowed one to perform 3D vector magnetometry on the driving SOT fields. Since the magnitudes of the measured out-of-plane and in-plane SOT fields are comparable, the antidamping SOT plays an important role in driving the magnetization dynamics in (Ga,Mn)As.

The observation of the intrinsic antidamping like SOT in (Ga,Mn)As has direct consequences also for the physics of in-plane current-induced torques in the transition-metal bilayers (Miron *et al.*, 2011; Liu *et al.*, 2012). Here the antidamping like SOT considered at the broken inversion symmetry interface can compete with another, conceptually distinct mechanism in which the intrinsic SHE in the paramagnet generates a spin current which upon entering the ferromagnet exerts an antidamping STT on the magnetization (Liu *et al.*, 2012). It has been mentioned above that the nonequilibrium spin density in the intrinsic antidamping SOT scales with the strength of the spin-orbit field and with the inverse of the strength of the exchange field. Similarly, the SHE spin current, which takes the role of the spin-injection rate $P$ in Eq. (9) for the nonequilibrium spin density $s$ in the adiabatic STT, scales with the strength of the spin-orbit coupling in the paramagnetic metal (Tanaka *et al.*, 2008) and $s$ in the adiabatic STT is inverse proportional to the exchange field [Eq. (9)].

## C. Interaction of spin with light

### 1. Magneto-optical effects

Similar to the dc conductivity, the unpolarized finite-frequency absorption spectra (Burch *et al.*, 2006; Jungwirth

*et al.*, 2007, 2010; Chapler *et al.*, 2011) show signatures of the vicinity of the metal-insulator transition and of strong disorder effects even in the most metallic (Ga,Mn)As materials, as illustrated in Fig. 32. Compared to a shallow-acceptor counterpart such as, e.g., C-doped GaAs [see the inset of Fig. 32(c)], the spectral weight in (Ga,Mn)As is shifted from the low-frequency Drude peak to higher frequencies. The ac conductivity scales with the dc conductivity over a broad range of Mn dopings and does not strongly reflect the spin-dependent interactions in the system.

Magneto-optical spectroscopies, on the other hand, provide a detailed probe into the exchange split and spin-orbit coupled electronic structure of (Ga,Mn)As (Ando *et al.*, 1998, 2008; Kuroiwa *et al.*, 1998; Beschoten *et al.*, 1999; Szczytko *et al.*, 1999; Komori *et al.*, 2003; Moore *et al.*, 2003; Kimel *et al.*, 2005; Lang *et al.*, 2005; Chakarvorty *et al.*, 2007; Acbas *et al.*, 2009; Tesarova, Nemec *et al.*, 2012; Tesarova, Subrt
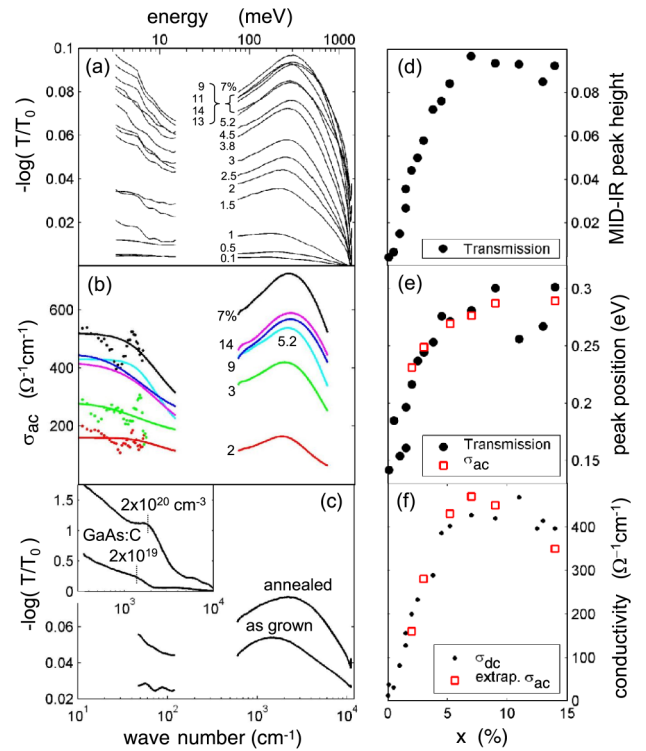


FIG. 32 (color online). (a) Infrared absorption of a series of optimized (Ga, Mn)As/GaAs epilayers with nominal Mn doping $x = 0.1\%–14\%$ plotted from the measured optical transmissions of the samples ($T$) and of the reference bare GaAs substrate ($T_0$). (b) Real part of the ac conductivity (lines) obtained from the measured complex conductivity in the terahertz range (points) and from fitting the complex conductivity in the infrared range to the measured transmissions. (c) Comparison of the infrared absorption in as-grown and annealed 4.5% doped sample. Inset: Comparison to GaAs:C samples with carbon doping densities $2 \times 10^{19}$ and $2 \times 10^{20}$ cm$^{-3}$. (d) Height of the (Ga,Mn)As midinfrared absorption peak as a function of Mn doping. (e) Position of the peak inferred from the transmission measurements and from the fitted ac conductivities. (f) Zero frequency conductivities obtained from dc transport measurements and from extrapolated optical ac conductivities measured in the terahertz range. From Jungwirth *et al.*, 2010.

*et al.*, 2012; Tesarova *et al.*, 2014). It implies that they can be used as sensitive optical spin-detection tools, as illustrated in Fig. 33 (Kimel *et al.*, 2005).

For the light propagating in the perpendicular direction to the sample surface the magneto-optical effects can be classified in the following way (Tesarova *et al.*, 2014): The magnetic circular birefringence (MCB) is given by the real part of the difference between refractive indices of two circularly polarized modes with opposite helicities and the magnetic circular dichroism (MCD) is given by its imaginary part. These magneto-optical coefficients are sensitive to the out-of-plane component of the magnetization, are an odd function of **M**, and represent the finite-frequency counterparts of the AHE. The magnetic linear birefringence (MLB) is given by the real part of the difference between refractive indices of two modes linearly polarized perpendicular and parallel to the magnetization and the magnetic linear dichroism (MLD) is given by its imaginary part. These magneto-optical coefficients are sensitive to the in-plane components of the magnetization, are an even function of **M**, and represent the finite-frequency counterparts of the AMR.

Both the circular and linear magneto-optical effects can cause a rotation (and ellipticity) of the polarization of a transmitted or reflec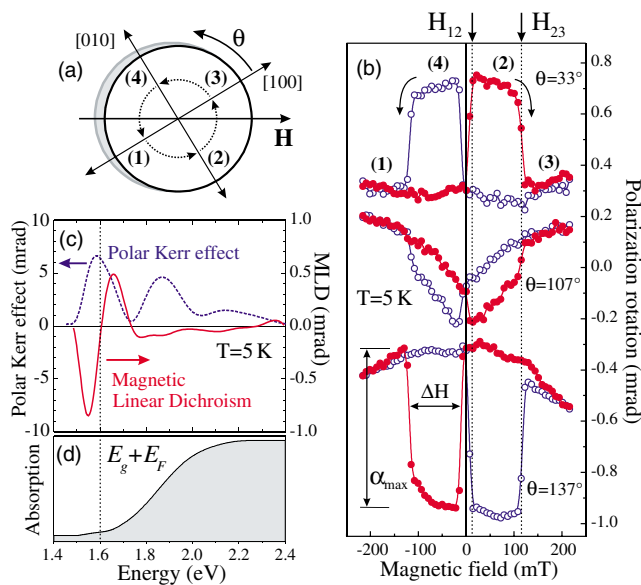ted linearly polarized light. For the rotation originating from the MCB and MCD the effects are referred to as the Faraday effect in transmission and the Kerr effect in reflection. For the rotation originating from the MLB and MLD the terminology is not unified across the literature (Tesarova *et al.*, 2014); however, it is clearly distinguishable from the Kerr (Faraday) rotation. While the Kerr (Faraday) rotation is independent of the polarization angle of the incident light, the rotation originating from the MLB and MLD depends on the angle between the light polarization and the in-plane magnetization. There is a direct analogy between this magneto-optical effect and the transverse voltage in the noncrystalline off-diagonal AMR described by Eq. (2). The transverse voltage in the latter case and the polarization rotation in the former case both have the $\sim \sin \phi$ form, where $\phi$ is the angle between the in-plane magnetization and the applied voltage in the transverse AMR case, and between the in-plane magnetization and the incident-light polarization in the case of the MLB and MLD induced rotation.

Measurements in Fig. 33(b) used the dependence on the polarization angle to optically detect magnetization switchings between [100] and [010] crystal axes in a 2% Mn-doped (Ga,Mn)As sample with a dominant in-plane cubic anisotropy (Kimel *et al.*, 2005). Consistent with the phenomenology of the MLB and MLD induced rotation, the largest signal is observed when the incident-light polarization is aligned with the in-plane diagonal crystal axis. Figures 33(c) and 33(d) highlight the fact that both the Kerr effect and the MLB and MLD induced rotation can be strong in (Ga,Mn)As for a suitably chosen frequency of the probe laser light. This allows for a sensitive optical detection of the in-plane and out-of-plane components of the magnetization.

The decomposition of the magneto-optical signal into the MCB and MCD induced rotation due to the out-of-plane magnetization and the MLB and MLD induced rotation due to in-plane magnetization was also employed to quantitatively determine the three-dimensional magnetization vector trajectory in the time-resolved pump-and-probe magneto-optical measurements in (Ga,Mn)As, as shown in Fig. 34 (Tesarova, Nemec *et al.*, 2012). The technique helped to experimentally identify different mechanisms by which photocarriers can induce magnetization dynamics in the pump-and-probe experiments in (Ga,Mn)As. The recombining photocarriers can heat the lattice and the transient increase of temperature can trigger magnetization dynamics or, on much shorter time scales, the photocarriers can directly induce spin torques acting on the magnetization (Oiwa, Takechi, and Munekata, 2005; Qi *et al.*, 2007, 2009; Takechi *et al.*, 2007; Wang *et al.*, 2007b; Hashimoto, Kobayashi, and Munekata, 2008; Hashimoto and Munekata, 2008; Rozkotová, Nemec, Horodyska *et al.*, 2008, Rozkotová, Němec, Tesařová *et al.*, 2008; Kobayashi *et al.*, 2010; Nemec *et al.*, 2012; Tesarova, Nemec *et al.*, 2012; Tesarova *et al.*, 2013). These effects are reviewed in more detail in Secs. III.C.2 and III.C.3. We note that earlier magneto-optical pump-and-probe studies of photocarriers exchange coupled to local magnetic moments have been performed in nonferromagnetic (II,Mn)VI diluted magnetic semiconductors (Baumberg *et al.*, 1994; Crooker *et al.*, 1996; Camilleri *et al.*, 2001).



FIG. 33 (color online). (a) $Ga_{0.98}Mn_{0.02}As$ sample orientation with respect to the applied magnetic field and the four-step magnetization reversal process as consecutive 90° jumps (shown by dotted arrows) between the four easy directions (1)–(4). (b) Field dependences of the magnetic linear dichroism for different angles $\theta$ between the incident polarization and the [100] crystallographic direction, measured at a wavelength of $\lambda = 815$ nm. (1)–(4) corresponds to the magnetization directions indicated in (a). $H_{12}$ and $H_{23}$ are the magnetic field values required for making jumps $(1) \rightarrow (2)$ and $(2) \rightarrow (3)$, respectively. (c) Spectra of the polar magneto-optical Kerr effect and magnetic linear dichroism (at $\theta = 135°$); (d) absorption spectrum at 5 K. (c), (d) Fabry-Pérot oscillations in the signal due to the finite buffer thickness have been removed numerically using a bandpass filter. From Kimel *et al.*, 2005.
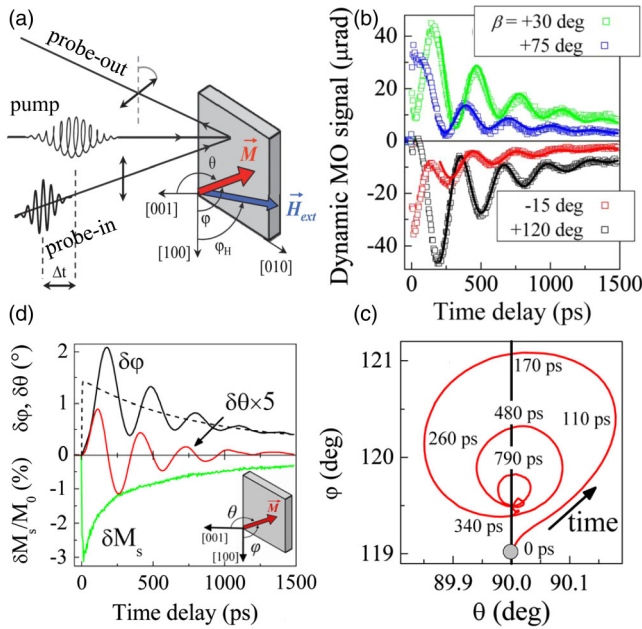
FIG. 34 (color online). (a) Schematic diagram of the experimental setup for a detection of the magnetization precession induced in (Ga,Mn)As by an impact of the femtosecond laser pump pulse. Rotation of the polarization plane of reflected linearly polarized probe pulses is measured as a function of the time delay $\Delta t$ between pump-and-probe pulses. The orientation of magnetization in the sample is described by the in-plane angle $\varphi$ and the out-of-plane angle $\theta$. The external magnetic field $H_{ext}$ is applied in the sample plane at an angle $\varphi_H$. (b) Dynamics of the magneto-optical signal induced by an impact of the pump pulse on the sample that was measured by probe pulses with different polarization orientations $\beta$. (c) Time evolution of the in-plane magnetization angle $\delta\varphi(t)$, the out-of-plane angle $\delta\theta(t)$, and the magnitude $\delta M_s(t)/M_0$; the dotted line depicts the in-plane evolution of the easy-axis position around which the magnetization precesses. (d) Orientation of magnetization at different times after the impact of the pump pulse; the sample plane is represented by the vertical line and the equilibrium position of the easy axis is depicted by the gray spot. From Tesarova, Nemec *et al.*, 2012.

## 2. Optical spin-transfer torque

A direct observation of a nonthermal photocarrier induced spin torque was reported in a pump-and-probe optical experiment in which a coherent spin precession in a (Ga,Mn)As ferromagnetic semiconductor was excited by circularly polarized laser pulses at normal incidence (Nemec *et al.*, 2012). During the pump pulse, the spin-angular momentum of photocarriers generated by the absorbed circularly polarized light is transferred to the collective magnetization of the ferromagnet, as described by Eqs. (4)–(11) and predicted in Fernández-Rossier *et al.* (2003) and Núñez *et al.* (2004).

The time scale of the photoelectron precession due to the exchange field produced by the ferromagnetic Mn moments is $\tau_{ex} \sim 100$ fs in (Ga,Mn)As (Fernández-Rossier *et al.*, 2003; Nemec *et al.*, 2012). The major source of spin decoherence of the photoelectrons in (Ga,Mn)As is the exchange interaction with fluctuating Mn moments. Microscopic calculations of the corresponding relaxation time give a typical scale of tens of picoseconds (Fernández-Rossier *et al.*, 2003). The other factor that limits $\tau_s$ introduced in Eq. (7) is the photoelectron decay time which is also approximately tens of picoseconds, as inferred from reflectivity measurements of the (Ga,Mn)As samples (Nemec *et al.*, 2012). Within the spin lifetime, the photoelectron spins therefore precess many times around the exchange field of ferromagnetic moments. In the corresponding regime of $\tau_s \gg \tau_{ex}$, the steady-state photoelectron spin polarization is given by Eq. (9), i.e., is perpendicular to both the polarization unit vector of the optically injected carrier spins and magnetization, and the optical STT has the form of the adiabatic STT given by Eq. (10), as illustrated in the top inset of Fig. 35. The precession time of holes in (Ga,Mn)As is approximately tens of femtoseconds and the spin lifetime of holes, dominated by the strong spin-orbit coupling, is estimated to be $\sim$1–10 fs (Fernández-Rossier *et al.*, 2003). Since $\tau_s \lesssim \tau_{ex}$ for holes, their contribution in the experiment with circularly polarized pump pulse is better approximated by the weaker torque which has the form of the nonadiabatic STT given by Eq. (11) and can be neglected.

The experimental observation of the magnetization precession in (Ga,Mn)As excited by the optical STT, with the characteristic opposite phases of the oscillations excited by pump pulses of opposite helicities, is shown in the top panel of Fig. 35 (Nemec *et al.*, 2012). Since the period of the magnetization precession (0.4 ns) is much larger than the pump-pulse duration, the action of the optical STT is reflected only in the initial phase and amplitude of the free precession of the magnetization. The decomposition of the magneto-optical signal in Fig. 35 into MCB and MCD induced rotation due to the out-of-plane magnetization and the MLB and MLD induced rotation due to in-plane magnetization shows (Nemec *et al.*, 2012) that the initial tilt of the magnetization is in the out-of-plane direction, as expected from Eq. (10) for the adiabatic STT. The precisely opposite phase of the measured magneto-optical signals triggered by pump pulses with opposite helicities, shown in the top panel of Fig. 35, implies that the optical STT is not accompanied by any polarization-independent excitation mechanism. These were intentionally suppressed in the experiment shown in the top panel of Fig. 35 by negatively biasing an attached piezostressor to the (Ga,Mn)As sample which modified the magnetic anisotropy of the ferromagnetic film. At positive piezovoltage, on the other hand, the polarization-independent mechanisms (Oiwa, Takechi, and Munekata, 2005; Qi *et al.*, 2007, 2009; Takechi *et al.*, 2007; Wang *et al.*, 2007b; Hashimoto, Kobayashi, and Munekata, 2008; Hashimoto and Munekata, 2008; Rozkotová, Nemec, Horodyska *et al.*, 2008; Rozkotová, Němec, Tesařová *et al.*, 2008; Kobayashi *et al.*, 2010) start to act along with the optical STT, as illustrated in the bottom panel of Fig. 35 (Nemec *et al.*, 2012). The polarization-independent optical excitation mechanisms are discussed in the following section.

## 3. Optical spin-orbit torque

In the optical STT reviewed previously, the external source for injecting spin-polarized photocarriers is provided by the circularly polarized light at normal incidence which yields a high degree of out-of-plane spin polarization of injected
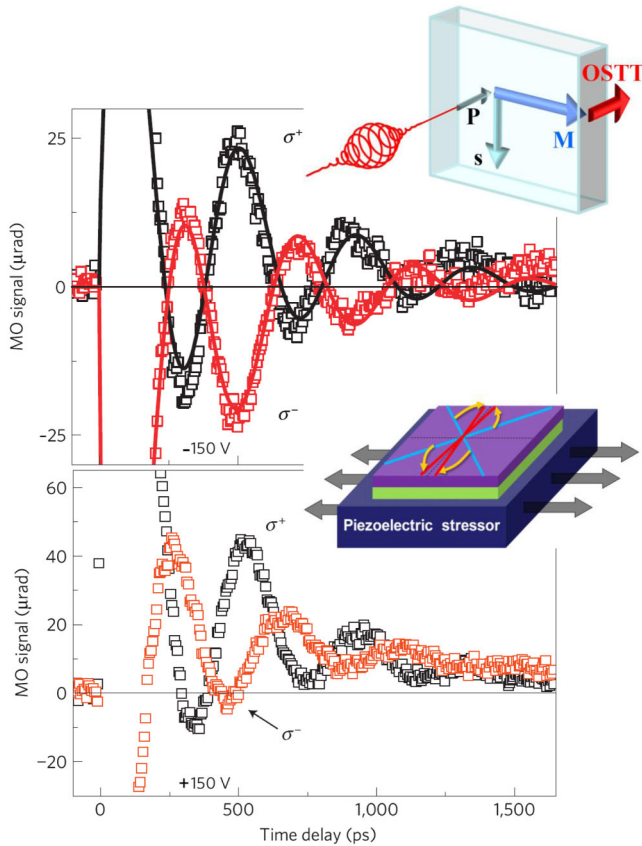
FIG. 35 (color online). Schematic illustration (top inset) of the optical spin-transfer torque induced by the rate $P$ of the photo-carrier spin injection along the light propagation axis $\hat{\mathbf{n}}$ (normal to the sample plane). The steady-state component of the non-equilibrium spin density **s** is oriented in the plane of the sample and perpendicular to the in-plane equilibrium magnetization vector. The (Ga,Mn)As sample is placed on a piezoelectric stressor (lower inset) which allows one to control the magnetic anisotropy *in situ*. Top panel: Precession of the magnetization induced in (Ga,Mn)As by $\sigma^+$ and $\sigma^-$ circularly polarized pump pulses. The points are the measured rotations of the polarization plane of the reflected linearly polarized probe pulse as a function of the time delay between pump-and-probe pulses. The experiment was performed on the (Ga,Mn)As sample attached to a piezostressor at applied bias $U = -150$ V for which the $\sigma^+$ and $\sigma^-$ circularly polarized pump pulses produce signals with opposite sign corresponding to the opposite sign of the optical STT and no polarization-independent ($\sigma^+ + \sigma^-$) signal for this piezovoltage. Bottom panel: Same as the top panel for a piezovoltage $U = +150$ V. Here magnetization dynamics is excited by both the optical STT and a polarization-independent mechanism. Adapted from Nemec *et al.*, 2012.

photocarriers due to the optical selection rules in GaAs. Since large optical STT requires a large spin lifetime of injected carriers, i.e., spin-orbit coupling is detrimental for optical STT, the weakly spin-orbit coupled photoelectrons play a key role in this case. The optical SOT, on the other hand, originates from spin-orbit coupling of nonequilibrium photocarriers excited by polarization-independent pump laser pulses which do not impart angular momentum. Since the effect relies on the strong spin-orbit coupling, the nonequilibrium photoholes

generated in the (Ga,Mn)As valence band are essential for the optical SOT. The physical picture of the optical SOT in (Ga, Mn)As is based on the SOT formalism of Eqs. (12) and (13), and on the following representation of the nonequilibrium steady-state spin polarization of the photoholes (Tesarova *et al.*, 2013): The optically injected photoholes relax toward the hole Fermi energy of the $p$-type (Ga,Mn)As on a short (∼100 fs) time scale (Yildirim *et al.*, 2012) and the excitation and relaxation processes create a nonequilibrium excess hole density in the spin-orbit coupled, exchange-split valence band. The increased number of nonequilibrium occupied hole states, as compared to the equilibrium state in dark, can generate a nonequilibrium spin polarization of holes which is misaligned with the equilibrium orientation of Mn moments. This nonequilibrium photohole polarization persists over the time scale of the hole recombination (∼ps) during which it exerts a torque on the Mn local moments. Approximately, the nonequilibrium photoholes can be represented by a steady state which differs from the equilibrium state in the dark in that the distribution function has a shifted Fermi level corresponding to the extra density of the photoholes. In this approximation, the nonequilibrium spin polarization of holes which is misaligned with the equilibrium orientation of Mn moments, and the corresponding optical SOT, is determined by the hole density dependent magnetocrystalline anisotropy field (Tesarova *et al.*, 2013).

The experimental identification of the optical SOT (Tesarova *et al.*, 2013) required to separate this nonthermal photomagnetic effect from the competing thermal excitation mechanism of magnetization dynamics (Wang *et al.*, 2006; Kirilyuk, Kimel, and Rasing, 2010). The absorption of the pump laser pulse leads to photoinjection of electron-hole pairs. The nonradiative recombination of photoelectrons produces a transient increase of the lattice temperature which builds up on the time scale of ∼10 ps and persists over ∼1000 ps. This results in a quasiequilibrium EA orientation which is tilted from the equilibrium EA. Consequently, Mn moments in (Ga,Mn)As will precess around the quasiequilibrium EA, as schematically illustrated in Fig. 36(a), with a typical precession time of ∼100 ps given by the magnetic anisotropy fields in (Ga,Mn)As. The EA stays in plane and the sense of rotation within the plane of the (Ga,Mn)As film with increasing temperature is uniquely defined by the different temperature dependences of the in-plane cubic and uniaxial anisotropy fields (Zemen *et al.*, 2009; Tesarova *et al.*, 2013). In the notation shown in Fig. 36(c), the change of the in-plane angle $\delta\varphi$ of the magnetization during the thermally excited precession can be only positive.

The optical SOT, illustrated schematically in Fig. 36(b), acts during the laser pulse (with a duration of 200 fs) and fades away within the hole recombination time (∼ps), followed by a free magnetization precession. It causes an impulse tilt of the magnetization which is a signature that allowed us to clearly distinguish the optical SOT from the considerably slower thermal excitation mechanism. Moreover, the initial optical SOT induced tilt of magnetization can yield precession angles that are opposite to the initial tilt of the magnetization dynamics induced by the slower thermal mechanism.

Examples of the direct observation of the thermally governed excitation of magnetization at a lower pump-pulse
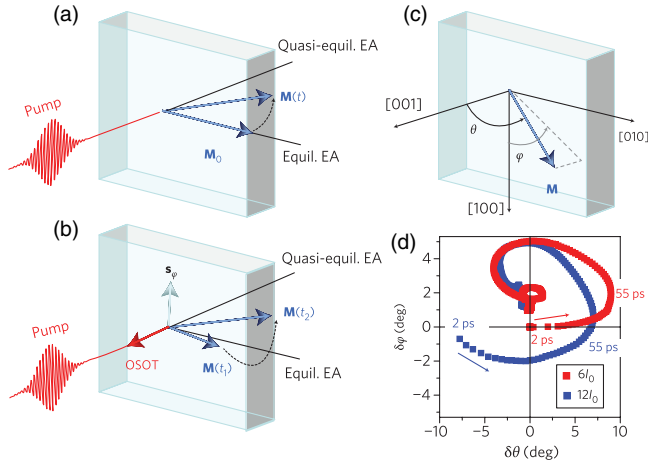
FIG. 36 (color online). (a) Schematic illustration of the thermally excited precession of magnetization $\mathbf{M}(t)$ around the transient quasiequilibrium easy axis (EA). $\mathbf{M}_0$ is the magnetization vector aligned with in-plane equilibrium EA before the pump pulse. (b) Schematic illustration of optical SOT induced by the in-plane transverse component $\mathbf{s}_\varphi$ of the nonequilibrium hole spin polarization. On the time scale of the magnetization precession, optical SOT causes an instantaneous tilt of the magnetization $\mathbf{M}(t_1)$ which allows one to clearly distinguish optical SOT from the considerably slower thermal excitation mechanism. The initial optical SOT induced tilt of magnetization can yield precession angles that are inaccessible in the thermally induced magnetization dynamics. (c) Definition of the coordinate system. (d) Time evolution of the magnetization vector measured in a (Ga,Mn)As material with nominal Mn doping $x = 3\%$. The direction of the time increase is depicted by arrows. Magnetization tilt angles $\delta\varphi$ and $\delta\theta$ are measured with respect to equilibrium EA. From Tesarova *et al.*, 2013.

intensity $6I_0$, where $I_0 = 7 \; \mu\mathrm{J}\,\mathrm{cm}^{-2}$, and of the excitation at a higher intensity $12I_0$ with a strong contribution from the optical SOT are shown in Fig. 36(d) for a 3% doped (Ga,Mn)As sample (Tesarova *et al.*, 2013). The distinct features of the optical SOT observed at pump intensity $12I_0$, namely, the impulse tilt and precession angles inaccessible by thermal excitations seen at the lower intensity $6I_0$, are clearly visible when comparing the two measured magnetization trajectories in Fig. 36(d). We recall that both dynamical magneto-optical signals shown in Fig. 36(d) are independent of the polarization of pump pulses which distinguishes both the slower thermal mechanism and the fast optical SOT mechanism from the optical STT. A complete suppression of the thermal mechanism and magnetization precession induced solely by the optical SOT was achieved by tuning the micromagnetics of the (Ga,Mn)As film *ex situ* by doping or *in situ* by applied magnetic fields (Tesarova *et al.*, 2013).

Magneto-optical pump-and-probe studies in (Ga,Mn)As demonstrated the possibility of studying STT and SOT on the short time scales achievable by the optical techniques. The relativistic optical SOT should be observable in other systems including, e.g., antiferromagnetic semiconductors, which unlike their ferromagnetic counterparts can have magnetic transition temperatures well above room temperature (Jungwirth *et al.*, 2011). It is well established that

magnetocrystalline anisotropies are equally present in spin-orbit coupled antiferromagnets as in ferromagnets and in Sec. III.B.3 we pointed out that the spin-orbit coupling induced anisotropic magnetotransport effects can also be strong in antiferromagnets. The optical SOT belongs to this family of relativistic effects and its exploration in antiferromagnets may open a new direction of optical spin-torque studies beyond the ferromagnetic semiconductor (Ga,Mn)As.

### D. Interaction of spin with heat

In Sec. III.A we outlined the distinction between the basically nonrelativistic Mott spintronic phenomena, such as the GMR or TMR, which depend on relative magnetization orientations in nonuniform magnetic structures, and the relativistic Dirac effects, such as the AHE, AMR, or TAMR, in uniform spin-orbit coupled magnets. In this section we recall that the research of the relativistic spintronics effects in (Ga,Mn)As has led to seminal results not only in magneto-transport and magneto-optical studies but also in the research of magnetothermopower phenomena.

#### 1. Anomalous Nernst effect

In analogy to the AHE, we consider an experimental geometry for detecting the ANE in which the thermal gradient $\nabla T \| \hat{x}$, magnetization $\mathbf{M} \| \hat{z}$, and the Nernst signal is the $M$-antisymmetric electric field $\mathbf{E} \| \hat{y}$. In nonmagnetic systems in zero magnetic field, the charge current density is given by

$$j_x = \sigma_{xx} E_x - \alpha_{xx} \partial_x T, \qquad (17)$$

which for the open circuit geometry ($j_x = 0$) yields

$$E_x = \frac{\alpha_{xx}}{\sigma_{xx}} \partial_x T = S_{xx} \partial_x T, \qquad (18)$$

where $\alpha_{xx}$ is the diagonal Peltier coefficient and $S_{xx}$ is the diagonal Seebeck (thermopower) coefficient. In the presence of the $\hat{z}$-axis magnetization, an off-diagonal Peltier current is generated resulting in the ANE,

$$j_y = -\alpha_{yx} \partial_x T + \sigma_{yx} E_x + \sigma_{xx} E_y, \qquad (19)$$

and for $j_y = 0$,

$$E_y = \frac{1}{\sigma_{xx}} (\alpha_{yx} - \sigma_{yx} S_{xx}) \partial_x T = S_{yx} \partial_x T, \qquad (20)$$

where $\alpha_{xy}$ and $S_{xy}$ are the antisymmetric off-diagonal Peltier and Seebeck coefficients, respectively.

Thermoelectric measurements on Hall bars fabricated in $(\mathrm{Ga, Mn})\mathrm{As}/(\mathrm{Ga, In})\mathrm{As}$ epilayers with perpendicular-to-plane easy axis were performed (Pu *et al.*, 2008) in order to test in a ferromagnet the validity of the Mott relation for the off-diagonal transport coefficients (Wang *et al.*, 2001),

$$\alpha_{yx} = \frac{\pi^2 k_B^2 T}{3e} \left( \frac{\partial \sigma_{yx}}{\partial E} \right)_\mu, \qquad (21)$$

and to experimentally assess the microscopic mechanism of the AHE and ANE in (Ga,Mn)As. In the same devices, the

four thermoelectric coefficients $\rho_{xx}$, $\rho_{xy}$, $S_{xx}$, and $S_{xy}$ were measured which allowed one to directly fit the experimental data by

$$S_{yx} = \frac{\rho_{xy}}{\rho_{xx}}\left(T\frac{\pi^2 k_B^2}{3e}\frac{\lambda'}{\lambda} + (1-n)S_{xx}\right). \tag{22}$$

Equation (22) is obtained by introducing the Mott relation (21) into the expression for $S_{yx}$ from Eq. (20) and by considering a general power-law dependence of the AHE resistivity on the diagonal resistivity,

$$\rho_{xy} = \sigma_{yx}/(\sigma_{xx}^2 + \sigma_{xy}^2) \approx \sigma_{yx}/\sigma_{xx}^2 = \lambda M_z \rho_{xx}^n. \tag{23}$$

Here the proportionality of the AHE to $M_z$ is factored out explicitly in the power-law dependence, $\lambda$ is the remaining scaling factor [$\lambda' = (\partial\lambda/\partial E)_\mu$], and

$$\rho_{xx} = \sigma_{xx}/(\sigma_{xx}^2 + \sigma_{xy}^2) \approx 1/\sigma_{xx}. \tag{24}$$

The intrinsic AHE is characterized by the off-diagonal conductivity $\sigma_{yx}$ which is independent of the scattering lifetime $\tau$, i.e., independent of $\sigma_{xx}$. This corresponds to the above power-law scaling with $n = 2$. On the other hand, for the extrinsic skew-scattering AHE, $\sigma_{yx} \sim \tau \sim \sigma_{xx}$, which corresponds to $n = 1$. The detection of both the AHE and ANE signals in (Ga,Mn)As Hall-bar samples is illustrated in the top panels of Fig. 37. The measured $\rho_{xx}$, $\rho_{xy}$, $S_{xx}$, and $S_{xy}$ could be accurately fitted to Eq. (22) which confirmed the Mott relation between the AHE and ANE in a ferromagnet. Moreover, the inferred values of $n$ from the fitting were close to 2 in all measured samples (see bottom panels of Fig. 37). This confirmed the intrinsic origin of the AHE and ANE in (Ga,Mn)As. Using Eq. (20) we can rewrite Eq. (22) as

$$\alpha_{yx} = \sigma_{yx}\left(T\frac{\pi^2 k_B^2}{3e}\frac{\lambda'}{\lambda} + (2-n)S_{xx}\right), \tag{25}$$

from which we directly obtain that for $n = 2$ the intrinsic, scattering-independent AHE coefficient is accompanied by a scattering-independent ANE coefficient,

$$\sigma_{yx} = \lambda M_z, \quad \alpha_{yx} = \lambda' M_z T\frac{\pi^2 k_B^2}{3e}. \tag{26}$$

### 2. Anisotropic magnetothermopower

Besides ANE, the thermoelectric measurements in (Ga,Mn)As also revealed strong AMT signals, in particular, the spin-caloritronic analog of the noncrystalline AMR (Pu *et al.*, 2006). A noncrystalline AMT as high as 6% was measured in the longitudinal direction obeying the $\cos 2\phi$ dependence as for the noncrystalline longitudinal AMR, where $\phi$ is the angle between magnetization and the applied electrical (thermal) voltage. Simultaneously, the transverse AMT was also observed, as illustrated in Fig. 38, following the $\sin 2\phi$ dependence of the corresponding transverse AMR coefficient. Experiments in (Ga,Mn)As marked a renewed interest in the AMT phenomenon (Ky, 1966) which was subsequently identified in a broad class of magnetic materials, ranging from the strongly spin-orbit coupled uranium pnictides
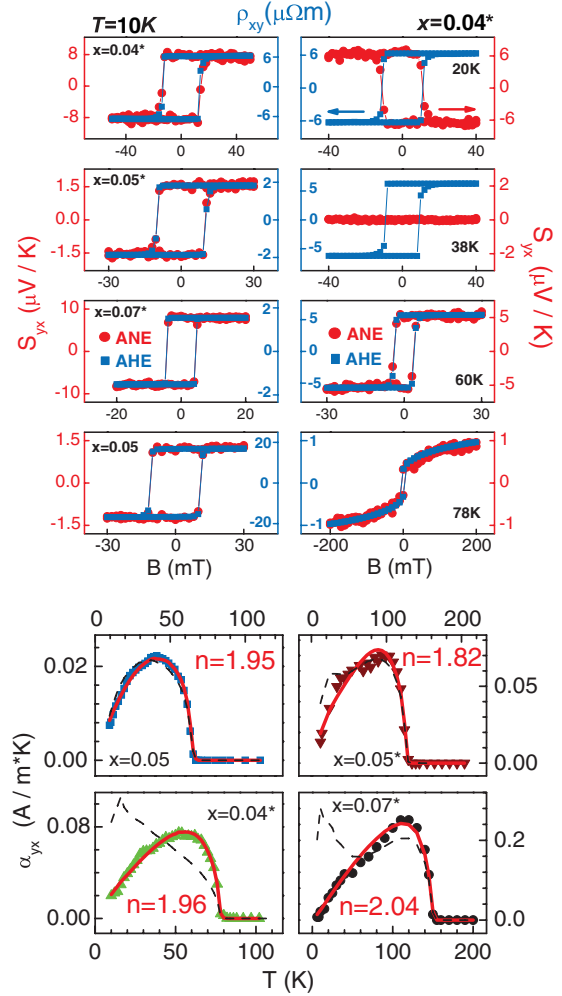


FIG. 37 (color online). Top eight panels: AHE and ANE loops at $T = 10$ K for different samples (left column) and at different temperatures for the 4% annealed sample (right column). In the left column, ANE data of 0.04*, 0.05*, and 0.07* samples were multiplied by $-1$ (* means that the sample was annealed). Bottom four panels: zero-field ANE coefficient. The solid lines are the best fits using Eq. (22) [or equivalently Eq. (25)], and the dashed curves are the best fits with $n = 1$. Adapted from Pu *et al.*, 2008.

(Wisniewski, 2007) to transition-metal based oxides (Tang *et al.*, 2011; Anwar, Lacoste, and Aarts, 2012), and nanowires and thin films of elemental transition-metal ferromagnets (Anwar, Lacoste, and Aarts, 2012; Mitdank *et al.*, 2012).

### 3. Tunneling anisotropic magnetothermopower

Similar to uniform magnetic films, in the Ohmic GMR multilayers electrical and heat transport measurements can be performed in macroscopic samples in the current-parallel-to-plane geometry. This allowed one to observe the GMT effect (Sakurai *et al.*, 1991) shortly after the discovery of the GMR (Baibich *et al.*, 1988; Binasch *et al.*, 1989) in the same type of transition-metal-multilayer samples and to show that switching from parallel to antiparallel magnetization configurations can lead to comparatively large changes in the thermopower (Sakurai *et al.*, 1991).

Magnetothermopower measurements are significantly more challenging in the perpendicular-to-plane geometry of the
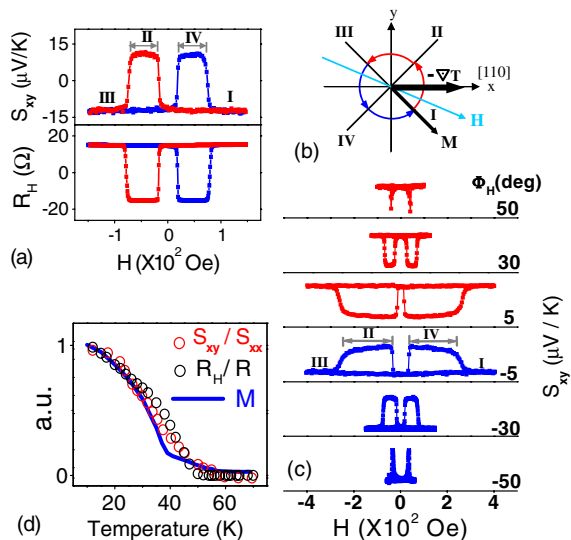
FIG. 38 (color online).   (a) Transverse AMT $S_{x,y}$ and transverse AMR $R_H$ in a 3.9% Mn-doped (Ga,Mn)As. (b) The relative orientation of $-\nabla T$, **M** and magnetic field **H**. The four directions marked as I, II, III, and IV are easy directions of **M**. (c) Angular dependence of the transverse AMT. (d) Comparison of $S_{xy}/S_{xx}$ and $R_H/R$, and sample magnetization $M$ measured by SQUID. Note that we use the terms transverse AMT and transverse AMR instead of the alternative planar Nernst effect and planar Hall effect (Pu *et al.*, 2006) to clearly distinguish the fact that the effects shown here are the symmetric off-diagonal coefficients even in **M**. From Pu *et al.*, 2006.

magnetic tunnel junctions and the TMT effect was observed in transition-metal tunnel devices (Liebing *et al.*, 2011; Walter *et al.*, 2011) more than 15 years after the discovery of the TMR (Miyazaki and Tezuka, 1995; Moodera *et al.*, 1995). Similar to the electrical transport, the magnetothermopower in the tunneling regime is much more closely related to the exchange-split electronic structure of the ferromagnets than in the Ohmic regime of the GMR multilayers and correspondingly can be in principle much stronger in the tunneling devices (Czerner, Bachmann, and Heiliger, 2011; Liebing *et al.*, 2011).

The origin of the TMT effect is schematically illustrated in Fig. 39 (Walter *et al.*, 2011). Unlike electrical conductance of the tunneling device,

$$ G = \frac{e^2}{h} \int T(E)[-\partial_E f(E,\mu,T)]dE, \qquad (27) $$

which in the linear response is governed by the transmission function $T(E)$ multiplied by the derivative of the electron occupation function $\partial_E f(E,\mu,T)$ at temperature $T$ and electrochemical potential $\mu$, the Seebeck coefficient,

$$ S = -\frac{\int T(E)(E-\mu)[-\partial_E f(E,\mu,T)]dE}{eT \int T(E)[-\partial_E f(E,\mu,T)]dE}, \qquad (28) $$

reflects the asymmetry in the energy dependence of the transmission around the chemical potential. As shown in Fig. 39, the Seebeck coefficient is the geometric center of $T(E)[-\partial_E f(E,\mu,T)]$. When this changes from the parallel to
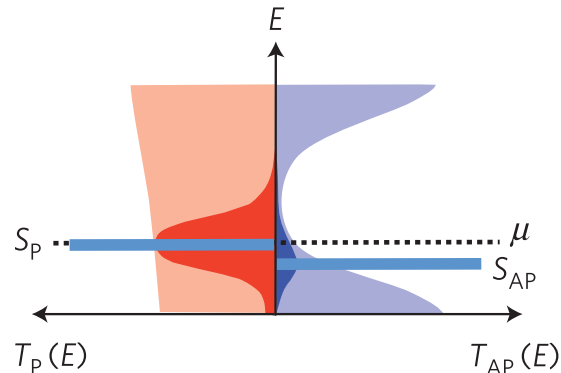


FIG. 39 (color online).   In magnetic tunnel junctions, thermal differences in the electron distributions and strong asymmetry in the spin-dependent tunneling channels are depicted. $T(E)$ is the transmission of the full tunnel junction, for which either the ferromagnetic electrodes can be a highly spin-polarized half-metal or the combination of the barrier and the ferromagnet exhibits half-metallic characteristics. The function $T(E)[-\partial_E f(E,\mu,T)]$ is given in a darker color. The thick line marks the resulting value of the geometric center determining the Seebeck coefficient in the parallel magnetization $S_P$ and antiparallel magnetization $S_{AP}$ of the electrodes. Note that we use the term TMT instead of the alternative magneto-Seebeck effect to distinguish it clearly from the spin-Seebeck effect discussed in Sec. III.D.4. Adapted from Walter *et al.*, 2011.

the antiparallel magnetization configurations the corresponding Seebeck coefficients are different in the two configurations resulting in the TMT.

The relativistic counterpart of the TMT in a tunnel junction with only one magnetic electrode is the TAMT. Observations of the TMT (Liebing *et al.*, 2011; Walter *et al.*, 2011) and TAMT (Naydenova *et al.*, 2011) effects were reported independently and simultaneously and, reminiscent of the discovery of the TAMR (Gould *et al.*, 2004), the TAMT was first identified in a (Ga,Mn)As-based tunnel junction (Naydenova *et al.*, 2011). The experiment was performed while rotating the magnetization in the plane of the (Ga,Mn)As layer, i.e., always perpendicular to the applied temperature gradient across the tunnel junction. As shown in Fig. 40, four
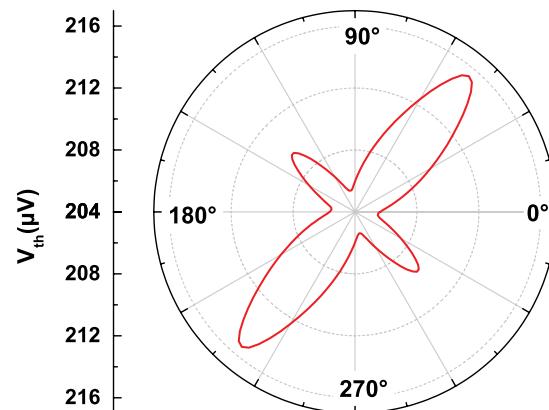


FIG. 40 (color online).   Thermovoltage in a (Ga, Mn)As/$i-$GaAs/GaAs:Si tunnel junction as a function of the magnetization angle. 0 is along the [010] crystal axis. From Naydenova *et al.*, 2011.

equivalent minima close to the [100] and [010] crystal axes and two sets of local maxima were observed. The symmetry of the observed TAMT reflects the competition of in-plane cubic and uniaxial magnetocrystalline anisotropies in the (Ga,Mn) As epilayer. The TAMT phenomenon originates from the changes in the energy dependence of the tunneling density of states when changing the angle of the magnetization with respect to crystal axes, i.e., has the same spin-orbit-coupled band structure origin as magnetocrystalline anisotropies and the TAMR.

## 4. Spin-Seebeck effect

Among the most intriguing spin-caloritronics effects is the spin-Seebeck effect (Uchida *et al.*, 2008, 2010; Jaworski *et al.*,
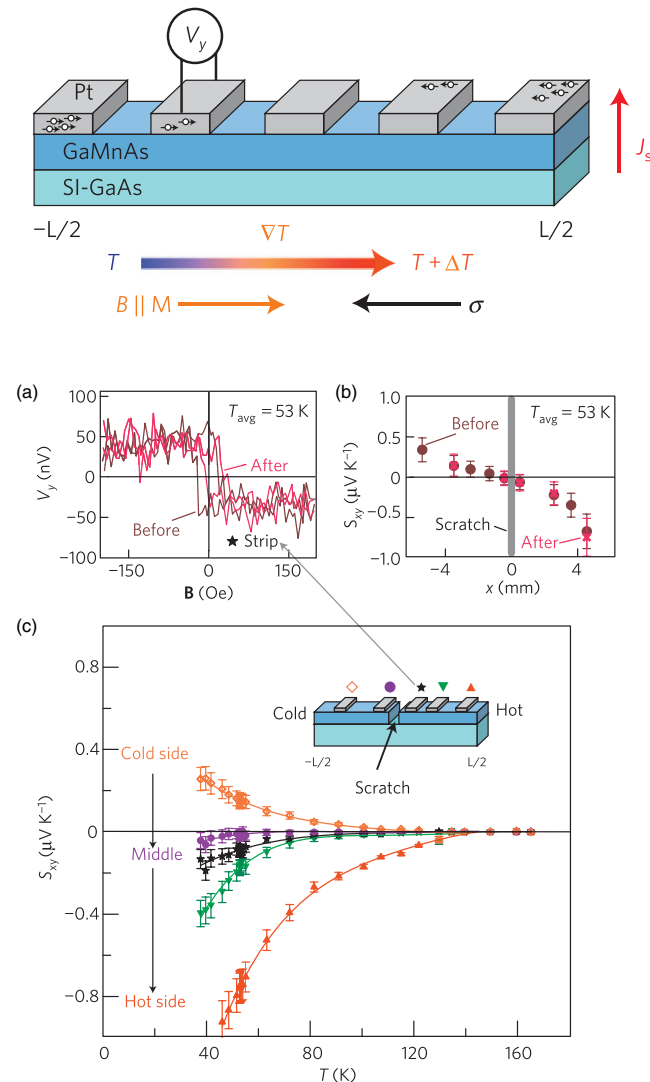


FIG. 41 (color online).    Top panel: Measurement geometry of the spin-Seebeck effect. (a) Transverse voltage $V_y$ as a function of the applied field $B$ from the strip contact 0.3 mm above the scratch (star) with an applied $\Delta T_x$ of 0.63 K. (b) Spatial dependence of the spin-Seebeck coefficient $S_{xy}$ before and after the scratch. The scratched region is indicated by the shaded region. (c) Temperature dependence of $S_{xy}$ after the scratch at various positions along the sample. Adapted from Jaworski *et al.*, 2010.

2010; Sinova, 2010; Bauer, Saitoh, and van Wees, 2012). Instead of directly generating electrical voltages from thermal gradients, as was the case of the above discussed magneto-thermopower effects, in the spin-Seebeck effect it is primarily the difference between spin-up and spin-down chemical potentials $\mu_\uparrow - \mu_\downarrow$, which is induced by the applied thermal voltage in a ferromagnet. An appealing picture was proposed following the first experimental observation of the spin-Seebeck effect in NiFe in which the ferromagnet functions like a thermocouple, but in the spin sector (Uchida *et al.*, 2008). In this picture, instead of two different charge Seebeck coefficients in two metals forming the thermocouple, it is the different carrier scattering and density and the corresponding Seebeck coefficient in the two spin channels which produce the nonzero difference $\mu_\uparrow - \mu_\downarrow$.

In this seminal work and in the subsequent experiments, the SHE in attached nonmagnetic electrodes was employed to convert the difference in spin-dependent chemical potentials into electrical voltages (Uchida *et al.*, 2008, 2010; Jaworski *et al.*, 2010). Specifically, $|\mu_\uparrow - \mu_\downarrow|$ decreases in the non-magnetic electrode from the interface with the ferromagnet along the vertical direction. This results in a vertical spin current in the nonmagnetic electrode which is converted into an in-plane electrical voltage via the SHE.

Experiments in which the transition-metal ferromagnet was replaced with the layer of a metallic (Ga,Mn)As (Jaworski *et al.*, 2010) ruled out the original picture of longitudinal diffusion of electrons in the two spin channels over macroscopic distances in the ferromagnet. As shown in Fig. 41, the same electrical signals were detected on the SHE electrodes after scratching out the conductive (Ga,Mn)As film in the middle of the sample. The nonlocal character of the observed spin-Seebeck effect, i.e., the dependence of the measured SHE voltage on the position of the electrode along the sample, has been extensively discussed since the experiments in (Ga,Mn) As and the parallel observation of the spin-Seebeck effect in a ferromagnetic insulator (Uchida *et al.*, 2010). It has been argued that phonons or magnons in the ferromagnet-substrate structure may be responsible for the nonlocality of the spin-Seebeck effect (Bauer, Saitoh, and van Wees, 2012; Tikhonov, Sinova, and Finkel'stein, 2013).

## IV. SUMMARY

We have reviewed several areas of the rich physics of spintronics phenomena and device concepts explored in the ferromagnetic semiconductor (Ga,Mn)As. The most extensively studied transport characteristics of (Ga,Mn)As are the spin-orbit coupling related magnetoresistance effects. Experiments and calculations in (Ga,Mn)As have provided an unprecedented physical insight into the anomalous Hall effect which prompted a renewed interest and experimental discovery of the spin Hall effect. Anisotropic magnetoresistance phenomena have been identified in (Ga,Mn)As-based tunneling devices and in devices sensing the anisotropy of the chemical potential. Apart from these direct magnetoresistance phenomena, (Ga,Mn)As has become a fruitful model system for exploring the inverse magnetotransport phenomena, i.e., the current-induced spin torques. The studies have provided new insight into spin-transfer torques in domain walls and led

to the discovery of the current-induced spin-orbit torques in uniform magnets. Moreover, optical counterparts of both the nonrelativistic spin-transfer and the relativistic spin-orbit torques have been identified in (Ga,Mn)As, allowing one to study these phenomena on time scales attainable in the optical pump-and-probe experiments. (Ga,Mn)As-based research has also made seminal contributions to the field of spin caloritronics by discovering the Ohmic and tunneling anisotropic thermopower effects and helping to elucidate the origin of the spin-Seebeck effect.

It is likely that (Ga,Mn)As and related ferromagnetic semiconductors will continue to inspire new avenues of magnetic materials and spintronics research in the future. Many studies, in particular, of the relativistic phenomena in (Ga,Mn)As may become directly relevant to room-temperature magnetic systems with strong spin-orbit coupling and may therefore lead to new technological applications, independent of the existing limits of the Curie temperature in the ferromagnetic semiconductors. This knowledge transfer applies to room-temperature magnetic systems which include not only the conventional transition-metal ferromagnets but also, e.g., a class of metal and semiconductor antiferromagnets with high Néel temperatures.

## LIST OF SYMBOLS AND ABBREVIATIONS

| | |
|---|---|
| ABE | Aharonov-Bohm effect |
| AHE | Anomalous Hall effect |
| AMR | Anisotropic magnetoresistance |
| AMT | Anisotropic magnetothermopower |
| ANE | Anomalous Nernst effect |
| CB | Coulomb blockade |
| DOS | Density of states |
| DW | Domain wall |
| FMR | Ferromagnetic resonance |
| GGA | Generalized gradient approximations |
| GMR | Giant magnetoresistance |
| GMT | Giant magnetothermopower |
| LT-MBE | Low-temperature molecular beam epitaxy |
| MCB | Magnetic circular birefringence |
| MCD | Magnetic circular dichroism |
| MLB | Magnetic linear birefringence |
| MLD | Magnetic linear dichroism |
| MRAM | Magnetic random access memory |
| SET | Single-electron transistor |
| SHE | Spin Hall effect |
| SOT | Spin-orbit torque |
| SQUID | Superconducting quantum interference device |
| STT | Spin-transfer torque |
| SWR | Spin-wave resonance |
| TAMR | Tunneling anisotropic magnetoresistance |
| TAMT | Tunneling anisotropic magnetothermopower |
| TBA | Tight-binding approximation |
| TMR | Tunneling magnetoresistance |
| TMT | Tunneling magnetothermopower |
| UCF | Universal conductance fluctuations |
| WB | Walker breakdown |
| WL | Weak localization |

## REFERENCES

Abolfath, M., T. Jungwirth, J. Brum, and A. H. MacDonald, 2001, Phys. Rev. B **63**, 054418.

Acbas, G., M. H. Kim, M. Cukr, V. Novák, M. A. Scarpulla, O. D. Dubon, T. Jungwirth, J. Sinova, and J. Cerne, 2009, Phys. Rev. Lett. **103**, 137201.

Adam, J., N. Vernier, J. Ferre, A. Thiaville, V. Jeudy, A. Lemaitre, L. Thevenard, and G. Faini, 2009, Phys. Rev. B **80**, 193204.

Ando, K., T. Hayashi, M. Tanaka, and A. Twardowski, 1998, J. Appl. Phys. **83**, 6548.

Ando, K., H. Saito, K. C. Agarwal, M. C. Debnath, and V. Zayets, 2008, Phys. Rev. Lett. **100**, 067204.

Anwar, M. S., B. Lacoste, and J. Aarts, 2012, arXiv:1206.1527.

Aprili, M., J. Lesueur, L. Dumoulin, and P. Nédellec, 1997, Solid State Commun. **102**, 41.

Aronov, A. G., and Y. B. Lyanda-Geller, 1989, JETP Lett. **50**, 431.

Baibich, M. N., J. M. Broto, A. Fert, F. N. V. Dau, F. Petroff, P. Eitenne, G. Creuzet, A. Friederich, and J. Chazelas, 1988, Phys. Rev. Lett. **61**, 2472.

Banhart, J., and H. Ebert, 1995, Europhys. Lett. **32**, 517.

Bauer, G. E. W., E. Saitoh, and B. J. van Wees, 2012, Nat. Mater. **11**, 391.

Baumberg, J. J., S. A. Crooker, D. D. Awschalom, N. Samarth, H. Luo, and J. K. Furdyna, 1994, Phys. Rev. B **50**, 7689.

Baxter, D. V., D. Ruzmetov, J. Scherschligt, Y. Sasaki, X. Liu, J. K. Furdyna, and C. H. Mielke, 2002, Phys. Rev. B **65**, 212407.

Berger, L., 1996, Phys. Rev. B **54**, 9353.

Bernand-Mantel, A., P. Seneor, K. Bouzehouane, S. Fusil, C. Deranlot, F. Petroff, and A. Fert, 2009, Nat. Phys. **5**, 920.

Bernevig, B. A., and O. Vafek, 2005, Phys. Rev. B **72**, 033203.

Beschoten, B., P. A. Crowell, I. Malajovich, D. D. Awschalom, F. Matsukura, A. Shen, and H. Ohno, 1999, Phys. Rev. Lett. **83**, 3073.

Bhatt, R. N., P. Wolfle, and T. V. Ramakrishnan, 1985, Phys. Rev. B **32**, 569.

Bhattacharjee, A. K., and C. B. à la Guillaume, 1999, Solid State Commun. **113**, 17.

Bihler, C., W. Schoch, W. Limmer, S. T. B. Goennenwein, and M. S. Brandt, 2009, Phys. Rev. B **79**, 045205.

Binasch, G., P. Grünberg, F. Saurenbach, and W. Zinn, 1989, Phys. Rev. B **39**, 4828.

Birowska, M., C. Sliwa, J. A. Majewski, and T. Dietl, 2012, Phys. Rev. Lett. **108**, 237203.

Blakemore, J. S., W. J. Brown, M. L. Stass, and D. A. Woodbury, 1973, J. Appl. Phys. **44**, 3352.

Bolotin, K. I., F. Kuemmeth, and D. C. Ralph, 2006, Phys. Rev. Lett. **97**, 127202.

Bouzerar, G., 2007, Europhys. Lett. **79**, 57007.

Brey, L., J. Fernández-Rossier, and C. Tejedor, 2004, Phys. Rev. B **70**, 235334.

Brey, L., and G. Gómez-Santos, 2003, Phys. Rev. B **68**, 115206.

Brey, L., C. Tejedor, and J. Fernández-Rossier, 2004, Appl. Phys. Lett. **85**, 1996.

Brown, W. J., and J. S. Blakemore, 1972, J. Appl. Phys. **43**, 2242.

Burch, K. S., D. B. Shrekenhamer, E. J. Singley, J. Stephens, B. L. Sheu, R. K. Kawakami, P. Schiffer, N. Samarth, D. D. Awschalom, and D. N. Basov, 2006, Phys. Rev. Lett. **97**, 087208.

Camilleri, C., F. Teppe, D. Scalbert, Y. G. Semenov, M. Nawrocki, M. Dyakonov, J. Cibert, S. Tatarenko, and T. Wojtowicz, 2001, Phys. Rev. B **64**, 085331.

Campion, R. P., K. W. Edmonds, L. X. Zhao, K. Y. Wang, C. T. Foxon, B. L. Gallagher, and C. R. Staddon, 2003, J. Cryst. Growth **251**, 311.

Chakarvorty, R., W. Lim, X. Liu, M. Kutrowski, L. Tivota, T. Wojtowicz, J. Furdyna, and M. Dobrowolska, 2007, Appl. Phys. Lett. **91**, 171118.

Chantis, A. N., K. D. Belashchenko, E. Y. Tsymbal, and M. van Schilfgaarde, 2007, Phys. Rev. Lett. **98**, 046601.

Chapler, B. C., *et al.*, 2011, Phys. Rev. B **84**, 081203(R).

Chapman, R. A., and W. G. Hutchinson, 1967, Phys. Rev. Lett. **18**, 443.

Chappert, C., A. Fert, and F. N. V. Dau, 2007, Nat. Mater. **6**, 813.

Chen, L., F. Matsukura, and H. Ohno, 2013, Nat. Commun. **4**, 2055.

Chernyshov, A., M. Overby, X. Liu, J. K. Furdyna, Y. Lyanda-Geller, and L. P. Rokhinson, 2009, Nat. Phys. **5**, 656.

Chiba, D., F. Matsukura, and H. Ohno, 2004, Physica (Amsterdam) **21E**, 966.

Chiba, D., F. Matsukura, and H. Ohno, 2006, Appl. Phys. Lett. **89**, 162505.

Chiba, D., T. Ono, F. Matsukura, and H. Ohno, 2013, Appl. Phys. Lett. **103**, 142418.

Chiba, D., Y. Sato, T. Kita, F. Matsukura, and H. Ohno, 2004, Phys. Rev. Lett. **93**, 216602.

Chiba, D., M. Sawicki, Y. Nishitani, Y. Nakatani, F. Matsukura, and H. Ohno, 2008, Nature (London) **455**, 515.

Chiba, D., M. Yamanouchi, F. Matsukura, T. Dietl, and H. Ohno, 2006, Phys. Rev. Lett. **96**, 096602.

Chiba, D., M. Yamanouchi, F. Matsukura, and H. Ohno, 2003, Science **301**, 943.

Chien, L., and C. R. Westgate, 1980, *The Hall Effect and Its Applications* (Plenum, New York).

Chun, S. H., *et al.*, 2007, Phys. Rev. Lett. **98**, 026601.

Ciccarelli, C., L. P. Zarbo, A. C. Irvine, R. P. Campion, B. L. Gallagher, J. Wunderlich, T. Jungwirth, and A. J. Ferguson, 2012, Appl. Phys. Lett. **101**, 122411.

Ciorga, M., A. Einwanger, J. Sadowski, W. Wegscheider, and D. Weiss, 2007, Phys. Status Solidi A **204**, 186.

Collins, M. F., V. J. Minkiewicz, R. Natans, L. Passell, and G. Shirane, 1969, Phys. Rev. **179**, 417.

Crooker, S. A., J. J. Baumberg, F. Flack, N. Samarth, and D. D. Awschalom, 1996, Phys. Rev. Lett. **77**, 2814.

Cubukcu, M., H. J. von Bardeleben, J. L. Cantin, and A. Lemaitre, 2010, Appl. Phys. Lett. **96**, 102502.

Cubukcu, M., H. J. von Bardeleben, K. Khazen, J. L. Cantin, O. Mauguin, L. Largeau, and A. Lemaitre, 2010, Phys. Rev. B **81**, 041202(R).

Curiale, J., A. Lemaitre, C. Ulysse, G. Faini, and V. Jeudy, 2012, Phys. Rev. Lett. **108**, 076604.

Czerner, M., M. Bachmann, and C. Heiliger, 2011, Phys. Rev. B **83**, 132405.

Czeschka, F. D., *et al.*, 2011, Phys. Rev. Lett. **107**, 046601.

de Gennes, P. G., and J. Friedel, 1958, J. Phys. Chem. Solids **4**, 71.

De Ranieri, E., *et al.*, 2008, New J. Phys. **10**, 065003.

De Ranieri, E., *et al.*, 2013, Nat. Mater. **12**, 808.

Deshmukh, M. M., and D. C. Ralph, 2002, Phys. Rev. Lett. **89**, 266803.

Dietl, T., 2003, in *Advances in Solid State Physics*, edited by B. Kramer (Springer, Berlin), p. 413.

Dietl, T., 2007, J. Phys. Condens. Matter **19**, 165204.

Dietl, T., 2008, J. Phys. Soc. Jpn. **77**, 031005.

Dietl, T., A. Haury, and Y. M. d'Aubigne, 1997, Phys. Rev. B **55**, R3347.

Dietl, T., F. Matsukura, H. Ohno, J. Cibert, and D. Ferrand, 2003, in *Recent Trends in Theory of Physical Phenomena in High Magnetic Fields*, edited by I. Vagner (Kluwer, Dordrecht), p. 197.

Dietl, T., and H. Ohno, 2014, Rev. Mod. Phys. **86**, 187.

Dietl, T., H. Ohno, and F. Matsukura, 2001, Phys. Rev. B **63**, 195205.

Dietl, T., H. Ohno, F. Matsukura, J. Cibert, and D. Ferrand, 2000, Science **287**, 1019.

Di Marco, I., P. Thunstrom, M. I. Katsnelson, J. Sadowski, K. Karlsson, S. Lebegue, J. Kanski, and O. Eriksson, 2013, Nat. Commun. **4**, 2645.

Dobrowolska, M., X. Liu, J. K. Furdyna, M. Berciu, K. M. Yu, and W. Walukiewicz, 2012, arXiv:1211.4051.

Dobrowolska, M., K. Tivakornsasithorn, X. Liu, J. K. Furdyna, M. Berciu, K. M. Yu, and W. Walukiewicz, 2012, Nat. Mater. **11**, 444.

Döring, W., 1938, Ann. Phys. (Berlin) **424**, 259.

Dugaev, V. K., P. Bruno, M. Taillefumier, B. Canals, and C. Lacroix, 2005, Phys. Rev. B **71**, 224423.

Dyakonov, M. I., and V. I. Perel, 1971, JETP Lett. **13**, 467.

Ebert, H., A. Vernes, and J. Banhart, 1999, Solid State Commun. **113**, 103.

Edelstein, V. M., 1990, Solid State Commun. **73**, 233.

Edmonds, K. W., K. Y. Wang, R. P. Campion, A. C. Neumann, N. R. S. Farley, B. L. Gallagher, and C. T. Foxon, 2002, Appl. Phys. Lett. **81**, 4991.

Elsen, M., H. Jaffrès, R. Mattana, L. Thevenard, A. Lemaître, and J. M. George, 2007, Phys. Rev. B **76**, 144415.

Endo, M., F. Matsukura, and H. Ohno, 2010, Appl. Phys. Lett. **97**, 222501.

Fang, D., H. Kurebayashi, J. Wunderlich, K. Vyborny, L. P. Zarbo, R. P. Campion, A. Casiraghi, B. L. Gallagher, T. Jungwirth, and A. J. Ferguson, 2011, Nat. Nanotechnol. **6**, 413.

Fang, Z., N. Nagaosa, K. S. Takahashi, A. Asamitsu, R. Mathieu, T. Ogasawara, H. Yamada, M. Kawasaki, Y. Tokura, and K. Terakura, 2003, Science **302**, 92.

Fernández-Rossier, J., A. S. Núñez, M. Abolfath, and A. H. MacDonald, 2003, arXiv:cond-mat/0304492.

Ferreira da Silva, A., I. Pepe, B. E. Sernelius, C. Persson, R. Ahuja, J. P. de Souza, Y. Suzuki, and Y. Yang, 2004, J. Appl. Phys. **95**, 2532.

Fisher, M. E., and J. S. Langer, 1968, Phys. Rev. Lett. **20**, 665.

Gambardella, P., and I. M. Miron, 2011, Phil. Trans. R. Soc. A **369**, 3175.

Ganichev, S. D., E. L. Ivchenko, V. V. Belkov, S. A. Tarasenko, M. Sollinger, D. Weiss, W. Wegscheider, and W. Prettl, 2002, Nature (London) **417**, 153.

Gao, L., X. Jiang, S.-H. Yang, J. D. Burton, E. Y. Tsymbal, and S. S. P. Parkin, 2007, Phys. Rev. Lett. **99**, 226602.

Garate, I., K. Gilmore, M. D. Stiles, and A. H. MacDonald, 2009, Phys. Rev. B **79**, 104416.

Garate, I., and A. H. MacDonald, 2009, Phys. Rev. B **80**, 134403.

Garate, I., J. Sinova, T. Jungwirth, and A. H. MacDonald, 2009, Phys. Rev. B **79**, 155207.

Garello, K., I. M. Miron, C. O. Avci, F. Freimuth, Y. Mokrousov, S. Blugel, S. Auffret, O. Boulle, G. Gaudin, and P. Gambardella, 2013, Nat. Nanotechnol. **8**, 587.

Giddings, A. D., *et al.*, 2005, Phys. Rev. Lett. **94**, 127202.

Gilmore, K., Y. U. Idzerda, and M. D. Stiles, 2008, J. Appl. Phys. **103**, 07D303.

Giraud, R., M. Gryglas, L. Thevenard, A. Lemaître, and G. Faini, 2005, Appl. Phys. Lett. **87**, 242505.

Glunk, M., J. Daeubler, W. Schoch, R. Sauer, and W. Limmer, 2009, Phys. Rev. B **80**, 125204.

Goennenwein, S. T. B., M. Althammer, C. Bihler, A. Brandlmaier, S. Geprägs, M. Opel, W. Schoch, W. Limmer, R. Gross, and M. S. Brandt, 2008, Phys. Status Solidi **2**, 96.

Goennenwein, S. T. B., S. Russo, A. F. Morpurgo, T. M. Klapwijk, W. Van Roy, and J. De Boeck, 2005, Phys. Rev. B **71**, 193306.

Gould, C., C. Rüster, T. Jungwirth, E. Girgis, G. M. Schott, R. Giraud, K. Brunner, G. Schmidt, and L. W. Molenkamp, 2004, Phys. Rev. Lett. **93**, 117203.

Gould, C., *et al.*, 2008, New J. Phys. **10**, 055007.

Gourdon, C., A. Dourlat, V. Jeudy, K. Khazen, H. J. von Bardeleben, L. Thevenard, and A. Lemaître, 2007, Phys. Rev. B **76**, 241301.

Gray, A. X., *et al.*, 2012, Nat. Mater. **11**, 957.

Gregg, J. F., I. Petej, E. Jouguelet, and C. Dennis, 2002, J. Phys. D **35**, R121.

Grigorenko, A. N., K. S. Novoselov, and D. J. Mapps, 2006, arXiv:cond-mat/0611751.

Haas, C., 1970, Crit. Rev. Solid State Sci. **1**, 47.

Haghgoo, S., M. Cubukcu, H. J. von Bardeleben, L. Thevenard, A. Lemaitre, and C. Gourdon, 2010, Phys. Rev. B **82**, 041301(R).

Haldane, F. D. M., 2004, Phys. Rev. Lett. **93**, 206602.

Hall, E. H., 1881, Philos. Mag. **12**, 157.

Hals, K. M. D., A. Brataas, and Y. Tserkovnyak, 2010, Europhys. Lett. **90**, 47 002.

Hals, K. M. D., A. K. Nguyen, and A. Brataas, 2009, Phys. Rev. Lett. **102**, 256601.

Harrison, W. A., 1980, *Electronic Structure and the Properties of Solids* (Freeman, San Francisco).

Hashimoto, Y., S. Kobayashi, and H. Munekata, 2008, Phys. Rev. Lett. **100**, 067202.

Hashimoto, Y., and H. Munekata, 2008, Appl. Phys. Lett. **93**, 202506.

Hayashi, T., Y. Hashimoto, S. Katsumoto, and Y. Iye, 2001, Appl. Phys. Lett. **78**, 1691.

Hayashi, T., M. Tanaka, K. Seto, T. Nishinaga, and K. Ando, 1997, Appl. Phys. Lett. **71**, 1825.

Heinrich, B., Y. Tserkovnyak, G. Woltersdorf, A. Brataas, R. Urban, and G. E. W. Bauer, 2003, Phys. Rev. Lett. **90**, 187601.

Hümpfner, S., M. Sawicki, K. Pappert, J. Wenisch, K. Brunner, C. Gould, G. Schmidt, T. Dietl, and L. W. Molenkamp, 2007, Appl. Phys. Lett. **90**, 102102.

Ingvarsson, S., L. Ritchie, X. Y. Liu, G. Xiao, J. C. Slonczewski, P. L. Trouilloud, and R. H. Koch, 2002, Phys. Rev. B **66**, 214416.

Jaworski, C. M., J. Yang, S. Mack, D. D. Awschalom, J. P. Heremans, and R. C. Myers, 2010, Nat. Mater. **9**, 898.

Joynt, R., 1984, J. Phys. F **14**, 2363.

Julliere, M., 1975, Phys. Lett. **54A**, 225.

Jungwirth, T., M. Abolfath, J. Sinova, J. Kučera, and A. H. MacDonald, 2002, Appl. Phys. Lett. **81**, 4029.

Jungwirth, T., W. A. Atkinson, B. Lee, and A. H. MacDonald, 1999, Phys. Rev. B **59**, 9818.

Jungwirth, T., Q. Niu, and A. H. MacDonald, 2002, Phys. Rev. Lett. **88**, 207208.

Jungwirth, T., J. Sinova, J. Mašek, J. Kučera, and A. H. MacDonald, 2006, Rev. Mod. Phys. **78**, 809.

Jungwirth, T., J. Sinova, K. Y. Wang, K. W. Edmonds, R. P. Campion, B. L. Gallagher, C. T. Foxon, Q. Niu, and A. H. MacDonald, 2003, Appl. Phys. Lett. **83**, 320.

Jungwirth, T., J. Wunderlich, and K. Olejnik, 2012, Nat. Mater. **11**, 382.

Jungwirth, T., *et al.*, 2005, Phys. Rev. B **72**, 165204.

Jungwirth, T., *et al.*, 2006, Phys. Rev. B **73**, 165205.

Jungwirth, T., *et al.*, 2007, Phys. Rev. B **76**, 125206.

Jungwirth, T., *et al.*, 2010, Phys. Rev. Lett. **105**, 227201.

Jungwirth, T., *et al.*, 2011, Phys. Rev. B **83**, 035321.

Kastner, M. A., 1992, Rev. Mod. Phys. **64**, 849.

Kato, Y. K., R. C. Myers, A. C. Gossard, and D. D. Awschalom, 2004, Science **306**, 1910.

Kawabata, A., 1980, Solid State Commun. **34**, 431.

Khazen, K., H. J. von Bardeleben, M. Cubukcu, J. L. Cantin, V. Novák, K. Olejník, M. Cukr, L. Thevenard, and A. Lemaître, 2008, Phys. Rev. B **78**, 195210.

Khmelevskyi, S., K. Palotás, L. Szunyogh, and P. Weinberger, 2003, Phys. Rev. B **68**, 012402.

Kimel, A. V., G. V. Astakhov, A. Kirilyuk, G. M. Schott, G. Karczewski, W. Ossau, G. Schmidt, L. W. Molenkamp, and T. Rasing, 2005, Phys. Rev. Lett. **94**, 227203.

Kirilyuk, A., A. V. Kimel, and T. Rasing, 2010, Rev. Mod. Phys. **82**, 2731.

Kittel, C., 1958, Phys. Rev. **110**, 1295.

Kobayashi, S., K. Suda, J. Aoyama, D. Nakahara, and H. Munekata, 2010, IEEE Trans. Magn. **46**, 2470.

Kodzuka, M., T. Ohkubo, K. Hono, F. Matsukura, and H. Ohno, 2009, Ultramicroscopy **109**, 644.

Komori, T., T. Ishikawa, T. Kuroda, J. Yoshino, F. Minami, and S. Koshihara, 2003, Phys. Rev. B **67**, 115203.

König, J., T. Jungwirth, and A. H. MacDonald, 2001, Phys. Rev. B **64**, 184423.

Kopecky, M., J. Kub, F. Maca, J. Masek, O. Pacherova, A. W. Rushforth, B. L. Gallagher, R. P. Campion, V. Novak, and T. Jungwirth, 2011, Phys. Rev. B **83**, 235324.

Koshihara, S., A. Oiwa, M. Hirasawa, S. Katsumoto, Y. Iye, C. Urano, H. Takagi, and H. Munekata, 1997, Phys. Rev. Lett. **78**, 4617.

Kötzler, J., and W. Gil, 2005, Phys. Rev. B **72**, 060412(R).

Kovacs, A., J. Sadowski, T. Kasama, J. Domagala, R. Mathieu, T. Dietl, and R. E. Dunin-Borkowski, 2011, J. Appl. Phys. **109**, 083546.

Kramer, B., and A. MacKinnon, 1993, Rep. Prog. Phys. **56**, 1469.

Kurebayashi, H., *et al.*, 2014, Nat. Nanotechnol. **9**, 211.

Kuroiwa, T., T. Yasuda, F. Matsukura, A. Shen, Y. Ohno, Y. Segawa, and H. Ohno, 1998, Electron. Lett. **34**, 190.

Ky, V. D., 1966, Phys. Status Solidi **17**, K207.

Lang, R., A. Winter, H. Pascher, H. Krenn, X. Liu, and J. K. Furdyna, 2005, Phys. Rev. B **72**, 024430.

Lee, P. A., and T. V. Ramakrishnan, 1985, Rev. Mod. Phys. **57**, 287.

Lee, P. A., A. D. Stone, and H. Fukuyama, 1987, Phys. Rev. B **35**, 1039.

Lee, W.-L., S. Watauchi, V. L. Miller, R. J. Cava, and N. P. Ong, 2004, Science **303**, 1647.

Liebing, N., S. Serrano-Guisan, K. Rott, G. Reiss, J. Langer, B. Ocker, and H. W. Schumacher, 2011, Phys. Rev. Lett. **107**, 177201.

Likharev, K. K., 1999, Proc. IEEE **87**, 606.

Limmer, W., M. Glunk, J. Daeubler, T. Hummel, W. Schoch, R. Sauer, C. Bihler, H. Huebl, M. S. Brandt, and S. T. B. Goennenwein, 2006, Phys. Rev. B **74**, 205205.

Linnarsson, M., E. Janzén, B. Monemar, M. Kleverman, and A. Thilderkvist, 1997, Phys. Rev. B **55**, 6938.

Liu, L., C. Pai, Y. Li, H. W. Tseng, D. C. Ralph, and R. A. Buhrman, 2012, Science **336**, 555.

Liu, X., Y. Y. Zhou, and J. K. Furdyna, 2007, Phys. Rev. B **75**, 195220.

Luttinger, J. M., 1958, Phys. Rev. **112**, 739.

Máca, F., and J. Mašek, 2002, Phys. Rev. B **65**, 235209.

MacDonald, A. H., P. Schiffer, and N. Samarth, 2005, Nat. Mater. **4**, 195.

Madelung, O., U. Rössler, and M. Schulz, 2003, *Impurities and Defects in Group IV Elements, IV–IV and III–V Compounds. Part b: Group IV–IV and III–V Compounds*, Vol. 41A2b, Landolt-Börnstein Group III Condensed Matter (Springer-Verlag, Berlin).

Manchon, A., N. Ryzhanova, M. Chschiev, A. Vedyayev, and B. Dieny, 2008, J. Phys. Condens. Matter **20**, 145208.

Manchon, A., and S. Zhang, 2008, Phys. Rev. B **78**, 212405.

Manchon, A., and S. Zhang, 2009, Phys. Rev. B **79**, 094422.

Mankovsky, S., S. Polesya, S. Bornemann, J. Minár, F. Hoffmann, C. H. Back, and H. Ebert, 2011, Phys. Rev. B **84**, 201201.

Marder, M. P., 2000, *Condensed Matter Physics* (Wiley, New York), eprint supplementary material by author.

Marti, X., *et al.*, 2013, arXiv:1303.4704.

Marti, X. *et al.*, 2014, Nat. Mater. **13**, 367.

Mašek, J., *et al.*, 2010, Phys. Rev. Lett. **105**, 227202.

Matsukura, F., H. Ohno, and T. Dietl, 2002, in *Handbook of Magnetic Materials*, edited by K. H. J. Buschow (Elsevier, Amsterdam), Vol. 14, p. 1.

Matsukura, F., H. Ohno, A. Shen, and Y. Sugawara, 1998, Phys. Rev. B **57**, R2037.

Matsukura, F., M. Sawicki, T. Dietl, D. Chiba, and H. Ohno, 2004, Physica (Amsterdam) **21E**, 1032.

Mattana, R., *et al.*, 2005, Phys. Rev. B **71**, 075206.

McGuire, T., and R. Potter, 1975, IEEE Trans. Magn. **11**, 1018.

Metaxas, P. J., J. P. Jamet, A. Mougin, M. Cormier, J. Ferre, V. Baltz, B. Rodmacq, B. Dieny, and R. L. Stamps, 2007, Phys. Rev. Lett. **99**, 217208.

Mikheev, E., I. Stolichnov, Z. Huang, A. W. Rushforth, J. A. Haigh, R. P. Campion, K. W. Edmonds, B. L. Gallagher, and N. Setter, 2012, Appl. Phys. Lett. **100**, 262906.

Miron, I. M., K. Garello, G. Gaudin, P. Zermatten, M. V. Costache, S. Auffret, S. Bandiera, B. Rodmacq, A. Schuhl, and P. Gambardella, 2011, Nature (London) **476**, 189.

Miron, I. M., G. Gaudin, S. Auffret, B. Rodmacq, A. Schuhl, S. Pizzini, J. Vogel, and P. Gambardella, 2010, Nat. Mater. **9**, 230.

Mitdank, R., M. Handwerg, C. Steinweg, W. Tollner, M. Daub, K. Nielsch, and S. F. Fischer, 2012, J. Appl. Phys. **111**, 104320.

Miyazaki, T., and N. Tezuka, 1995, J. Magn. Magn. Mater. **139**, L231.

Mizukami, S., Y. Ando, and T. Miyazaki, 2001, Jpn. J. Appl. Phys. **40**, 580.

Moodera, J. S., L. R. Kinder, T. M. Wong, and R. Meservey, 1995, Phys. Rev. Lett. **74**, 3273.

Moore, G. P., J. Ferré, A. Mougin, M. Moreno, and L. Däweritz, 2003, J. Appl. Phys. **94**, 4530.

Moser, J., A. Matos-Abiague, D. Schuh, W. Wegscheider, J. Fabian, and D. Weiss, 2007, Phys. Rev. Lett. **99**, 056601.

Mott, N. F., 1929, Proc. R. Soc. A **124**, 425.

Mott, N. F., 1936, Proc. R. Soc. A **153**, 699.

Mott, N. F., 1964, Adv. Phys. **13**, 325.

Mougin, A., M. Cormier, J. P. Adam, P. J. Metaxas, and J. Ferre, 2007, Europhys. Lett. **78**, 57 007.

Munekata, H., T. Abe, S. Koshihara, A. Oiwa, M. Hirasawa, S. Katsumoto, Y. Iye, C. Urano, and H. Takagi, 1997, Appl. Phys. Lett. **81**, 4862.

Munekata, H., A. Zaslavsky, P. Fumagalli, and R. J. Gambino, 1993, Appl. Phys. Lett. **63**, 2929.

Murakami, S., N. Nagaosa, and S.-C. Zhang, 2003, Science **301**, 1348.

Myers, R. C., B. L. Sheu, A. W. Jackson, A. C. Gossard, P. Schiffer, N. Samarth, and D. D. Awschalom, 2006, Phys. Rev. B **74**, 155203.

Nagaev, E. L., 1998, Phys. Rev. B **58**, 816.

Nagaosa, N., J. Sinova, S. Onoda, A. H. MacDonald, and N. P. Ong, 2010, Rev. Mod. Phys. **82**, 1539.

Naydenova, T., P. Durrenfeld, K. Tavakoli, N. Pegard, L. Ebel, K. Pappert, K. Brunner, C. Gould, and L. W. Molenkamp, 2011, Phys. Rev. Lett. **107**, 197201.

Nemec, P., *et al.*, 2012, Nat. Phys. **8**, 411.

Nemec, P., *et al.*, 2013, Nat. Commun. **4**, 1422.

Neumaier, D., K. Wagner, S. Geissler, U. Wurstbauer, J. Sadowski, W. Wegscheider, and D. Weiss, 2007, Phys. Rev. Lett. **99**, 116803.

Niazi, T., M. Cormier, D. Lucot, L. Largeau, V. Jeudy, J. Cibert, and A. Lemaitre, 2013, Appl. Phys. Lett. **102**, 122403.

Novák, V., *et al.*, 2008, Phys. Rev. Lett. **101**, 077201.

Núñez, A. S., J. Fernández-Rossier, M. Abolfath, and A. H. MacDonald, 2004, J. Magn. Magn. Mater. **272–276**, 1913.

Ohno, H., 1998, Science **281**, 951.

Ohno, H., 1999, J. Magn. Magn. Mater. **200**, 110.

Ohno, H., D. Chiba, F. Matsukura, T. Omiya, E. Abe, T. Dietl, Y. Ohno, and K. Ohtani, 2000, Nature (London) **408**, 944.

Ohno, H., and T. Dietl, 2008, J. Magn. Magn. Mater. **320**, 1293.

Ohno, H., H. Munekata, T. Penney, S. von Molnár, and L. L. Chang, 1992, Phys. Rev. Lett. **68**, 2664.

Ohno, H., A. Shen, F. Matsukura, A. Oiwa, A. Endo, S. Katsumoto, and Y. Iye, 1996, Appl. Phys. Lett. **69**, 363.

Ohno, Y., D. K. Young, B. Beschoten, F. Matsukura, H. Ohno, and D. D. Awschalom, 1999, Nature (London) **402**, 790.

Ohya, S., P. N. Hai, Y. Mizuno, and M. Tanaka, 2007, Phys. Rev. B **75**, 155328.

Oiwa, A., H. Takechi, and H. Munekata, 2005, J. Supercond. Nov. Magn. **18**, 9.

Okabayashi, J., A. Kimura, O. Rader, T. Mizokawa, A. Fujimori, T. Hayashi, and M. Tanaka, 1998, Phys. Rev. B **58**, R4211.

Olejník, K., M. H. S. Owen, V. Novák, J. Mašek, A. C. Irvine, J. Wunderlich, and T. Jungwirth, 2008, Phys. Rev. B **78**, 054403.

Omiya, T., F. Matsukura, T. Dietl, Y. Ohno, T. Sakon, M. Motokawa, and H. Ohno, 2000, Physica (Amsterdam) **7E**, 976.

Ono, K., H. Shimada, and Y. Ootuka, 1997, J. Phys. Soc. Jpn. **66**, 1261.

Onoda, M., and N. Nagaosa, 2002, J. Phys. Soc. Jpn. **71**, 19.

Overby, M., A. Chernyshov, L. P. Rokhinson, X. Liu, and J. K. Furdyna, 2008, Appl. Phys. Lett. **92**, 192501.

Owen, M. H. S., *et al.*, 2009, New J. Phys. **11**, 023008.

Paalanen, M. A., and R. N. Bhatt, 1991, Physica (Amsterdam) **169B**, 223.

Pappert, K., S. Hümpfner, C. Gould, J. Wenisch, K. Brunner, G. Schmidt, and L. W. Molenkamp, 2007, Nat. Phys. **3**, 573.

Pappert, K., M. J. Schmidt, S. Hümpfner, C. Rüster, G. M. Schott, K. Brunner, C. Gould, G. Schmidt, and L. W. Molenkamp, 2006, Phys. Rev. Lett. **97**, 186402.

Park, B. G., J. Wunderlich, D. A. Williams, S. J. Joo, K. Y. Jung, K. H. Shin, K. Olejník, A. B. Shick, and T. Jungwirth, 2008, Phys. Rev. Lett. **100**, 087204.

Park, B. G., *et al.*, 2011, Nat. Mater. **10**, 347.

Potashnik, S. J., K. C. Ku, R. Mahendiran, S. H. Chun, R. F. Wang, N. Samarth, and P. Schiffer, 2002, Phys. Rev. B **66**, 012408.

Potter, R. I., 1974, Phys. Rev. B **10**, 4626.

Pu, Y., D. Chiba, F. Matsukura, H. Ohno, and J. Shi, 2008, Phys. Rev. Lett. **101**, 117208.

Pu, Y., E. Johnston-Halperin, D. D. Awschalom, and J. Shi, 2006, Phys. Rev. Lett. **97**, 036601.

Qi, J., Y. Xu, A. Steigerwald, X. Liu, J. K. Furdyna, I. E. Perakis, and N. H. Tolk, 2009, Phys. Rev. B **79**, 085304.

Qi, J., Y. Xu, N. H. Tolk, X. Liu, J. K. Furdyna, and I. E. Perakis, 2007, Appl. Phys. Lett. **91**, 112506.

Ralph, D. C., and M. D. Stiles, 2008, J. Magn. Magn. Mater. **320**, 1190.

Rantschler, J. O., R. D. McMichael, A. Castillo, A. J. Shapiro, W. F. Egelhoff, Jr., B. B. Maranville, D. Pulugurtha, A. P. Chen, and L. M. Connors, 2007, J. Appl. Phys. **101**, 033911.

Rappoport, T. G., P. Redliński, X. Liu, G. Zaránd, J. K. Furdyna, and B. Jankó, 2004, Phys. Rev. B **69**, 125213.

Riester, S. W. E., I. Stolichnov, H. J. Trodahl, N. Setter, A. W. Rushforth, K. W. Edmonds, R. P. Campion, C. T. Foxon, B. L. Gallagher, and T. Jungwirth, 2009, Appl. Phys. Lett. **94**, 063504.

Rokhinson, L. P., Y. Lyanda-Geller, Z. Ge, S. Shen, X. Liu, M. Dobrowolska, and J. K. Furdyna, 2007, Phys. Rev. B **76**, 161201.

Roy, P. E., and J. Wunderlich, 2011, Appl. Phys. Lett. **99**, 122504.

Rozkotová, E., P. Nemec, P. Horodyska, D. Sprinzl, F. Trojanek, P. Maly, V. Novak, K. Olejnik, M. Cukr, and T. Jungwirth, 2008, Appl. Phys. Lett. **92**, 122507.

Rozkotová, E., P. Němec, N. Tesařová, P. Malý, V. Novák, K. Olejník, M. Cukr, and T. Jungwirth, 2008, Appl. Phys. Lett. **93**, 232505.

Rushforth, A. W., N. R. S. Farley, R. P. Campion, K. W. Edmonds, C. R. Staddon, C. T. Foxon, B. L. Gallagher, and K. M. Yu, 2008, Phys. Rev. B **78**, 085209.

Rushforth, A. W., M. Wang, N. R. S. Farley, R. C. Campion, K. W. Edmonds, C. R. Staddon, C. T. Foxon, and B. L. Gallagher, 2008, J. Appl. Phys. **104**, 073908.

Rushforth, A. W., *et al.*, 2007, Phys. Rev. Lett. **99**, 147207.

Rushforth, A. W., *et al.*, 2008, Phys. Rev. B **78**, 085314.

Rüster, C., T. Borzenko, C. Gould, G. Schmidt, L. W. Molenkamp, X. Liu, T. J. Wojtowicz, J. K. Furdyna, Z. G. Yu, and M. E. Flatté, 2003, Phys. Rev. Lett. **91**, 216602.

Rüster, C., C. Gould, T. Jungwirth, E. Girgis, G. M. Schott, R. Giraud, K. Brunner, G. Schmidt, and L. W. Molenkamp, 2005, J. Appl. Phys. **97**, 10C506.

Rüster, C., C. Gould, T. Jungwirth, J. Sinova, G. M. Schott, R. Giraud, K. Brunner, G. Schmidt, and L. W. Molenkamp, 2005, Phys. Rev. Lett. **94**, 027203.

Ruzmetov, D., J. Scherschligt, D. V. Baxter, T. Wojtowicz, X. Liu, Y. Sasaki, J. K. Furdyna, K. M. Yu, and W. Walukiewicz, 2004, Phys. Rev. B **69**, 155207.

Saffarzadeh, A., and A. A. Shokri, 2006, J. Magn. Magn. Mater. **305**, 141.

Saito, H., S. Yuasa, and K. Ando, 2005, Phys. Rev. Lett. **95**, 086604.

Saitoh, E., M. Ueda, H. Miyajima, and G. Tatara, 2006, Appl. Phys. Lett. **88**, 182509.

Sakurai, J., M. Horie, S. Araki, H. Yamamoto, and T. Shinjo, 1991, J. Phys. Soc. Jpn. **60**, 2522.

Sankowski, P., P. Kacman, J. A. Majewski, and T. Dietl, 2007, Phys. Rev. B **75**, 045306.

Sato, K., *et al.*, 2010, Rev. Mod. Phys. **82**, 1633.

Sawicki, M., D. Chiba, A. Korbecka, Y. Nishitani, J. A. Majewski, F. Matsukura, T. Dietl, and H. Ohno, 2010, Nat. Phys. **6**, 22.

Sawicki, M., *et al.*, 2005, Phys. Rev. B **71**, 121302.

Schlapps, M., M. Doeppe, K. Wagner, M. Reinwald, W. Wegscheider, and D. Weiss, 2006, Phys. Status Solidi A **203**, 3597.

Schlapps, M., T. Lermer, S. Geissler, D. Neumaier, J. Sadowski, D. Schuh, W. Wegscheider, and D. Weiss, 2009, Phys. Rev. B **80**, 125330.

Schneider, J., U. Kaufmann, W. Wilkening, M. Baeumler, and F. Köhl, 1987, Phys. Rev. Lett. **59**, 240.

Shacklette, L. W., 1974, Phys. Rev. B **9**, 3789.

Shen, A., H. Ohno, F. Matsukura, Y. Sugawara, N. Akiba, T. Kuroiwa, A. Oiwa, A. Endo, S. Katsumoto, and Y. Iye, 1997, J. Cryst. Growth **175**–**176**, 1069.

Shick, A. B., S. Khmelevskyi, O. N. Mryasov, J. Wunderlich, and T. Jungwirth, 2010, Phys. Rev. B **81**, 212409.

Shick, A. B., F. Máca, J. Mašek, and T. Jungwirth, 2006, Phys. Rev. B **73**, 024418.

Shimizu, H., T. Hayashi, T. Nishinaga, and M. Tanaka, 1999, Appl. Phys. Lett. **74**, 398.

Shklovskii, B. I., and A. L. Efros, 1984, *Electronic Propreties of Doped Semiconductors* (Spinger-Verlag, New York).

Silver, M., W. Batty, A. Ghiti, and E. P. O'Reilly, 1992, Phys. Rev. B **46**, 6781.

Sinitsyn, N. A., Q. Niu, J. Sinova, and K. Nomura, 2005, Phys. Rev. B **72**, 045346.

Sinova, J., 2010, Nat. Mater. **9**, 880.

Sinova, J., D. Culcer, Q. Niu, N. A. Sinitsyn, T. Jungwirth, and A. H. MacDonald, 2004, Phys. Rev. Lett. **92**, 126603.

Sinova, J., T. Jungwirth, and J. Černe, 2004, Int. J. Mod. Phys. B **18**, 1083.

Sinova, J., T. Jungwirth, X. Liu, Y. Sasaki, J. K. Furdyna, W. A. Atkinson, and A. H. MacDonald, 2004, Phys. Rev. B **69**, 085209.

Sinova, J., T. Jungwirth, S. R. E. Yang, J. Kučera, and A. H. MacDonald, 2002, Phys. Rev. B **66**, 041202.

Slonczewski, J. C., 1996, J. Magn. Magn. Mater. **159**, L1.

Smit, J., 1951, Physica (Utrecht) **17**, 612.

Stefanowicz, W., C. Sliwa, P. Aleshkevych, T. Dietl, M. Doppe, U. Wurstbauer, W. Wegscheider, D. Weiss, and M. Sawicki, 2010, Phys. Rev. B **81**, 155203.

Stolichnov, I., S. W. E. Riester, H. J. Trodahl, N. Setter, A. W. Rushforth, K. W. Edmonds, R. P. Campion, C. T. Foxon, B. L. Gallagher, and T. Jungwirth, 2008, Nat. Mater. **7**, 464.

Strange, P., 1998, *Relativistic Quantum Mechanics* (Cambridge University Press, Cambridge, England).

Szczytko, J., W. Mac, A. Twardowski, F. Matsukura, and H. Ohno, 1999, Phys. Rev. B **59**, 12935.

Takechi, H., A. Oiwa, K. Nomura, T. Kondo, and H. Munekata, 2007, Phys. Status Solidi C **3**, 4267.

Tanaka, M., and Y. Higo, 2001, Phys. Rev. Lett. **87**, 026602.

Tanaka, T., H. Kontani, M. Naito, T. Naito, D. S. Hirashima, K. Yamada, and J. Inoue, 2008, Phys. Rev. B **77**, 165117.

Tang, G. D., H. H. Guo, T. Yang, D. W. Zhang, X. N. Xu, L. Y. Wang, Z. H. Wang, H. H. Wen, Z. D. Zhang, and Y. W. Du, 2011, Appl. Phys. Lett. **98**, 202109.

Tang, H. X., R. K. Kawakami, D. D. Awschalom, and M. L. Roukes, 2003, Phys. Rev. Lett. **90**, 107201.

Tang, J.-M., and M. E. Flatté, 2008, Phys. Rev. Lett. **101**, 157203.

Tatara, G., N. Nakabayashi, and K. J. Lee, 2013, Phys. Rev. B **87**, 054403.

Tesarova, N., P. Nemec, E. Rozkotova, J. Subrt, H. Reichlova, D. Butkovicova, F. Trojanek, P. Maly, V. Novak, and T. Jungwirth, 2012, Appl. Phys. Lett. **100**, 102403.

Tesarova, N., P. Nemec, E. Rozkotova, J. Zemen, F. Trojanek, K. Olejnik, V. Novak, P. Maly, and T. Jungwirth, 2013, Nat. Photonics **7**, 492.

Tesarova, N., J. Subrt, P. Maly, P. Nemec, C. T. Ellis, A. Mukherjee, and J. Cerne, 2012, Rev. Sci. Instrum. **83**, 123108.

Tesarova, N., *et al.*, 2014, Phys. Rev. B **89**, 085203.

Thiaville, A., Y. Nakatani, J. Miltat, and Y. Suzuki, 2005, Europhys. Lett. **69**, 990.

Thomson, W., 1857, Proc. R. Soc. London **8**, 546.

Tikhonov, K. S., J. Sinova, and A. M. Finkeľstein, 2013, Nat. Commun. **4**, 1945.

Tran, M., J. Peiro, H. Jaffres, J. M. George, O. Mauguin, L. Largeau, and A. Lemaître, 2009, Appl. Phys. Lett. **95**, 172101.

Trushin, M., K. Vyborny, P. Moraczewski, A. A. Kovalev, J. Schliemann, and T. Jungwirth, 2009, Phys. Rev. B **80**, 134405.

Tserkovnyak, Y., A. Brataas, G. E. W. Bauer, and B. I. Halperin, 2005, Rev. Mod. Phys. **77**, 1375.

Tsukagoshi, K., B. W. Alphenaar, and K. Nakazato, 1998, Appl. Phys. Lett. **73**, 2515.

Uchida, K., S. Takahashi, K. Harii, J. Ieda, W. Koshibae, K. Ando, S. Maekawa, and E. Saitoh, 2008, Nature (London) **455**, 778.

Uchida, K., *et al.*, 2010, Nat. Mater. **9**, 894.

Uemura, T., Y. Imai, M. Harada, K. Matsuda, and M. Yamamoto, 2009, Appl. Phys. Lett. **94**, 182502.

Valenzuela, S. O., and M. Tinkham, 2006, Nature (London) **442**, 176.

van der Molen, S. J., N. Tombros, and B. J. van Wees, 2006, Phys. Rev. B **73**, 220406.

Van Esch, A., L. Van Bockstal, J. De Boeck, G. Verbanck, A. S. Van Steenbergen, P. J. Wellmann, B. Grietens, R. B. F. Herlach, and G. Borghs, 1997, Phys. Rev. B **56**, 13103.

van Gorkom, R. P., J. Caro, T. M. Klapwijk, and S. Radelaar, 2001, Phys. Rev. B **63**, 134432.

Vanhaverbeke, A., and M. Viret, 2007, Phys. Rev. B **75**, 024411.

Vila, L., R. Giraud, L. Thevenard, A. Lemaître, F. Pierre, J. Dufouleur, D. Mailly, B. Barbara, and G. Faini, 2007, Phys. Rev. Lett. **98**, 027204.

Viret, M., M. Gabureac, F. Ott, C. Fermon, C. Barreteau, and R. Guirado-Lopez, 2006, Eur. Phys. J. B **51**, 1.

Vyborny, K., J. Kucera, J. Sinova, A. W. Rushforth, B. L. Gallagher, and T. Jungwirth, 2009, Phys. Rev. B **80**, 165204.

Wagner, K., D. Neumaier, M. Reinwald, W. Wegscheider, and D. Weiss, 2006, Phys. Rev. Lett. **97**, 056803.

Walowski, J., M. Djordjevic Kaufmann, B. Lenk, C. Hamann, J. McCord, and M. Munzenberg, 2008, J. Phys. D **41**, 164016.

Walter, M., *et al.*, 2011, Nat. Mater. **10**, 742.

Wang, D. M., Y. H. Ren, X. Liu, J. K. Furdyna, M. Grimsditch, and R. Merlin, 2007a, Phys. Rev. B **75**, 233308.

Wang, D. M., Y. H. Ren, X. Liu, J. K. Furdyna, M. Grimsditch, and R. Merlin, 2007b, Phys. Rev. B **75**, 233308.

Wang, J., C. Sun, Y. Hashimoto, J. Kono, G. A. Khodaparast, L. Cywinski, L. J. Sham, G. D. Sanders, C. J. Stanton, and H. Munekata, 2006, J. Phys. Condens. Matter **18**, R501.

Wang, K. Y., K. W. Edmonds, R. P. Campion, L. X. Zhao, C. T. Foxon, and B. L. Gallagher, 2005, Phys. Rev. B **72**, 085201.

Wang, K. Y., M. Sawicki, K. W. Edmonds, R. P. Campion, S. Maat, C. T. Foxon, B. L. Gallagher, and T. Dietl, 2005, Phys. Rev. Lett. **95**, 217204.

Wang, K. Y., *et al.*, 2010, Appl. Phys. Lett. **97**, 262102.

Wang, M., R. P. Campion, A. W. Rushforth, K. W. Edmonds, C. T. Foxon, and B. L. Gallagher, 2008, Appl. Phys. Lett. **93**, 132103.

Wang, M., K. W. Edmonds, B. L. Gallagher, A. W. Rushforth, O. Makarovsky, A. Patane, R. P. Campion, C. T. Foxon, V. Novak, and T. Jungwirth, 2013, Phys. Rev. B **87**, 121301(R).

Wang, Y., Z. A. Xu, T. Kakeshita, S. Uchida, S. Ono, Y. Ando, and N. P. Ong, 2001, Phys. Rev. B **64**, 224519.

Wang, Y. Y., C. Song, B. Cui, G. Y. Wang, F. Zeng, and F. Pan, 2012, Phys. Rev. Lett. **109**, 137201.

Wenisch, J., C. Gould, L. Ebel, J. Storz, K. Pappert, M. J. Schmidt, C. Kumpf, G. Schmidt, K. Brunner, and L. W. Molenkamp, 2007, Phys. Rev. Lett. **99**, 077201.

Werpachowska, A., and T. Dietl, 2010, Phys. Rev. B **82**, 085204.

Wisniewski, P., 2007, Appl. Phys. Lett. **90**, 192106.

Woltersdorf, G., O. Mosendz, B. Heinrich, and C. H. Back, 2007, Phys. Rev. Lett. **99**, 246603.

Woodbury, D. A., and J. S. Blakemore, 1973, Phys. Rev. B **8**, 3803.

Wunderlich, J., T. Jungwirth, A. C. Irvine, B. Kaestner, A. B. Shick, R. P. Campion, D. A. Williams, and B. L. Gallagher, 2007, J. Magn. Magn. Mater. **310**, 1883.

Wunderlich, J., T. Jungwirth, V. Novák, A. C. Irvine, B. Kaestner, A. B. Shick, C. T. Foxon, R. P. Campion, D. A. Williams, and B. L. Gallagher, 2007, Solid State Commun. **144**, 536.

Wunderlich, J., B. Kaestner, J. Sinova, and T. Jungwirth, 2005, Phys. Rev. Lett. **94**, 047204.

Wunderlich, J., *et al.*, 2006, Phys. Rev. Lett. **97**, 077201.

Wunderlich, J., *et al.*, 2007, Phys. Rev. B **76**, 054424.

Yakunin, A. M., A. Y. Silov, P. M. Koenraad, J. H. Wolter, W. Van Roy, J. De Boeck, J. M. Tang, and M. E. Flatté, 2004, Phys. Rev. Lett. **92**, 216806.

Yamanouchi, M., D. Chiba, F. Matsukura, T. Dietl, and H. Ohno, 2006, Phys. Rev. Lett. **96**, 096601.

Yamanouchi, M., D. Chiba, F. Matsukura, and H. Ohno, 2004, Nature (London) **428**, 539.

Yamanouchi, M., J. Ieda, F. Matsukura, S. E. Barnes, S. Maekawa, and H. Ohno, 2007, Science **317**, 1726.

Yang, S. R. E., J. Sinova, T. Jungwirth, Y. P. Shim, and A. H. MacDonald, 2003, Phys. Rev. B **67**, 045205.

Yao, Y., L. Kleinman, A. H. MacDonald, J. Sinova, T. Jungwirth, D. sheng Wang, E. Wang, and Q. Niu, 2004, Phys. Rev. Lett. **92**, 037204.

Yildirim, M., S. March, R. Mathew, A. Gamouras, X. Liu, M. Dobrowolska, J. K. Furdyna, and K. C. Hall, 2012, Appl. Phys. Lett. **101**, 062403.

Yokoyama, M., H. Yamaguchi, T. Ogawa, and M. Tanaka, 2005, J. Appl. Phys. **97**, 10D317.

Yu, K. M., W. Walukiewicz, T. Wojtowicz, I. Kuryliszyn, X. Liu, Y. Sasaki, and J. K. Furdyna, 2002, Phys. Rev. B **65**, 201303.

Yuldashev, S., K. Igamberdiev, S. Lee, Y. Kwon, Y. Kim, H. Im, A. Shashkov, and T. W. Kang, 2010, Appl. Phys. Express **3**, 073005.

Zemen, J., J. Kucera, K. Olejnik, and T. Jungwirth, 2009, Phys. Rev. B **80**, 155203.

Zhang, S., and Z. Li, 2004, Phys. Rev. Lett. **93**, 127204.

Zhou, Y.-Y., Y.-J. Cho, Z. Ge, X. Liu, M. Dobrowolska, and J. K. Furdyna, 2007, IEEE Trans. Magn. **43**, 3019.